**TÉCNICO LISBOA**

# Dynamic brain functional connectivity analysis in migraine: a resting-state fMRI study

## Cláudia Marina Alves Fonseca

Thesis to obtain the Master of Science Degree in

## Biomedical Engineering

Supervisors: Prof. Patrícia Margarida Piedade Figueiredo

Dr. Raquel Santos Gil-Gouveia

## Examination committee

Chairperson: Prof. Mário Jorge Costa Gaspar da Silva

Supervisor: Prof. Patrícia Margarida Piedade Figueiredo

Member of the Committee: Prof. Anna Luiza Barszczak Sardinha Letournel

## October 2021

# Declaration

I declare that this document is an original work of my own authorship and that it fulfils all the requirements of the Code of Conduct and Good Practices of the Universidade de Lisboa.

# Preface

The work presented in this thesis was performed at LaSEEB (Evolutionary Systems and Biomedical Engineering Lab) of Institute for Systems and Robotics, at Instituto Superior Técnico from University of Lisbon (Portugal), during the period February-October 2021, under the supervision of Prof. Patrícia Figueiredo and Dr. Raquel Gil-Gouveia from Hospital da Luz.

# Agradecimentos

A realização desta Dissertação de Mestrado foi uma longa viagem que se fez acompanhar de momentos e de pessoas. Quero exprimir o meu profundo e sentido agradecimento a todos aqueles que, de alguma forma, fizeram parte do meu caminho, permitindo que esta tese se concretizasse.

Em primeiro lugar, começo por expressar o meu sincero obrigada à Professora Patrícia Figueiredo, que me inspirou a explorar o mundo incrível da neuroimagiologia e que desde o início se mostrou inteiramente disponível para me guiar e esclarecer as minhas dúvidas. Foi uma honra ter integrado a equipa de investigação do LaSEEB durante estes 9 meses, e todo o apoio e confiança no meu trabalho foram cruciais para conseguir chegar ao fim deste percurso.

Quero agradecer também à Doutora Raquel Gil-Gouveia e Professora Joana Cabral por todo o conhecimento que me transmitiram e que me ajudou completar esta tese.

Um grande e profundo obrigada à Inês Esteves e à Marta Xavier, que me acompanharam incansavelmente ao longo de todo o processo. As vossas dicas e palavras de conforto foram cruciais para manter a calma nos momentos mais difíceis e ter foco para continuar o meu caminho.

Quero ainda agradecer ao Professor Alexandre Andrade, que me "acolheu" num dos seus projetos do IBEB em contexto extra-curricular e com quem dei os meus primeiros passos nesta área fascinante.

De seguida, e não menos importante, quero dar o meu especial agradecimento às pessoas que preenchem a minha vida e que me completam.

Quero agradecer do fundo do meu coração ao meu grupo de amigos do IST, Carolina Glória, Carolina Narciso, Carolina Parada, Daniela Ribeiro, José Pedro Fragoso, Laura Dias, Leonor Garcia, Ricardo Mendes, Rita Mão de Ferro, Samuel Branco e Sebastião Dias, porque batalharam comigo nestes 5 anos e tornaram-nos realmente especiais. Um agradecimento especial à Carolina Parada, por todas as conversas, apoio e paciência. Amigos que nos seguram quando caímos e que admiram as nossas conquistas tornam o percurso muito mais gratificante e motivante.

Um sincero obrigada às minha amigas Dulce Canha e Ivânia Machado, que me acompanham há mais de 10 anos da minha vida e com quem sei que posso sempre contar. Vocês partilham as minhas vitórias comigo, e orientam-me quando tudo parece ao contrário.

Um agradecimento muito especial ao Paulo Aires, que esteve presente desde o início deste percurso com palavras de carinho e encorajamento. O lema "uma hora a mais de trabalho hoje, uma hora a menos de trabalho amanhã" ficou comigo até hoje.

E, por fim, o agradecimento que tenho para dar à minha família dificilmente caberia em palavras. Às minhas grandes inspirações, por quem tenho o maior respeito – mãe Anabela, pai Mário e mana Beatriz – o meu mais sincero obrigada. O apoio incondicional que me deram ao longo da minha vida levou-me a correr atrás dos meus objetivos independentemente da dificuldade dos obstáculos, e o carinho e alento nos momentos mais árduos motivaram-me a continuar com coragem quando tudo parecia impossível. Se hoje chego à última etapa do meu mestrado, é graças a vocês.

Um grande obrigada também à minha avó Zulmira, ao meu avô Amândio e ao meu tio Nando, por todo o apoio, carinho, e presença inabaláveis, e por nunca me deixarem desistir dos meus sonhos.

A todos, estou-vos eternamente grata.

# Acknowledgments

The path behind this Master's Thesis was a challenging one, filled with people and moments along the way. I want to express my deep and heartfelt gratitude to all of those who were part of this journey in some way, bringing this dissertation to fruition.

First and foremost, I will begin by expressing my honest gratitude to Professor Patrícia Figueiredo, who inspired me to explore the incredible world of neuroimaging and was fully available to guide me from the beginning and clarify all my doubts. It was an honour to be part of the LaSEEB research team during these 9 months, and all the support and trust in my work were crucial to reach the end of this journey.

I would also like to thank Doctor Raquel Gil-Gouveia and Professor Joana Cabral for all the knowledge, which helped me complete this dissertation.

Next, I want to express my profound gratitude to Inês Esteves and Marta Xavier, who tirelessly accompanied me through the whole process. Your tips and comfort words were crucial to keep calm in the most challenging moments, as well as to focus on continuing my path.

I would also like to thank Professor Alexandre Andrade, who welcomed me in one of his projects in IBEB in an extra-curricular context and with whom I took my first steps in this fascinating field.

Furthermore, and not less important, I want to give my special thanks to the people that fulfil my life and complete me.

From the bottom of my heart, I want to thank my group of friends from IST, Carolina Glória, Carolina Narciso, Carolina Parada, Daniela Ribeiro, José Pedro Fragoso, Laura Dias, Leonor Garcia, Ricardo Mendes, Rita Mão de Ferro, Samuel Branco and Sebastião Dias, because they always fought alongside me, making these last 5 years truly special. A special thanks to Carolina Parada for all the talks, support and patience. Friends who hold us when we fall and admire our achievements make the journey much more rewarding and motivating.

A sincere thanks to my friends Dulce Canha and Ivânia Machado, who have accompanied me for more than 10 years of my life and whom I know I can always count on. You share my victories with me and guide me when everything seems upside down.

I would also like to express my special thanks to Paulo Aires, who was present with words of affection and encouragement from the very beginning of this journey. The motto "one more hour of work today, one less tomorrow" has stayed with me until today.

Finally, the gratitude towards my family would hardly fit into words. My most sincere thank you to my big inspirations, to whom I hold enormous respect – my mother Anabela, my father Mário and my sister Beatriz. The unconditional support you gave me throughout my life led me to run after my goals regardless of the obstacles, and your affection and encouragement in the most arduous moments motivated me to continue when everything seemed impossible. If today I reach the last stage of my master, it is thanks to you.

Also, a big thank you to my grandmother Zulmira, my grandfather Amândio and my uncle Nando for all their support, affection and unwavering presence, and for never letting me give up on my dreams.

To all of you, I am eternally grateful.

x

# Resumo

A enxaqueca é uma patologia neurológica incapacitante caracterizada por crises recorrentes de cefaleias pulsáteis, geralmente acompanhadas de náuseas, vómitos, distúrbios sensoriais e cognitivos. Apesar de ser considerada um problema de saúde pública, a sua patofisiologia não é totalmente conhecida. De modo a investigar os mecanismos deste distúrbio, procedeu-se ao estudo da conetividade funcional dinâmica (dFC) através da análise de dados de ressonância magnética funcional em repouso de oito pacientes com enxaqueca episódica menstrual sem aura na fase interictal do ciclo de enxaqueca, cinco das oito pacientes na fase ictal, e seis controlos saudáveis na fase menstrual de pós-ovulação para controlo hormonal na fase interictal. Primeiramente, a dFC foi estimada com os métodos da janela temporal e coerência de fase. Depois, a análise dinâmica do vetor próprio principal focou-se nos padrões dominantes das matrizes de dFC, agrupados posteriormente em estados de dFC recorrentes com o algoritmo k-médias. As diferenças entre grupos foram avaliadas estatisticamente com *t-tests* de permutação não-paramétrica. Verificou-se para a fase ictal e controlos um aumento significativo do tempo de vida médio e probabilidade de ocorrência em redes de atenção dorsal/frontoparietais, redes somatomotora e visual, e uma diminuição dessas métricas temporais no estado *global mode* comparativamente à fase interictal. Esta investigação enfatizou a relevância de analisar a dFC para estudar a enxaqueca, e a possibilidade deste distúrbio estar associado a uma alteração na dinâmica de sistemas de atenção/cognitivos, de processamento sensorial e do *global mode*, os quais poderão constituir biomarcadores neuroimagiológicos para a monitorização da progressão desta patologia.

**Palavras-chave:** enxaqueca episódica, conetividade funcional dinâmica, ressonância magnética funcional em repouso, coerência de fase, análise dinâmica do vetor próprio principal, estados de conetividade funcional dinâmica

# Abstract

Migraine is an incapacitating neurological disorder characterised by recurring, throbbing headache attacks, generally combined with nausea, vomiting, sensory and cognitive disturbances. Migraine has become a major public health concern with a huge impact worldwide, however, its pathophysiology is not entirely understood. In order to investigate the disorder mechanisms, dynamic functional connectivity (dFC) in migraineurs was assessed through the analysis of resting-state functional magnetic resonance imaging data. Eight female menstrual episodic migraine patients without aura were scanned in the interictal (attack-free) phase of the migraine cycle, five of the eight patients in the ictal (attack) phase, and six healthy controls in the menstrual mid-cycle/post-ovulation phase to control hormonal variation in the interictal phase. To estimate the dFC, the sliding window and phase coherence methods were tested. Then, the leading eigenvector dynamic analysis focused on the dominant patterns of dFC matrices captured by leading eigenvectors, further organised into recurrent dFC states with the k-means clustering algorithm. Finally, between-group differences were statistically assessed with non-parametric permutation-based $t$-tests. Results revealed a significant increased mean lifetime and probability of occurrence in dorsal attention/frontoparietal, somatomotor and visual networks, and decreased temporal metrics in the fully connected state (global mode) in migraine patients in the ictal phase and controls compared to the interictal phase. This work reinforced the relevance of using dFC to study migraine brain, and suggested that its dysfunction might be associated with an altered dynamic of attentional/cognitive and stimulus processing systems and the global mode, which might potentially constitute neuroimaging biomarkers for disease progression.

# Contents

# List of Tables

# List of Figures

# Nomenclature

| | |
|---|---|
| **AAL** | Automated Anatomic Labelling |
| **ALFF** | Amplitude of Low-Frequency Fluctuations |
| **ATP** | Adenosine Triphosphate |
| **AudN** | Auditory Network |
| **BasN** | Basal Ganglia Network |
| **BOLD** | Blood Oxygen Level Dependent |
| **CEN** | Central Executive Network |
| **CbN** | Cerebellar Network |
| **CG** | Cervical Ganglion |
| **CGRP** | Calcitonin Gene-Related Peptide |
| **CNR** | Contrast-to-Noise Ratio |
| **CogCN** | Cognitive Control Network |
| **CSD** | Cortical Spreading Depression |
| **DAN** | Dorsal Attention Network |
| **dFC** | Dynamic Functional Connectivity |
| **dHb** | Deoxyhaemoglobin |
| **DMN** | Default Mode Network |
| **ECN** | Executive Control Network |
| **EEG** | Electroencephalography |
| **EPI** | Echo-Planar Imaging |
| **fALFF** | Fractional Amplitude of Low-Frequency Fluctuations |
| **FC** | Functional Connectivity |
| **FID** | Free-Induction Decay |
| **fMRI** | Functional Magnetic Resonance Imaging |
| **FPN** | Frontoparietal Network |
| **FPCEN** | Frontoparietal Central Executive Network |
| **GRAPPA** | GeneRalized Autocalibrating Partial Parallel Acquisition |
| **$HbO_2$** | Oxyhaemoglobin |

| | |
|---|---|
| **HCP** | Human Connectome Project |
| **HRF** | Haemodynamic Response Function |
| **ICA** | Independent Component Analysis |
| **ICHD** | International Classification of Headache Disorders |
| **LEiDA** | Leading Eigenvector Dynamic Analysis |
| **LFP** | Local Field Potentials |
| **LN** | Limbic Network |
| **LTI** | Linear and Time-Invariant |
| **MEG** | Magnetoencephalography |
| **MNI** | Montreal Neurological Institute |
| **MRI** | Magnetic Resonance Imaging |
| **MPRAGE** | Magnetization-Prepared Rapid Gradient Echo |
| **NMR** | Nuclear Magnetic Resonance |
| **PAG** | Periaqueductal Grey |
| **PC** | Phase Coherence |
| **PCA** | Principal Component Analysis |
| **PVEs** | Partial Volume Effects |
| **RB** | Rigid Body |
| **rCBF** | Regional Cerebral Blood Flow |
| **rCBV** | Regional Cerebral Blood Volume |
| **rCMRO$_2$** | Regional Cerebral Metabolic Rate of Oxygen |
| **rCMR$_{glu}$** | Regional Cerebral Metabolic Rate of Glucose |
| **ReHo** | Regional Homogeneity |
| **RF** | Radiofrequency |
| **ROI** | Region-Of-Interest |
| **rs-fMRI** | Resting-State Functional Magnetic Resonance Imaging |
| **RSN** | Resting-State Networks |
| **RVM** | Rostral Ventromedial Medulla |
| **S1** | Primary Somatosensory Cortex |
| **S2** | Secondary Somatosensory Cortex |
| **SCN** | Subcortical Network |
| **sFC** | Static Functional Connectivity |
| **SMN** | Somatomotor Network |
| **SMS** | Simultaneous Multislice |

| | |
|---|---|
| **SN** | Salience Network |
| **SNR** | Signal-to-Noise Ratio |
| **SpVC** | Spinal Trigeminal Nucleus |
| **SPG** | Sphenopalatine Ganglion |
| **SSN** | Superior Salivatory Nucleus |
| **SW** | Sliding Window |
| **TCC** | Trigeminocervical Complex |
| **TE** | Time Echo |
| **TG** | Trigeminal Ganglion |
| **TR** | Time Repetition |
| **TV** | Trigeminovascular |
| **TVS** | Trigeminovascular System |
| **VAN** | Ventral Attention Network |
| **VLatN** | Visual Lateral Network |
| **VMedN** | Visual Medial Network |
| **VN** | Visual Network |
| **VOccN** | Visual Occipital Network |
| **WHO** | World Health Organization |
| **WTC** | Wavelet Transform Coherence |

# Chapter 1

# Introduction

*This chapter provides the reader with the motivation behind the present work in section 1.1., followed by the main objectives of this investigation in section 1.2. Finally, section 1.3. describes the thesis outline, with an overview of the chapters included in this study.*

## 1.1. Motivation

Migraine is a complex neurological headache disorder among the most prevalent and disabling conditions worldwide, estimated to affect over 20 % of the population in a 3:1 female-to-male ratio [1]. According to the Global Burden of Disease study (2019) from the World Health Organization (WHO) [2], this disorder ranks second among the world's causes of disability and first in young women [3].

The cyclic nature of migraine is characterised by recurrent and incapacitating headache attacks, which typically coincide with wide-ranging symptomatology, followed by attack-free phases. These symptoms include nausea, vomiting, sensory disturbances, muscle tenderness [4], and attentional, cognitive, and executive impairments [5], contributing to the great complexity of this disorder.

Despite the massive individual impact that migraine brings, it also entails burdensome consequences on private and socioeconomic domains, especially due to the productivity losses caused by its prevalence in the youngest and most productive years of life [1][6]. Notwithstanding, migraine remains undervalued in terms of priority setting and resource allocation processes, and new therapeutics to treat this condition lack investment [7].

In the last two decades, technologies to investigate migraine pathophysiology progressed greatly. Functional neuroimaging techniques, especially functional magnetic resonance imaging (fMRI), have become an indispensable tool in migraine research and have driven robust advances in understanding migraine generation, progression, chronification and treatment. In particular, resting-state fMRI (rs-fMRI) has gained widespread acceptance in the neuroscience community as a powerful technique to explore spontaneous migraine brain activity and functional connectivity (FC) for characterising brain's spatiotemporal organisation and mapping brain function [8].

Studying migraine patients in different phases of the migraine cycle and healthy controls have allowed for a deeper comprehension regarding migraine phase-specific alterations in neuronal activity, stimulus processing and FC [9][10]. Therefore, emerging studies in pair with new optimized approaches

may contribute to advancing the knowledge of migraine mechanisms and eventually identify potential biochemical, genetic and/or imaging clinical biomarkers able to ensure a more accurate diagnosis of the disorder, better prediction of each individual's response to treatment, and, potentially, recognition of targets to develop novel therapeutics.

## 1.2. Objectives

This Master's Thesis aims to study dFC in migraine and investigate specific brain alterations during the ictal (attack) and interictal (attack-free) phases of the migraine cycle. These alterations might potentially contribute to advances in the knowledge of migraine pathophysiology and constitute neuroimaging biomarkers to predict this disorder's progression or response to treatment.

The dFC is estimated from rs-fMRI data and organised into quasi-stable recurrent FC patterns, called the dFC states [11]. These states can be characterised in terms of spatial patterns (correlation with well-established resting-state functional networks), temporal metrics (mean lifetime, probability of occurrence and switching profile) and FC strength (mean eigenvalue).

Different methodologies are proposed to be implemented and compared throughout the work to evaluate their impact on the results (dFC states). Hence, the specific target objectives of the present dissertation are the following:

1.  **Preprocessing:** Compare a minimal preprocessing pipeline with a more refined preprocessing protocol including additional denoising steps – Independent Component Analysis (ICA) noise clean-up and nuisance regression;
2.  **Parcellation:** Assess the influence of different atlases (with different cortical and subcortical resolutions) to parcellate preprocessed data (namely the Automated Anatomical Labelling (AAL), Desikan and Harvard-Oxford atlases);
3.  **dFC estimation:** Compare the Sliding Window (SW) Pearson correlation method with the Phase Coherence (PC) method using the Hilbert transform approach;
4.  **Smoothing dFC labels:** Evaluate the impact of implementing a temporal smoothing algorithm to the dFC labels on temporal metrics;
5.  **Static vs. dynamic FC:** Compare the information provided by dFC (FC over time) with the one from static FC (sFC) (average of FC over time);
6.  **Investigate migraine-specific dFC alterations:** Compare different phases of the migraine cycle (ictal with interictal) and migraineurs in the interictal phase with healthy controls.

## 1.3. Thesis outline

This dissertation is organised into five main chapters. The first and current chapter 1 comprises an introduction to the work, including the motivation for the conducted study, the objectives proposed to be accomplished and the thesis outline.

Chapter 2 provides the reader with the theoretical background required to understand the approached concepts, namely migraine clinical aspects and pathophysiology, basic principles of fMRI,

rs-fMRI and FC, and comprises a review with the current state-of-the-art of migraine rs-fMRI studies and the main findings regarding sFC and dFC.

Next, chapter 3 presents a complete description of the data acquisition, including the characteristics of the participants involved in the project and the parameters of the acquired rs-fMRI data. Furthermore, this chapter explains the methodologies followed for the data analysis performed in this work, comprising the preprocessing and parcellation steps, the methods used to estimate the dFC matrices, the LEiDA applied to reduce the dimensionality of the data while explaining the majority of its variance, and the approaches followed to estimate and characterise the dFC states. Finally, this chapter describes the statistical analyses performed, namely the correlation of the dFC states with resting-state networks and the comparison between migraine patients in the interictal and ictal sessions and between migraineurs in the interictal session and healthy controls.

Furthermore, chapter 4 displays the results obtained with the fMRI data analysis and their interpretation and comparison with findings from the literature. This chapter includes an exploratory analysis of the FC repertoire obtained for the migraine interictal dataset, which comprises several comparisons derived from altering methods of the procedure, and a statistical analysis to evaluate the significant differences between migraine patients in the interictal and ictal phases and between migraineurs in the interictal phase and healthy controls.

At last, chapter 5 highlights the main conclusions to be drawn from this work, along with the main limitations and suggestions regarding future work.

# Chapter 2

# Context and Related Work

*This chapter provides the reader with theoretical background regarding the work developed in this Master's Thesis and the related work. Section 2.1. presents the context behind the present study concerning migraine. Next, section 2.2. provides an overview of the fMRI field and associated concepts. Finally, section 2.3. describes the state-of-the-art review of studies directed to the sFC and dFC analysis in migraine and other headache-related disorders.*

## 2.1. Migraine

Migraine is a common, incapacitating brain disorder characterised by recurrent attacks of throbbing headaches that can last from 4 to 72 hours [12], generally accompanied by wide-ranging symptoms including nausea, vomiting, hypersensitivity to sensory inputs (visual, auditory and olfactory) and movement, cutaneous allodynia (abnormal skin sensitivity) and muscle tenderness [4][13].

Migraine attacks typically begin around puberty, although they may have their first occurrence in childhood, a few times per year, and their frequency can increase up to a few times per week in adulthood [4][14]. Due to this heterogeneity, the International Classification of Headache Disorders (ICHD) (ICHD-3 beta) classifies migraine as either episodic, if the patient suffers up to 14 headache days per month, or chronic, when the frequency of the attacks corresponds to at least 15 days per month, with migraine-associated features required on 8 of the 15 headache days [15].

Scientific evidence supports the notion that migraine has a strong genetic basis, being tendentially more prevalent in genetically susceptible individuals [4]. In fact, advances in genetics have already identified 38 genomic migraine-associated *loci* [16]. Furthermore, familial hemiplegic migraineurs have revealed single genetic mutations associated with deficits in ion channels (e.g. $Na^+$-K-ATPase pump or $\alpha_1$-subunit of the voltage-gated P/Q-type calcium channel), and two families with migraine exhibited mutations in the gene expressing casein-kinase-1$\delta$ involved in circadian rhythm disorders [16]–[18].

Migraine is recognised by WHO as a global health priority, estimated to affect over 20% of the population in a 3:1 female-to-male ratio [1], and ranking second among the world's causes of disability and first in young women [2][3]. Data estimate that 5.4% of the total years lived with disability are attributed to headache disorders, with migraine accounting for 88.2% of those, which corresponds to 46.6 million people dying one year early in terms of lost health life [3].

The massive prevalence of migraine entails burdensome consequences on private and socio-economic domains, which have been underestimated in numerous health care systems and resource allocation processes. In particular, productivity losses are significant and largely amplified due to the prevalence of this condition in the youngest and most productive years of life (15 to 49 years) [1][6].

Furthermore, it is worth mentioning that this disorder has a severe impact on a mental health level and brings indirect intangible costs that exceed the direct costs of medical care. A global survey performed among migraineurs in 2018 revealed that 85% of all participants felt depressed, helpless, and misunderstood during life, and 55% lived in fear of the next attack [19].

Despite the meaningful impact of migraine, therapeutics for this condition lack investment [7]. Currently, the available therapies are either acute treatments that induce the termination of acute attacks (e.g. administration of analgesics, antiemetics, ergotaminics and triptans) or prophy-lactic treatments that act on their prevention (e.g. anticonvulsants, β-blockers, calcium channel modula-tors and tricyclic antidepressants), decreasing the duration, intensity and frequency of their associated features [7][20][21]. However, these therapies present disadvantages. The acute treatment only relieves the pain entirely within 2 hours and for a minority of patients, being overused in several situations, and is susceptible to the patient's sensitivity to the medication and contraindications, such as cardiovascu-lar diseases. In turn, prophylactic treatment is only effective for a limited number of migraineurs [13].

Over recent years, events and associations to support and empower migraineurs have increased. For example, in 2019, Portugal created the first portuguese association of migraine and headache patients *MiGRA Portugal*, the American Migraine Foundation made the campaign *Move Against Migraine*, and the World Federation of Neurology dedicated the *World Brain Day* to this disorder.

Nonetheless, it is essential to keep raising awareness for the investment and research needs of this condition in order to allow for a better understanding of its pathophysiological mechanisms, for the development of new therapies to improve its outcomes and, in a broader perspective, for the optimisation of the resource allocation and clinical management [2][6].

### 2.1.1. Clinical aspects

The migraine phenotype is periodic. A complete migraine cycle is characterised by the interictal phase and the migraine attack, as depicted in Figure 2.1. The interictal phase corresponds to the interval between two consecutive migraine attacks in which the patients are usually asymptomatic. The migraine attack comprises the preictal, ictal and postictal phases, which may happen sequentially, but, in most cases, they are overlapped [22].

The preictal phase, also known as the premonitory phase or prodrome, corresponds to the time before the onset of the headache and can be manifested up to 48 hours [23]. Commonly, this stage includes sensory symptoms, such as photophobia, phonophobia, osmophobia, allodynia and muscular sensitivity; affective symptoms, involving irritability and depression; autonomic symptoms, namely fati-gue, yawning, food cravings, thirst, flushing, sweating, nasal and sinus congestion, rhinorrhoea, frequent urination and diarrhoea; and cognitive symptoms, thought to be reversible and finished after the attack or with effective acute treatment [4][5][14]. The most common pattern of cognitive decline involves speech, reading and concentration difficulties and impaired thinking during the preictal, ictal and post-

ictal phases, which suggests attentional and executive deficits with abnormalities in processing speed, decision-making, planning and working memory [5][24]. Although this symptom repertoire is characteristic of the prodrome, it may be noticeable and endure throughout the cycle, being usually less prevalent in the headache phase [4][25].

Some authors consider the prodromal manifestations reliable predictors of the incoming attacks [24]. If patients identify those symptoms early, the avoidance of stimuli that may trigger the attack (e.g. sensory stimuli, missing meals, caffeine, alcohol, smoke, physical exercise) and the early start of the treatment may attenuate the following symptoms [4][14].
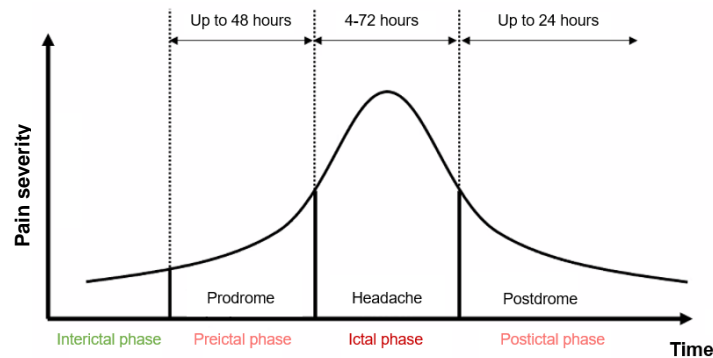


Figure 2.1. Migraine cycle. The migraine attack can be dissected into three different periods: the preictal phase or prodrome, which lasts up to 48 hours; the ictal phase, which can last between 4 to 72 hours and corresponds to the period in which the patient experiences the headache; and the postictal phase or postdrome, which takes up to 24 hours. The interictal period corresponds to the interval between two consecutive migraine attacks. The headache pain severity reaches its maximum in the ictal phase. Figure adapted from Peng and May [22].

Regarding the aura, this phase is experienced immediately after the prodrome, only by approximately one-third of migraineurs, and according to the ICHD-3 beta [15], it consists of a total reversible neurological disturbance and cortical dysfunction that lasts between 15 and 30 minutes [14][23]. The visual aura, which is the most common type of disturbance, is characterised by visual changes known as the fortification spectra (positive symptoms such as scintillations and flashes of lights) or the scotomas (negative symptoms such as blind spots). However, other cortical perturbations may occur, involving motor, sensory and language spectra [26].

The ictal phase corresponds to the interval of 4 to 72 hours in which the patient experiences the headache and maximum pain severity. Thereafter, the postictal phase finishes the migraine attack.

The postictal phase or postdrome lasts up to 24 hours after the headache phase and can be defined as the period between the resolution of the headache and total recovery. Despite the large neglection of this phase by the scientific community, not even documented in the ICHD-3 beta [15], some patients report symptoms involving tiredness, attention deficits and neck stiffness [25][27].

Although the interictal phase of the migraine cycle is tendentially asymptomatic, some studies argue otherwise. Neurophysiological evidence points to cases of hypersensibility to sensory stimuli, stripe-induced visual discomfort and cognitive dysfunction [24]. Moreover, converging evidence describes the existence of a habituation response deficit in the attack-free phase. Instead of a regular habituation effect, with a "response decrement" resulting from the exposure to repeated stimuli, interictal migraineurs exhibit an initial weaker response that intensifies with persistent stimulation (e.g. sensory inputs), leading to some vulnerability in those conditions [24][28].

Hence, the peculiarities of each phase and the intra- and inter-patient varying symptoms contribute to the huge complexity of this disorder.

## 2.1.2. Origin: Vascular vs. Neural theories

Headaches started to be recognised nearly 6,000 years ago, while the defining features of migraine only emerged in the work of Willis published in the 17th century [14].

In the 1870s, Edward Liveing described migraine attacks as "nerve-storm" headaches derived from a brain disorder. In the same year, Peter Latham's work suggested that migraine was originated from vasodilation and triggered by aura [14]. Since then, the origin of migrainous pain and the pathophysiological events involved in triggering and conducting its progression have been under medical debate and dichotomised into either vascular or neural events [7][29].

The vascular hypothesis has dominated for many years, suggesting that mechanisms driving migraine attacks occurred in the major pain sensing regions of the brain – meninges and large cerebral blood vessels [30]. In fact, in 1940, the famous work of Graham and Wolff showed a strong correlation between the migraine headache pain and the amplitude of pulsation of the cranial vasculature, namely that the administration of ergotamine tartrate would constrict specific branches of the external carotid arteries, reducing the amplitude of their pulsations and, therefore, the intensity of the headache [31].

Approximately four years later, the first pure neuronal theory for the origin of migraine by Aristides Leão claimed that the alterations in blood flow derived from neuronal activation [30]. Posterior advances in migraine biology research and development of medicines with both neural and vascular effects (e.g. sumatriptan) contributed to discrediting the entirely vascular nature of the disorder [14].

Over the years, migraine perception transited from a purely vascular disorder to a neurovascular condition primarily associated with abnormal brain activity, since the brain of a migraineur differs from a non-pathological brain, with the vasculature playing a critical role in the disease mechanisms [4][25]. Nowadays, migraine is considered a central nervous system disorder [32]. Nevertheless, the origin of its attacks and the underlying brain structures and neurobiological processes involved in their progression remains unclear and under clinical and scientific research.

## 2.1.3. Pathophysiology

Reports suggest that migraine attacks are commonly driven by triggers, such as anxiety, fatigue, stress, sleep disturbances, posture, physical exercise, food or missing meals, alcohol, caffeine, smoke, hormonal and environmental changes, and sensory stimuli (e.g. bright lights, loud noises and intense odours) [4][33]. The association of migraine triggers with a destabilisation of the body homeostasis suggests a major involvement of the hypothalamus in the symptomatology of this disorder, with the brainstem, thalamus and cortical regions also playing a significant role [4][33]. Currently, the putative basis for migraine attacks is the activation of the meningeal nociceptors and the trigeminovascular system (TVS), followed by its peripheral and central sensitisation.

### 2.1.3.1. Activation of the meningeal nociceptors

The hypothalamus is involved in the regulation of homeostatic networks and circadian rhythms of the body [4] – appetite and food intake (linked to the mediobasal nucleus), sleep arousal (suprachiasmatic

nucleus) and stress and mood changes (paraventricular nucleus) [34] – and autonomic and endocrine factors. Furthermore, this brain region is interconnected with structures that participate in migraine mechanisms, such as the brainstem and the spinal trigeminal nucleus (SpVC) located in the trigeminocervical complex (TCC) of the medullary dorsal horn, which emphasises the relevance in correlating external with internal factors, and migraine triggers with the prodromal manifestations [34].

A plausible hypothesis for the activation of the meningeal nociceptors is the ability of the hypothalamic neurons to affect the balance between the parasympathetic and sympathetic tone [13], which is schematically illustrated in Figure 2.2.
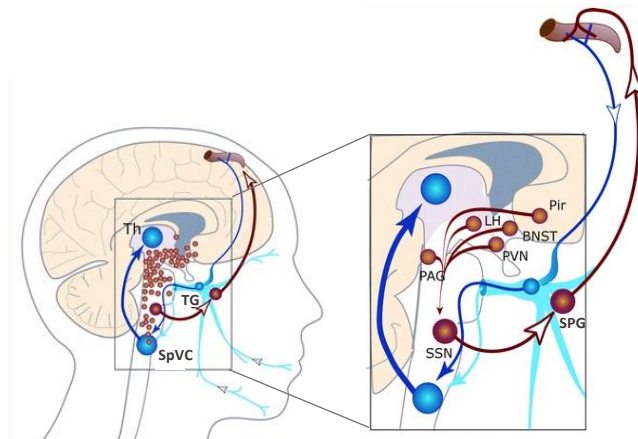


Figure 2.2. Parasympathetic pathway involved in the activation of meningeal nociceptors and TVS. The SSN receives input from hypothalamic and limbic areas (LH, PVN, PAG, Pir and BNST), whose activity is controlled by migraine triggers. This process activates the SPG and leads to the neurogenic inflammation, meningeal vasodilation and activation of the TV neurons in the SpVC. In parallel, the activation of the TG potentiates the increase of the parasympathetic tone. BNST = Bed Nucleus of Stria Terminalis; LH = Lateral Hypothalamus; PAG = Periaqueductal Gray; Pir = Piriform Cortex; PVN = Paraventricular Hypothalamic Nucleus; SPG = Sphenopalatine Ganglion; SpVC = Spinal Trigeminal Nucleus; SSN = Superior Salivatory Nucleus; TG = Trigeminal Ganglion; Th = Thalamus. Figure adapted from Burstein et al. [35].

Firstly, the hypothalamus and brain regions integrating the limbic system send inputs to the preganglionic parasympathetic neurons in the superior salivatory nucleus (SSN) located in the pons of the brainstem, which unleashes the neurogenic inflammation from the meningeal terminals of postganglionic parasympathetic neurons in the sphenopalatine ganglion (SPG) of the TVS. The neurogenic inflammation consists of the local release of endogenous vasoactive neuropeptides, namely acetylcholine, calcitonin gene-related peptide (CGRP), substance-P, pituitary adenylate cyclase-activating polypeptide-28, vasopressin intestinal peptide and nitric oxide, which induce an augmented parasympathetic outflow to the cranial vasculature [4][35]. Consequently, the meningeal nociceptors vasodilate, leading to the activation of trigeminovascular (TV) neurons in the SpVC and a cascade of signalling events and perivascular changes that culminate in head pain [36], which is explained hereinafter in section 2.1.3.2. This process generates a parallel loop since it simultaneously induces trigeminal ganglion (TG) stimulation, increasing the parasympathetic tone expression [13].

Another hypothesis for the activation of the meningeal nociceptors is the electrophysiological phenomenon known as cortical spreading depression (CSD), which originates the aura. The CSD consists of a transient depolarisation wave that propagates slowly across the brain, excites the cortical neurons and glia (hyperemia or phase of depolarisation) and subsequently inhibits them (oligemia or

phase of hyperpolarisation), silencing the spontaneous and evoked synaptic activity up to 30 minutes [37]. In the case of visual aura, the abnormalities in the visual field described by migraineurs are believed to derive from the initiation of the CSD in the occipital lobe and its retinotopic propagation throughout the visual cortex [14]. The susceptibility of migraineurs to trigger CSD and aura derives from the hypothesis that migraine is a disorder with an altered brain state of hyperexcitability. Indeed, central neuronal hyperexcitability in migraine has been observed in several studies, with enhanced levels of oxidative stress biomarkers accompanied by a reduction of antioxidant mechanisms and alterations in the mitochondrial metabolism. These alterations induce increased levels of lactic acid and deficits in NADH-dehydrogenase and cytochrome-c-oxidase [38].

The CSD has been proved to disturb the neurovascular coupling, inducing a temporary decrease of cerebral blood flow, deregulation of ionic and metabolic homeostasis and deficits in cortical activity. Then, the autoregulation of the cerebral blood flow occurs together with the local release of adenosine triphosphate (ATP), glutamate, hydrogen, potassium ions (by neurons, glia and vascular cells), and vasoactive neuropeptides (by peripheral nerves), which diffuse and activate the meninges [4][13][17].

### 2.1.3.2. The Trigeminovascular System

The anatomy of the TVS consists of trigeminal neurons (with cell bodies localised in the TG) and the cerebral vasculature they innervate [39]. The main function of this pathway is to convey nociceptive information from the meninges to the brain, firstly to central regions and subsequently to the cortex [35].

The trigeminal neurons present first-order peripheral axonal projections that extend mainly through the ophthalmic division of the trigeminal nerve (V1) (with lesser extent through the maxillary (V2) and mandibular (V3) nerves) and reach the meninges (pial, arachnoid and dural blood vessels), venous sinuses and large cerebral arteries [37][40]. Thus, there is a dense nociceptive innervation in the meningeal and intracerebral vasculature, with C-fibers (unmyelinated axons) and Aδ-fibers (myelinated axons), that reach the dorsal horn superficial layers (laminae I and II) [37]. Moreover, these axons have sensory afferent projections that enter the brainstem through the trigeminal tract, interact with inputs from pericranial and paraspinal muscles, adjacent skin and upper cervical spinal cord (C1-C2), and converge centrally, synapsing with SpVC (second-order) neurons in the TCC [13][37].

When the TVS is activated, incoming signals from the dural vasculature extend as trigeminal afferents through the TG and are received by the SpVC neurons, together with inputs coming from the head and neck that can also pass through the TG or as greater occipital nerve afferents through the cervical ganglion (CG) (Figure 2.3.) [37]. Then, the SpVC neurons extend via ascending pathways through the quintothalamic tract to structures that participate in the processing of nociceptive signals, namely the brainstem – periaqueductal grey (PAG), locus coeruleus and areas from the rostral ventromedial medulla (RVM) – and high cervical spinal cord, synapsing with the thalamic (third-order) neurons [37].

Thereafter, the thalamus transmits nociceptive signals to the cortex. One approach suggests that this phenomenon occurs since the thalamic neurons are densely innervated by a set of neurotransmitters and neuropeptides (mainly GABA, glutamate, dopamine and serotonin) in a system that, when unbalanced, potentiates the activation of the TVS and this signal transmission [41]. In turn, the somatosensory and visceral inputs coming from the head and orofacial regions project through the trigeminohypothalamic tract to the hypothalamus [36].
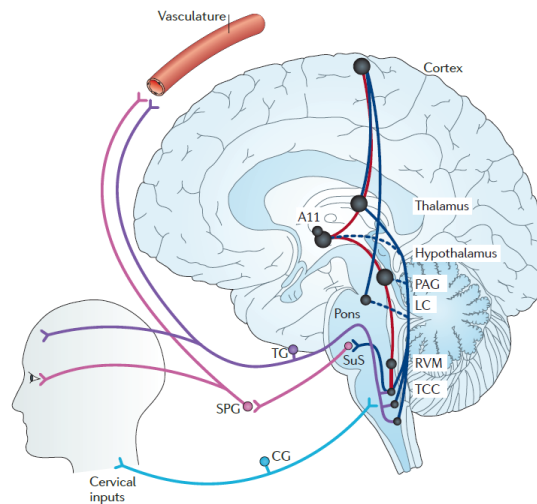
Figure 2.3. Ascending and descending pathways of the TVS. The inputs coming from the meningeal vasculature are conducted through the TG and signals from head and neck travel either through the TG or CG to the TCC. The inputs in the SpVC neurons in the TCC ascend via the quintothalamic tract to the brainstem (including PAG, LC and areas from the RVM), thalamus and hypothalamus, and also present a reflex connection to the SuS that activates the SPG, inducing the parasympathetic outflow and meningeal vasodilation. The signals coming from the thalamus and hypothalamus ascend to the cortex. The descending projections extend from the cortex to the hypothalamic, thalamic nuclei and LC. The SpVC neurons are modulated through the hypothalamus (A11 dopaminergic nucleus), PAG and RVM. CG = Cervical Ganglion; LC = Locus Coeruleus; PAG = Periaqueductal Grey; RVM = Rostral Ventro-medial Medulla; SPG = Sphenopalatine Ganglion; SuS = Superior Salivatory Nucleus; TCC = Trigemino-cervical Complex; TG = Trigeminal Ganglion. Figure adapted from Akerman et al. [36].

### 2.1.3.3. Modulation and perception of pain

The processing of nociceptive inputs throughout the TVS is complex. Upon activation of this pathway, the convergence of V1 inputs from the trigeminal nerve and signals from facial skin and cervical nerves sensitises the pericranial muscles and periorbital skin, which explains the distribution of pain perception in migraine through the occipital, cervical-neck and periorbital areas [40][42]. The perception of nociceptive signals is affected by a set of pain-modulatory circuits that involve the hypothalamus, thalamus, cortex and brainstem [36].

The hypothalamus, as mentioned in section 2.1.3.1., is critically involved in premonitory symptoms due to its role in regulating body homeostasis and several physiological functions. Furthermore, the hypothalamic projections to the SSN participate in the parasympathetic pathway and drive the activation of the TVS. Besides these roles, the hypothalamic descending pathways integrate the modulation of nociceptive signals at the spinal level and SpVC neurons, namely through the A11 dopaminergic nucleus (see Figure 2.3.). The A11 nucleus is believed to be the source of dopamine in the spinal cord and, if activated, this molecule can alter the responses in dural meningeal nociceptors [14][36].

Regarding the thalamus, it is usually interpreted as a "relay station" of nociceptive central processing and integration of affective, cognitive and sensory responses to pain [36]. Moreover, the sensitisation of central TV neurons and thalamic nuclei significantly affects the perception of pain information. The peripheral sensitisation (up to 10 minutes to develop) is characterised by a decreased threshold response and enhanced magnitude response of TV neurons, which become sensitive to dural stimulation to which their response was minimal or even null [4][13]. This phenomenon mediates the throbbing headache pain and its intensification during tasks inducing augmented intracranial pressure

(e.g. coughing or bending over) [4][37]. Furthermore, the central sensitisation of TV neurons (30 to 60 minutes to develop) and thalamic (ventroposteromedial, dorsal and posterior) nuclei (2 to 4 hours to develop) is associated with increased spontaneous neuronal activity and sensitivity to mechanical and thermal stimulation of, respectively, cephalic and extracephalic regions, as if these inputs were noxious [4][13]. This phenomenon explains the allodynia and muscle tenderness in migraine [4][37].

In the cortex, the reception of thalamic nociceptive inputs by primary/secondary (S1/S2) somato-sensory cortices and insula is associated with sensory-discriminative aspects of pain, namely its quality, intensity and location. In turn, signals sent to visual, auditory, motor, olfactory, parietal association, and retrosplenial cortices explain why an abnormal neuronal activity in these areas is involved in migraine symptoms such as hypersensitivity to light, sounds and odours, allodynia, motor clumsiness, concentration deficit and transient amnesia [37][43]. Moreover, descending cortico-trigeminal pathways modulate the excitability of SpCV neurons, inhibiting their activity if the pathway begins in S1, and stimulating it if it starts in the insular cortex [37].

The role of the brainstem in migraine has been explored over the years. In particular, in the 1980s, the origin of migrainous pain was thought to derive from functional deficits in the PAG, also called the "headache generator" [7]. During the migraine attack, the abnormal functioning of this structure would conduct changes in cortical activity, either the hyperactivation of the neurons responsible for the pain transmission in the dorsal horn or the decrease of the synaptic neuronal activity that inhibited the same pain transmission, leading to the headache pain phase in the migraine cycle. Currently, although there is a lack of evidence supporting the "generator" theory, PAG is undoubtedly associated with the modulation of migrainous pain [7][44]. Studies have shown that stimulating the PAG or blocking its P/Q-type calcium channels inhibits and facilitates, respectively, the activity of SpVC neurons [37]. Furthermore, bilateral projections of PAG to the RVM are interpreted as a modulatory circuit that controls pain processing to the spinal dorsal horn. In fact, RVM cells affect how the neurons respond to noxious stimulation and alter the perception of craniovascular inputs, such that the "on" cells are inhibited by opioids and stimulate the firing of neurons after receiving nociceptive signals, and the "off" cells are stimulated by opioids and inhibit the neuronal firing [14][37].

Considering the existence of these pain-related circuits, it is interesting to mention the pain modulation processes in migraine treatments. Triptans (mentioned in section 2.1.1. as an acute therapy) are selective 5-HT$_{1B}$ and 5-HT$_{1D}$ serotonin receptor antagonists that disturb the interconnections between the peripheral and central TV neurons. According to preclinical studies, these molecules can reduce the release of vasoactive neuropeptides (e.g. CGRP and substance-P) to the TG and trigeminal nucleus by vasoconstriction of arterial vasculature [7][45]. Also, ditans are 5-HT$_{1F}$ receptor antagonists that inhibit the activity of cells in the trigeminal nucleus caudalis with trigeminal stimulation [7]. More recent drugs, such as anti-CGRP monoclonal antibodies and onabotulinumtoxin-A, inhibit the activation and sensitisation of meningeal nociceptors hampering the activity of Aδ- and C-fibers, respectively [45].

Hence, this overview shows that migraine is not a common headache, but a burdensome multifactorial disorder involving complex, interlinked pathophysiological mechanisms and modulatory systems.

In the last two decades, technologies to investigate migraine pathophysiology progressed greatly, including novel biochemical, genetic, electrophysiological and neuroimaging studies [9].

Functional neuroimaging techniques have become an indispensable tool in migraine research and driven robust advances in understanding its generation, progression, chronification and treatment [10]. In particular, fMRI has been widely explored to understand the mechanisms involved in migraine sensory (visual, auditory, olfactory, painful) hypersensitivities by measuring brain changes in response to external stimuli, as well as to decoding the functional architecture and network organisation of the migraine brain throughout the cycle, by studying FC of patients at rest [46]. Thus, emerging migraine studies in pair with new optimized approaches may contribute to garnering new insights regarding migraine-specific brain alterations and identifying biochemical, genetic and/or imaging clinical biomarkers able to ensure a more accurate diagnosis of the disorder, better prediction of each individual's response to treatment, and, potentially, recognition of targets to develop novel therapeutics.

## 2.2. Functional Magnetic Resonance Imaging

fMRI is a high spatial resolution and non-invasive magnetic resonance imaging (MRI) technique that emerged in the 1990s. This approach detects real-time information in terms of cerebral blood flow, which most likely reflects neurotransmitter action and, for that reason, is considered an indirect measure of neuronal activity [10]. Therefore, fMRI has become a leading and valuable research tool for mapping the activity of the human brain and exploring its function and dysfunction [47].

### 2.2.1. Basic principles

#### 2.2.1.1. Magnetic Resonance Imaging

MRI is a technique based on the phenomenon of nuclear magnetic resonance, which arises from the interaction of atomic nuclei, mainly hydrogen ($^1$H) in water molecules, with an externally applied magnetic field [48]. Atoms with an odd number of protons and/or neutrons present an inherent spin angular momentum that acts as a magnetic dipole due to its electrical charge.

In the absence of an external magnetic field, the individual magnetic moments of the patient's nuclei are randomly oriented and cancel each other, so that the net magnetisation is null [49]. However, when the patient is placed in the scanner, a static magnetic field ($B_0$) derived from a strong magnet is applied in the longitudinal or *z*-direction (corresponding to the patient's long axis), which leads to two notable phenomenons: on the one side, the magnetic moments of the nuclei align parallel or antiparallel to $B_0$, being tendentially more oriented in the same sense of $B_0$ since it corresponds to the minimum energy state; on the other side, according to the Classical Theory of Electromagnetism, spins exhibit resonance at a well-defined Larmor frequency ($\omega_0$), proportional to the hydrogen nucleus's gyromagnetic constant and the strength of $B_0$. This precession frequency originates a non-null net magnetisation across all spins that stabilises in the equilibrium magnetisation state, and the patient becomes polarised [50].

In order to obtain the MR signal, it is necessary to apply an oscillating electromagnetic radiofrequency (RF) field ($B_1$), weaker than $B_0$, with an excitation frequency that equals $\omega_0$. This RF pulse excites the nuclei from the lower to the higher energy state (parallel to antiparallel conformation, respectively) and flips the net magnetisation to the transverse or *xy*-plane, perpendicular to $B_0$. Hence, spins are in phase and precessing around a field resulting from the sum of the static and oscillating ones [49].

When the application of $B_1$ is stopped, the spins return to the lower energy state, and the magnetisation vector decays back to thermal equilibrium in a process known as relaxation, which occurs in the longitudinal and transverse directions. It is worth noticing that the contrast mechanism in MRI derives from differences in the relaxation times between tissues. The longitudinal relaxation (re-growth of the vector component into the *z*-direction) is characterised by the time constant $T_1$ and corresponds to the transference of energy from the spin to the surrounding lattice due to the transition between states with different energy [51]. The transverse relaxation (decay of the vector component into the *xy*-plane), in ideal conditions of $B_0$ homogeneity, is characterised by an exponential signal decay, or free-induction decay (FID), controlled by the time constant $T_2$, which is measured by RF coils placed within the scanner and converted into a measurable signal [50]. In practice, magnetic field inhomogeneities change locally and randomly the precession frequency of the spins, such that there is a loss of phase coherence (spin dephasing) and the relaxation is faster, being characterised by the time constant $T_2^*$ (lower than $T_2$). In the brain, the field inhomogeneities can also arise from the composition of the local blood supply, which depends on the cellular metabolic needs and, thus, is used as an indirect measure of neural activity. This correlation is the core of the Blood Oxygen Level-Dependent (BOLD) contrast used in BOLD-fMRI to map brain function [48].

### 2.2.1.2. The Blood Oxygen Level Dependent signal

The BOLD signal was first described by Ogawa and colleagues in 1990 and is the most commonly used contrast mechanism in fMRI [52]. The concept underlying this mechanism is that local neuronal (electrical and synaptic) activity is tightly correlated with changes in haemodynamics, including regional cerebral blood flow (rCBF) and volume (rCBV) and blood oxygenation, through a process known as neurovascular coupling. This phenomenon produces an effect that is measurable in MR images [52].

According to the neurovascular coupling, the activation of brain areas increases the regional cerebral metabolic rate of oxygen (rCMRO$_2$) and glucose (rCMR$_{glu}$) required for cellular metabolism, which is ensured by the haemodynamic response that, through local vasodilation, leads to an augmented rCBF and rCBV. In order to guarantee that the local influx of oxygen is higher than the consumption rate, the rCBF needs to be larger than the rCMRO$_2$. Therefore, there is an increase in blood oxygenation in response to neural activation, which reflects a net increase in the balance between oxygenated arterial blood to deoxygenated venous blood, and, consequently, a higher BOLD signal in the activated brain region compared to the surrounding tissue (see Figure 2.4.) [8][48].

The BOLD contrast is sensitive to changes in the regional concentration of blood oxyhaemoglobin (HbO$_2$) and deoxyhaemoglobin (dHb) within the brain, since these are coupled to subtle alterations in the magnetic field surrounding the red blood cells. The HbO$_2$, saturated with oxygen molecules, is diamagnetic, being magnetically indistinguishable from the surrounding tissue. The dHb, deoxygenated and with four unpaired electrons, is paramagnetic. This paramagnetism leads to susceptibility effects in the surroundings of these molecules that result in local magnetic field inhomogeneities and thus cause spin dephasing and geometric distortions. Therefore, this phenomenon reduces $T_2$ (intravascular signal) and $T_2^*$ (extravascular signal) time constants, leading to BOLD signal losses. In the same reasoning, an increase in blood oxygenation leads to an augmented ratio of HbO$_2$ to dHb, which enhances the $T_2^{(*)}$ and therefore the BOLD signal, corresponding to a brighter region on the MRI [8][47].
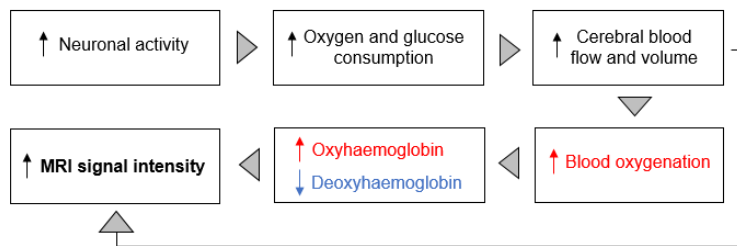
Figure 2.4. Schematic representation of the neurovascular coupling mechanism.

One should note that the BOLD signal response is much slower than the underlying neuronal activity, being modelled by the haemodynamic response function (HRF) that limits the temporal resolution of fMRI. Typically, the HRF presents a width of approximately 3 s and a peak between 5 s to 6 s after the stimulus onset, returning to baseline about 12 s after the stimulus onset [8][47].

In theory, the BOLD signal corresponds closely to local field potentials (LFP) of a neural population (i.e., a weighted average of synchronised dendro-somatic components from synaptic signals), such that it can be roughly approximated by the convolution of the LFP with the HRF. Nevertheless, according to the Linear Transform Model, assuming that the BOLD response is linearly dependent on neural signals under certain conditions and that the relationship between the BOLD signal and the neuronal response displays linear and time-invariant (LTI) properties, the neural responses to individual events add linearly to yield the expected BOLD response (see Figure 2.5.). In those conditions, the BOLD signal can be predicted as the convolution of neuronal activity with the HRF [48][53][54].
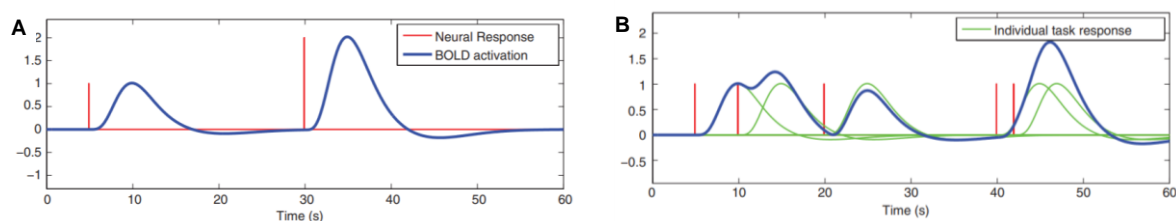


Figure 2.5. BOLD signal response modelled by the HRF, following the LTI properties, with **A** displaying separately distributed neural events and **B** representing neural responses close together in time. The property of linearity of the BOLD response stands for (i) if a neural response is scaled by a factor, the BOLD response will be scaled by the same factor and (ii) if two neural events occur close in time, the expected BOLD reponse is a linear addition of both. The property of time invariance demonstrates that if a neural reponse is shifted in time, the BOLD response will also be shifted by the same amout of time. Figure extracted from Poldrack et al. [53].

The basic principle of BOLD-fMRI consists of acquiring sequential low-resolution brain volumes (each one with multiple slices composed by voxels), from which it is possible to detect variations in the BOLD signal. The typical image readout sequence used for BOLD-fMRI acquisition is echo-planar imaging (EPI) due to the BOLD contrast sensitivity and imaging speed. However, this technique presents limited temporal resolution, with a slow temporal sampling of the haemodynamic response and susceptibility to artefacts near the air-tissue boundaries [8][53]. To overcome these caveats, new directions for imaging technology have arisen over the years, namely simultaneous multislice (SMS) and 3D imaging techniques, which improved acquisition speed and signal-to-noise ratio (SNR). The use of ultra-high fields (7 Tesla or higher) in fMRI experiments can also be used to increase the available SNR and contrast-to-noise ratio (CNR) [55].

The BOLD-fMRI acquisition can be performed using a task-based or stimulus-driven paradigm, which

compares stimulus-evoked responses with a matched baseline task, or a resting-state paradigm, which corresponds to a condition with the absence of external stimuli or imposed tasks [8]. The use of fMRI experimental designs with task-based paradigms makes it possible to determine which brain regions show an increased intensity of the BOLD signal when a task or stimulus is imposed, which contributes to studying the localised brain activity and function. Furthermore, throughout the years, rs-fMRI has gained widespread acceptance in the neuroscience community as an increasingly powerful technique to explore spontaneous brain activity and functional co-activation patterns for characterising the brain's spatiotemporal organisation and mapping brain function [8][56].

## 2.2.2. Resting-state fMRI and Functional Connectivity

The human brain can be interpreted as an integrative network derived from complex interactions between brain regions with some degree of FC. FC can be defined as the coherence (or statistical temporal dependence) of BOLD signal fluctuations between distinct brain regions [56].

rs-fMRI is the area of application of BOLD-fMRI that allows studying the intrinsic brain FC. This technique focuses on the spontaneous low-frequency fluctuations (usually between 0.01 Hz and 0.1 Hz) of the BOLD signal, reflecting the brain baseline activity. In a typical rs-fMRI experiment, participants are placed into the MR scanner and asked to keep their eyes opened or closed and not think of anything in particular without falling asleep, while the intrinsic brain activity is measured [56][57]. This approach presents several technical advantages over other fMRI techniques, namely the facility in the signal acquisition, reduced burden of experimental design or training demands, the low effort required from the patients, reduced susceptibility to (head) motion artefacts and proficiency in detecting different functional areas in patient populations [56][57].

Over the past years, rs-fMRI studies have identified resting-state networks (RSNs), i.e., intrinsic connectivity networks composed of brain areas with low-frequency synchronous fluctuations, which reproduce the functional architecture of the brain [57][58]. In 1995, Biswall and colleagues demonstrated the first significant BOLD signal functional correlations within the sensorimotor or somatomotor network (SMN), between the left and contralateral sensorimotor cortices [59][60]. Furthermore, emerging rs-fMRI studies have allowed the identification of standard repertoires of functional subsystems over the years. The Yeo's template [61] was obtained with a surface vertex clustering analysis and includes seven RSNs – visual (VN), SMN, ventral attention (VAN), dorsal attention (DAN), limbic (LN), frontoparietal (FPN) and default mode (DMN) networks. Moreover, the Smith's template [62], originated by an ICA analysis, comprises ten RSNs, which include a sub-divided VN – visual medial (VMedN), visual occipital (VOccN) and visual lateral (VLatN) networks, a sub-divided FPN – right and left FPN (R FPN and L FPN, respectively), the DMN, SMN, auditory (AudN), executive control (ECN) and cerebellar (CbN) networks.

All of the RSNs mentioned before except for the DMN are task-positive, meaning that voxels belonging to those get consistently more activated in active-task conditions. In contrast, the DMN is task-negative, since it includes regions that are more intensely correlated during rest and present reduced activity when a cognitive task is performed. Recently, more attention has been given to the DMN in the clinical and research communities [60][62]. A global description of the anatomical and functional characteristics of each standard RSN based on a literature review is presented in Table 2.1.

Table 2.1. Anatomical and functional description of the most common RSNs reported in the literature.
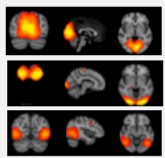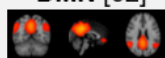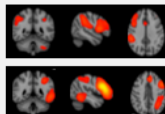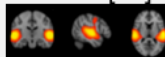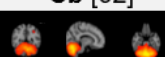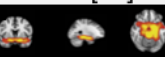
| RSN | Anatomical areas | Associated function |
|---|---|---|
| **VN** [62]<br>VMedN, VOccN and VLatN<br> | Med/BLatCalSul; PerStrA; MedVAs (LinG, lPrecun, LatGenN of Th); LatVAs (TOcc junction); S/LatOccG; Occ pole [57][62]. | Visual behavioural domain. Processing of simple visual stimuli (VMedN), e.g. flickering checkerboard; complex emotional stimuli (VLatN) corresponding to a cognition-space paradigm; and high-order visual stimuli (VOccN) corresponding to a cognition-language-orthography paradigm [62][63]. |
| **DMN** [62]<br> | MedParC (PrecunC, A/PCC); BLatl/LatParC; VentMedFC [62]. | Self-related and introspective mental processes, e.g. mind-wandering, daydreaming, social cognition, self-monitoring, stimulus-independent thoughts and integration of cognitive processes. Deactivation during a goal-directed behaviour [63][64]. |
| **SMN** [62]<br> | S1; S2; M1; PreMoC; SuppMoA; MCC; SMC; BLatMFG [63]. | Action-execution motor tasks and perception-somesthesis paradigms [62]. |
| **FPN** [62]<br>R FPN and L FPN<br> | M/IFG; Precun; lParC; AnG [60]. | Attention, cognition, language, memory, decision-making, visual processes and perception-somesthesis-pain [62][64]. |
| **AudN** [62]<br> | Prim/AssAudC (BLatSTG, Heschl'sG, PInsC) [62][63]. | Action-execution paradigm, cognition-language paradigm and perception-audition-speech paradigm [62]. |
| **ECN** [62]<br> | MedFAs (S/MedFG, A/ParaCC, VentLatPFC, Th) [63]. | Regulation of executive/cognitive functions, e.g. endogenous attention, goal-directed planning, decision-making, working memory, language paradigms (L EC), perceptual, somesthetic and nociception processing (R EC) [63][65]. |
| **DAN** [66]<br> | S/MFG; LatOccC; IntraParC; FEF [64][65]. | Cognitive selection of relevant sensory information (top-down system), stimulus processing and preparation of responses of action selection. Activation when attention is overtly/covertly oriented in space [65][67]. |
| **VAN** [68]<br> | TPar junction; IFC [65]. | Detection of sensory salient stimuli. Activation when behaviourally unexpected stimuli appear outside the cued focus of spatial attention [65][67]. |
| **Cb** [62]<br> | Cb [62]. | Action-execution and perception-somesthesis-pain domains [62]. |
| **LN** [69]<br> | Amg; HC; Ins; HTh; NAc parts [69]. | Emotional processing and regulation and processing of encoding memories [69]. |

Table 2.1. *(Continued)*

| RSN | Anatomical areas | Associated functions |
|---|---|---|
| **SN** [66]  | BLat Ins; DACC; PreSuppMoA [63]. | Control of cognition and pain-related processes, orientation toward conflict monitoring, information integration, salient emotional stimuli and response selection. Regulation of transition between internal attention and task-related states, and of dynamic changes in others RSNs [63]. |

**Abbreviations**: **A** = Anterior; **An** = Angular; **Amg** = Amygdala; **Ass** = Association; **Aud(N)** = Auditory (Network); **BLat** = Bilateral; **C** = Cortex; **CalSul** = Calcarine Sulcus; **CC** = Cingulate Cortex; **Cb(N)** = Cerebellum (Network); **D** = Dorsal; **DAN** = Dorsal Attention Network; **DM(N)** = Defaut Mode (Network); **EC(N)** = Executive Control (Network); **F** = Frontal; **FAs** = Frontal Areas; **FEF** = Frontal Eye Field; **FPN** = Frontoparietal Network; **G** = Gyrus; **GenN** = Geniculate Nucleus; **HC** = Hippocampus; **HTh** = Hypothalamus; **I** = Inferior; **Ins** = Insula; **L** = Left; **LN** = Limbic Network; **Lat** = Lateral; **Lin** = Lingual; **M** = Middle; **M1** = Primary Motor Cortex; **Med** = Medial; **NAc** = Nucleus Accumbens; **Occ** = Occipital; **P** = Posterior; **Par** = Parietal; **PerStrA** = Peristriate Area; **PF** = Prefrontal; **Precun** = Precuneus; **Prim** = Primary; **R** = Right; **S** = Superior; **S1** = Primary Somatosensory Area; **S2** = Secondary Somatosensory Area; **SM(N)** = Somatomotor (Network); **SN** = Salience Network; **SuppMoA** = Supplementary Motor Area; **T** = Temporal; **Vent** = Ventro; **VAs** = Visual Areas; **VAN** = Ventral Attention Network; **V(N)** = Visual (Network).

In summary, fMRI connectivity studies contribute to a more detailed brain characterisation concerning the FC strength within each network (functional segregation) and large-scale neuronal communication between different networks (functional integration). Advances in this field may provide new insights regarding healthy brain functioning and the disruption from the normal brain condition in neurological and neuropsychiatric disorders [56][57].

### 2.2.2.1. Preprocessing

The neuronal activity that induces the BOLD-fMRI response only accounts for a small ratio of the total variance of the signal. The predominant non-neuronal contributions may include thermal noise (derived from the electrical circuits of MR signal reception), instrumental drifts, and artefacts derived from hardware instabilities, head motion and non-neuronal physiological fluctuations (e.g. signals derived from the pulsatile flow of cardiac cycle through the brain, respiration, alterations in the concentration of arterial $CO_2$ due to the changing respiration rate, vasomotion effects and changes in blood pressure and cerebral autoregulation mechanisms) [63][64].

Since the rs-fMRI analysis investigates the correlation between BOLD time courses through the brain without any prior knowledge about the signal of interest, the presence of noise and artefacts that might share some spatial and spectral overlap with RSNs reduces the SNR and the quality of the BOLD signal, affecting the identification of the RSNs and, consequently, the analysis of FC [65]. Furthermore, in dFC analysis, the presence of noise can mislead the assignment of dynamic changes to neural activity [66][67]. Thus, to improve the relative validity of the FC estimates, the BOLD signal must undergo preprocessing, as will be further explored in section 3.2.1. of the present work. Typical preprocessing steps include motion correction, distortion correction, slice-timing correction, physiological noise correction, spatial smoothing, temporal filtering, and registration to standard space [53][66].

### 2.2.2.2. Parcellation

The organizational principles of the human brain are extremely complex due to the existence of vast microarchitectures, topographies, connectivities and functionalities [68]. Furthermore, the enormous

dimensionality of the fMRI datasets would hamper an efficient and fast extraction of information for further analyses if BOLD signals from all brain voxels were considered individually [69].

Hence, the concept of brain parcellation has become widely used in neuroscience, which consists of dividing the brain into anatomically and/or functionally distinct regions of interest (ROIs) and average the BOLD time courses of the voxels belonging to each ROI [70].

Not only can brain parcellations reduce the extremely high dimensionality of rs-fMRI data into a set of manageable sets of regions and increase the SNR (by reducing the noise through averaging), they also provide fundamental insights regarding the whole-brain activity and functional architecture, which contributes to decoding the human brain in terms of predicting behavioural/clinical phenotypes from brain imaging data. Furthermore, this method makes the comparison of FC results across studies more efficient, as the FC is analysed within specific ROIs and not in hundreds of thousands of voxels [68][70][71]. However, parcellating the rs-fMRI has some inherent limitations, such as the loss of a detailed connectome within each ROI and the counter-intuitive down-sampling of the data by averaging BOLD signals in pair with efforts to increase the spatial resolution of fMRI sequences [69].

Over the past few years, much progress has been made in defining new types of brain parcellations, including cortical and subcortical regions, through model-driven or data-driven approaches.

The model-driven methods use standard predefined anatomical templates that divide the brain according to histological and microstructural properties (cyto- or myelo-architectonic information), ensuring spatial contiguity and non-overlap of brain regions. Some examples are the AAL [72], Desikan [73] and Harvard-Oxford atlases. However, this type of parcellation does not require the defined ROIs to present FC homogeneity, and since the atlases derive from a higher resolution source than the majority of fMRI data, their application at the fMRI scale may give rise to partial volume effects (PVEs) and co-registration errors [74].

In turn, data-driven approaches generate ROIs by parcellating the whole rs-fMRI data into spatially coherent regions that show maximum functional homogeneity without including anatomical priors (FC-based parcellation strategies). For that purpose, spatially constrained clustering techniques, such as the ICA, k-means and hierarchical clustering, are used [53][68][70]. Some templates obtained by this type of approach are Yeo repertoire [61], Smith repertoire [62] and Craddock atlas [74]. Nevertheless, one should note that these parcellation schemes do not guarantee spatial contiguity [74].

Besides the variety of methods to parcellate the brain, there are distinct sources of reference data through which the templates are created and different objectives that drive their creation (for example, to track a specific brain structure or functionality).
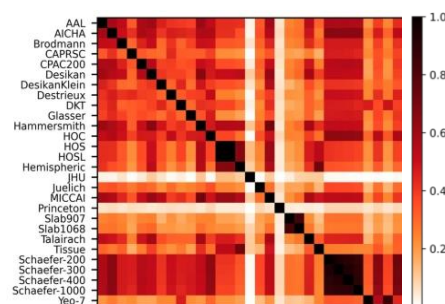


Figure 2.6. Adjusted mutual information scores between different brain parcellation schemes. Figure adapted from Lawrence et al. [71].

Figure 2.6. shows the variable degree of similarity (adjusted mutual information scores) between different templates [71].

Thus, the peculiarities of each approach and the complementary information they provide together justify the importance of comparing distinct parcellation schemes during data analysis to provide a more complete interpretation of results.

### 2.2.2.3. Static FC analysis

Assuming stationarity of FC over a full rs-fMRI scan, with the underlying brain connections being constant over time, the sFC can be analysed in preprocessed data through several methods. The most common are model-dependent methods, which are limited to local connectivities and require prior information or a predefined model (seed-based correlations, regional homogeneity (ReHo) and amplitude of low-frequency fluctuations (ALFF)) and exploratory data-driven approaches that look for general FC patterns at a whole-brain level (principal component analysis (PCA), ICA and clustering) [8][56].
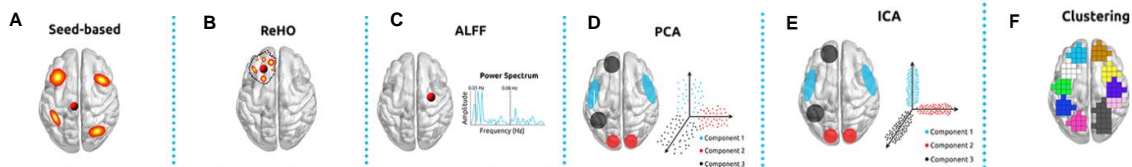


Figure 2.7. Common methods used to study static FC in rs-fMRI data. **A:** Seed-based correlations; **B:** ReHo; **C:** ALFF; **D:** PCA; **E:** ICA; **F:** Clustering. Figure adapted from Soares et al. [8].

The seed-based correlational analysis (Figure 2.7.A) was the first method of sFC to be implemented to rs-fMRI data by Biswal and colleagues [59] and is currently the most straightforward approach to assess the activity of a specific ROI (seed), which can correspond to one single voxel or a set of voxels. This technique correlates the averaged BOLD time courses of voxels belonging to the seed with the time series of all remaining voxels of the brain. Therefore, with the application of a threshold, it is obtained an FC map that provides information about which voxels are significantly correlated (or functionally connected) to the seed and to what extent, allowing to detect both long- and short-distance connections between the seed and other brain regions [56][75].

Then, the ReHo method (Figure 2.7.B) relies on the assumption that a given voxel is temporally similar to its closest neighbourhood [76]. It can be applied in a predefined ROI, although that is not a mandatory condition, and measures the synchronisation between the BOLD time course of a given voxel with the ones of its nearest neighbours, in a voxel-wise approach, using Kendall's coefficient of concordance. In contrast to seed-based correlational analysis, ReHo studies local spontaneous activity and short-distance connections, providing information about brain regional activity [8].

The ALFF method (Figure 2.7.C), or the most recent fractional ALFF technique (fALFF) with reduced sensitivity to physiological noise, measures the magnitude of signal amplitude on a voxel-by-voxel way, reflecting the intensity of spontaneous regional activity. The (f)ALFF can be obtained by transforming each voxel's time series to the frequency domain (power spectrum) and then computing the amplitude at each frequency, since the power of a frequency is proportional to the square of the amplitude of this frequency component. Finally, the averaged amplitude is computed at each voxel in the low-frequency range (typically 0.01-0.1 Hz) [8][77]. Similar to the ReHo, this approach analyses spontaneous activity at a local level, and since both metrics express different properties of BOLD signal (synchronisation and

amplitude, respectively), they are commonly used as complementary analyses [8].

Regarding the PCA (Figure 2.7.D), it is a method that searches for a set of principal components (PCs), each of them corresponding to a direction in the dimensional space of input data (orthogonal axes). In practice, data can be explained as a linear combination of all PCs, as they together maximise the explained variance of the data and separate relevant information from noise. The efficacy of this technique depends on assumptions of linearity and orthogonality of PCs and high SNR [8].

Furthermore, the ICA (Figure 2.7.E) is a blind-source separation technique that finds a mixture of sources that minimises the statistical dependence between its underlying components [78]. When implemented in rs-fMRI analysis, ICA decomposes the 4D fMRI dataset into statistically independent spatial-temporal components (ICs) described by a spatial map modulated in time by the series of the respective component. This data-driven approach has been widely used in several studies with the significant advantage of requiring few prior assumptions. Nevertheless, it requires the user to visually and manually ascertain the ICs of interest corresponding to brain networks, correlate them with predefined RSN templates and discard those associated with noise [75].

Finally, clustering methods (Figure 2.7.F) divide data into non-overlapping clusters that maximise the degree of similarity within each group and minimise the similarity between different groups [56]. The cluster assignment is based on the distance of each data point to the cluster centroid, which is typically computed through an average of its members. Each iteration of the algorithm updates the cluster centroids and memberships, and the algorithm halts when the centroids stabilize and the defined number of iterations is achieved (i.e., until convergence of results) [79]. In rs-fMRI analysis, data are segmented into clusters of brain voxels with correlated BOLD time courses and, thus, FC [8].

Over the past years, all metrics described above have provided new insights regarding the rs-fMRI signal, and, currently, they are still widely used to analyse brain FC. However, the estimation of FC over an entire rs-fMRI scan with the prior assumption that it does not change over time started to be interpreted as too simplistic to capture the full extent of resting-state activity [80]. Indeed, at rest, the dynamic aspects of fMRI are even more notable since the mental activity is unconstrained [66].

Hence, in the 2000s, studies suggesting the dynamic behaviour of FC on short-time scales started to arise throughout ageing, development, visual state and even as a function of attention, conscious awareness, learning and muscle fatigue. In 2010, the investigation from Chang and Glover demonstrated for the first time the unambiguous dynamic behaviour of FC with fluctuations in the time scale of seconds to minutes [66]. Throughout the years, the limitations of sFC analysis and improvements in recording methods shifted the attention to the concept of dFC and the implementation of new methods to analyse FC, as explored in the next section in more detail.

### 2.2.2.4. Dynamic FC analysis

In contrast to conventional sFC, the study of dFC addresses variations in the FC over time (i.e., across the duration of a scan), which allows the detection of time-varying patterns of neuronal connectivity and the appearance of significant brain networks. These are not so easily identified in sFC analysis and can be particularly prominent when comparing the FC of healthy and diseased brains [81]. Up to now, some analytical pipelines have been implemented to estimate the dFC, including the SW, PC and time-frequency analysis.

**(i) Sliding Window method**

The SW has been the most common and straightforward approach for analysing dFC [82]. This method segments fMRI data in successive intervals of time (temporal windows), within which the FC is described between each pair of brain regions by computing a pairwise (typically Pearson) correlation between their respective BOLD time courses [83].

For a sliding window with length $W$ (i.e., that spans the temporal period from $t$ to $t + W - 1$) shifted by a step $S$ that defines the degree of overlap between successive windows after calculating the FC metric of interest (*corr()*), the dFC between two brain regions $n$ and $p$ at each time point $t$ can be given by the Equation (2.1):

$$dFC(n,p,t) = corr(x_{n,t}^{t+W-1}, x_{p,t}^{t+W-1}) \qquad (2.1)$$

where $x_{n,t}^{t+W-1}$ and $x_{p,t}^{t+W-1}$ are the BOLD time courses of the brain regions $n$ and $p$, respectively, segmented in time from $t$ to $t + W - 1$. This process is repeated until the window reaches the end part of the whole time course [80][84]. That way, considering the brain parcellated into $N$ regions, the functional connections between all regions can be described in connectivity matrices with size $N \times N$ per window (time) that reflect the temporal evolution of the FC through the whole brain, as schematically illustrated in Figure 2.8. Since the sFC matrices are symmetric, only the upper (or lower) values in relation to the diagonal ($N\times(N-1)$/2 elements) yield relevant information [80].
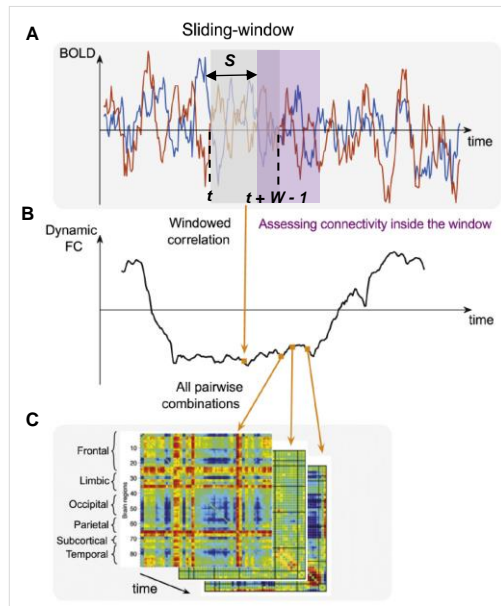


Figure 2.8. SW methodology to estimate dFC. **A:** BOLD time courses (brown and blue) from two brain ROIs and a temporal window (grey) that spans the temporal period from $t$ to $t + W - 1$, shifted by a step $S$ that defines the degree of overlap between successive windows, within which the parwise correlation is computed; **B:** Connectivity time course obtained from computing the pairwise correlation between the time series of the two ROIs within the temporal window over time; **C:** dFC matrices representing the FC between each pair of ROIs over time. Figure adapted from Preti et al. [80].

One should note that, although the Pearson correlation coefficient is the most common metric used to estimate FC in the SW approach, other possibilities have already been used, namely ReHo and ICA. For example, in the case of SW-ICA, the decomposition of BOLD time courses with ICA yields spatial maps of RSNs over time [84].

The SW provides a simple pipeline to obtain FC estimates, and its robustness makes it less susceptible to noise than other techniques, such as the PC. Notwithstanding, it entails several limitations. The estimation of FC within the sliding window compromises the temporal resolution of the method, and the choice of a fixed-length window precludes the detection of dFC fluctuations with durations below that size. Thus, the choice of the window length is a trade-off: it should be short enough to detect potentially FC variations of interest without introducing spurious fluctuations (sensitivity), but long enough to ensure a reliable estimation of FC (specificity) and resolve the lowest frequencies of interest in the signal and [80][84]. Although there is no ideal size, previous studies revealed that durations of 30 s to 60 s produce robust results of FC [84]. Furthermore, the window step is commonly set to one repetition time (TR), which is the period between the application of consecutive RF pulses (corresponding to one time frame or volume) [82].

Another pitfall of this technique is the window shape. The rectangular window, which is the most commonly used, assigns equal weights to all observations inside the window. However, this increases the risk of including/excluding outliers that appear as instantaneous noisy observations, leading to sudden misunderstood changes in dFC [80]. A possible solution to that problem is selecting tapered windows with weighted edges (e.g. by convolving a rectangular window with a Gaussian kernel) [11].

**(ii) Phase Coherence method**

The PC method characterises the time-varying single frame FC by comparing instantaneous phase information between BOLD time courses of different brain regions. The degree of phase synchronisation, also called PC, is a measure of dFC [85].

The first step of the PC method is the conversion of the band-pass filtered BOLD signal ($x(t)$) into its complex analytic version ($x_a(t)$), meaning the separation of its instantaneous amplitude from its instantaneous phase (Equation (2.2)). This signal decomposition can be performed using processing techniques like the Hilbert transform, Wavelet filtering or Gabor expansion [85]. In the present work, the Hilbert transform approach was implemented:

$$x_a(t) = x(t) + jH[x(t)] \tag{2.2}$$

where $j$ is the imaginary unit and $H[\cdot]$ the Hilbert transform.

Assuming that $x(t)$ is a narrowband signal, it can be represented by the product of an amplitude-modulated low-pass signal, $a(t)$, with a sinusoidal carrier frequency, $\theta(t)$, such that:

$$x(t) = a(t)cos\left[\theta(t)\right] \tag{2.3}$$

If the Bedrosian's theorem is respected, then the Hilbert transform of $x(t)$ can be rewritten as follows:

$$H[x(t)] = a(t)sin\left[\theta(t)\right] \tag{2.4}$$

Therefore, the analytic signal can be defined by Equation (2.5), using Euler's formula:

$$x_a(t) = a(t)e^{j\theta(t)} \tag{2.5}$$

where $a(t)$ is the instantaneous amplitude and $\theta(t)$ the instantaneous phase [85].

After estimating the phases of BOLD signals, the dFC between two brain regions *n* and *p* at each time point *t* can be given by their PC, which is computed through the Equation (2.6):

$$dFC(n, p, t) = PC(n, p, t) = cos\ [\theta(n, t) - \theta(p, t)] \tag{2.6}$$

Thus, if two brain regions have synchronised BOLD signals at the same instant (i.e., $\theta(n, t) = \theta(p, t)$), they have no phase difference, such that $dFC(n, p, t) = PC(n, p, t) = 1$. Following the same reasoning, orthogonal BOLD signals will present null PC and dFC [86]. Considering the brain parcellation scheme of *N* regions, it is possible to obtain a whole-brain pattern of BOLD PC over time, represented by symmetric dFC matrices with size *N x N* per TR.

The implementation of the PC method has been widely recognised in magnetoencephalography (MEG) and electroencephalography (EEG) studies, being still an emerging tool in fMRI [85]. Since this method uses instantaneous BOLD phase alignments to characterise FC, it presents more sensitivity to noise fluctuations than the SW, because random fluctuations of BOLD phases with small phase differences between them may lead to spurious connections [87]. However, PC reveals substantial advantages compared to SW. First of all, the PC method computes the dFC at each TR, which guarantees a maximum temporal resolution and ensures a more accurate analysis of the faster dFC fluctuations. Moreover, since this metric is applied instantaneously for each time point and the whole brain with one transform, it is computationally faster than temporal correlations. Also, since the PC is a non-linear measure, it is more suitable to detect complex dynamic processes in the brain [85].

### (iii) Time-frequency analysis

The time-frequency analysis quantifies the correlation between BOLD time courses of different brain regions as a function of both time and frequency, by analysing their coherence and phase lag [66][82].

One way to implement this method is resorting to the Wavelet Transform Coherence (WTC). The WTC decomposes the BOLD time series into the time-frequency space through the convolution of the time course with scaled and translated versions of a wavelet function [66]. The implementation of time-frequency analysis with the WTC overcomes the limitation of the SW of requiring a fixed window size. Instead, the scale of the wavelet (effective analysis window) is adapted to the frequency of the signal, such that shorter time windows are implemented in higher frequencies (faster changes, better spatial resolutions) and larger time windows to lower frequencies. That way, this method allows to characterise the coherence between brain regions and networks at multiple frequencies and study the temporal variability in the amplitude and phase relationships between brain regions at each time-frequency point. Nevertheless, the abundance of information obtained with this type of implementation makes it difficult to scale up to multiple brain regions and subjects [84][88].

### 2.2.2.5. dFC states

The direct analysis of dFC time courses would be highly burdensome due to their dimensionality. Also, several studies have revealed that FC displays quasi-stable recurrent synchronisation patterns that resemble well-established functional networks instead of varying randomly over time. Hence, the organisation of FC fluctuations into dFC states is extremely relevant to their interpretation [11].

The estimation of dFC states from multi-dimensional data can be computationally faster and more

efficient if the input dimensionality is significantly reduced. A way to perform this reduction is by applying the Leading Eigenvector Dynamic Analysis (LEiDA) proposed by Cabral and colleagues [83][86][89]. LEiDA focuses on the dominant FC pattern of the data by considering the leading eigenvector ($V_1$) of the dFC matrix at each time point ($N$ elements per time) instead of the whole dFC matrix ($N \times N$ elements per time or, in practice, non-redundant $Nx(N-1)/2$ elements per time) [86]. The $V_1$ is associated with the largest magnitude eigenvalue and explains the majority (over 50 %) of data variance [89].

Beyond the reduced dimensionality that LEiDA ensures, it provides a clearer and more rigorous detection of recurrent patterns and epochs at which the dFC variance becomes dominated by a different pattern, being also more robust to high-frequency noise [86].

Thereafter, the estimation of dFC states can be performed by implementing matrix factorisation techniques into FC data (or the respective leading eigenvectors) over time, such as k-means clustering, PCA and dictionary learning. Commonly, these methods are implemented across subjects, allowing for a dFC characterisation of the entire group that participated in the rs-fMRI acquisition [80].

The k-means clustering algorithm is a clustering technique introduced by Allen and colleagues [11] that groups the dFC matrices over time into non-overlapping clusters. Each cluster is characterised by a centroid vector representing a recurrent dFC state, and dFC matrices are described at each time point by a single state to which they present the highest similarity (shortest distance to the centroid). The requirement of a predefined number of clusters to implement this algorithm makes it susceptible to getting different results, which may interfere with the interpretation of the FC states [11][80].

In contrast to k-means clustering, in which the centroids are mutually exclusive in time, PCA and dictionary learning approaches allow temporal overlap between states. In PCA, the dFC matrices are decomposed as a linear combination of all FC patterns (known as eigenconnectivities) with time-varying associated weights [90]. Instead, in dictionary learning, the dFC matrix is a linear combination of a subset of dFC states with a certain degree of temporal sparsity [91].

After estimating the dFC states, they can be characterised in terms of their occurrence throughout time using predefined temporal metrics: the mean lifetime (or dwell time), which corresponds to the mean number of consecutive epochs in the given state; the probability of occurrence (or fractional occupancy), which is the fraction of epochs the state occurred throughout the scan; and, finally, the switching profile, which summarises the probabilities of switching from a given dFC state to another [86].

## 2.3. State-of-the-art

Functional neuroimaging studies are a crucial tool to understand migraine pathophysiology, helping to identify potential brain regions involved in the onset of migraine attacks and determine the clinical significance of brain dysfunction associated with the disorder [92].

Over the years, much progress has been made in migraine research. Most investigations focused on stimulus-induced brain activation and processing, involving the exposure of interictal migraineurs to visual, olfactory, skin noxious thermal stimulation and trigemino-nociceptive activation by intra-nasal ammonia, and the comparison of results with healthy controls. Consistent observations have also been reported in terms of altered brain activity in response to external sensory stimuli and atypical habituating responses between attacks [92][93]. Moreover, other studies directed to pharmacologically-induced and

triggered attacks could reproduce the pathological migraine mechanisms during the ictal phase [9].

In the last two decades, rs-fMRI experiments have increased exponentially, providing new insights regarding the alterations in migraine brain FC throughout the migraine cycle and compared to healthy subjects. Most studies focused on the analysis of FC assuming stationarity over a full rs-fMRI scan, using mainly seed-based correlational analysis and ICA. Table *2.2.* summarises the main sFC alterations observed in the past years, based on the review of Skorobogatykh et al. [94] and the more recent literature published to date.

Migraine literature comparing the interictal phase with healthy controls revealed an abnormal FC in more than 20 RSNs, namely the basal ganglia (BasN) and central executive (CEN) networks, DAN, DMN, ECN, FPN, SMN and SN, and other networks composed by pain processing structures belonging to the so-called "pain matrix", such as the amygdala, cingulate cortex, cerebellum, hypothalamus, insula, PAG, prefrontal cortex, posterior central gyrus and thalamus [93][94]. Furthermore, studies suggested altered FC in the DAN, DMN and executive network (EN) during the ictal phase compared to controls and in the DMN, FPN, SMN, VN, pons network and pain matrix (hypothalamus, insula, postcentral gyrus and thalamus) during the ictal phase compared to the interictal phase.

Although atypical sFC has been reported within migraine brain sensory processing regions involved in affective, cognitive and sensory-discriminative pain processes, the heterogeneity across studies suggests poor reproducibility of results and lack of migraine-specific neuroimaging patterns [94].

More recently, assuming that FC fluctuates on short time scales, other studies started to emerge, exploring the dynamic aspects of rs-fMRI [80]. In Table 2.3., the state-of-the-art of dFC findings regarding migraine is described. Due to the novelty of this approach and lack of studies, literature on headache-related disorders was also included. Alterations in FC were detected in patients with these conditions in the AudN, DMN, FPN, ECN, SMN, SN, VN, subcortical (SCN) and cognitive control (CogCN) networks, and pain matrix (lower brainstem, cingulate cortex, cerebellum, insula, prefrontal cortex and thalamus) in comparison to controls.

Table 2.2. Static FC rs-fMRI studies in migraine.

| RSN | Main FC-related findings |
| --- | --- |
| **BasN** | Interictal *vs.* HC<br>↑**sFC:** R Cd–L Ins/L Pu; L Cd–BLatHCG/L Amg/L Ins/L Pu; NAc–BLatParaHCG/ BLatACC/ BLatOFC/L PCC [102]; R MdNS–R ACC/R MTG/R ITG/L ParaHCG; L MdNS– R PreCeG/ BLatMFG/L HC/R MFG; ↓**sFC:** R MdNS–R Ins; L MdNS–R Ins [103]. |
| **CEN** | Interictal *vs.* HC<br>↑**sFC:** R CEN–R MFG/R AIns; L CEN–L IFG [104]. |
| **DAN** | Interictal *vs.* HC<br>↑**sFC:** L DAN–R OG/L RecG/R FusG/R MTG/R ParaHCG/R MOccG [105]. |
| **DMN** | Interictal *vs.* HC<br>↑**sFC:** DMN (BLatHeschl'sG, BLat Planum Temporale, L STG, BLatLinG, OccFusG, CG) [106]; DMN–R AIns [104]/L PCC/L Precun [107]; ↓**sFC:** DMN–L SPFG/L T pole [108].<br>Ictal *vs.* HC<br>↑**sFC:** DMN (MPFC–PCC/BLatIns) [109].<br>Ictal *vs.* Interictal<br>↑**sFC:** DMN (DMedFC, SFG, MTG); ↓**sFC:** DMN (Precun, VentMedPFC, AnG) [110]. |
| **PonsN** | Ictal *vs.* Interictal<br>↑**sFC:** Pons [110]; L Pons (L S1, L SPar lobule) [111]. |

Table 2.2. *(Continued)*

| RSN | | Main FC-related findings |
|---|---|---|
| ECN | | Interictal *vs.* HC<br>↓**sFC:** R ECN–R MFG/DACC [112].<br>Ictal *vs.* HC<br>↓**sFC:** EN–DAN [65]. |
| FPN | | Interictal *vs.* HC<br>↑**sFC:** FPCEN (L IFG in the L FPCEN, R MFG in the R FPCEN); R FPCEN–A Ins [104];<br>↓**sFC:** FPN–R MFG/R DACC [113]; R FPN–Precun [114]. |
| SMN | | Interictal *vs.* HC<br>↑**sFC:** L S1–L APar lobe/R SPar lobe/R S1/BLatPreMoC/R IFG/R Ins/R T lobe/L Prim MoC/R MOccG; ↓**sFC:** R S1–BLatPreMoC/BLatSFG/BLatACC/Pons/L Ins/BLatS1/ BLat PaCe lobule/R T lobe/R Cb lobule VIIIb/L IPar lobule [115].<br>Ictal *vs.* Interictal<br>↓**sFC:** SMN (SMC) [116]. |
| SN | | Interictal *vs.* HC<br>↓**sFC:** SN–R Supp [104]. |
| VN | | Ictal *vs.* Interictal<br>↑**sFC:** Aura-side V5–Lower MFG [111]. |
| Pain matrix | Amg | Interictal *vs.* HC<br>↑**sFC:** Amg–AIns/S2/Th [117]; L Amg–L MCG/L Precun [118]. |
| | CC | Interictal *vs.* HC<br>↑**sFC:** R ACC–BLatOFC; L ACC–BLatOFC/R DLatPFC [119]/BLatF lobe/L Par lobe [120]; DACC (BLatMT lobe, OFC, L DLatPFC); R Occ lobe (R MCC) [121];<br>↓**sFC:** R ACC–PFC/PCC [122]. |
| | Cb | Interictal *vs.* HC<br>↑**sFC:** R Cb–R MedPFC [121]. |
| | HTh | Interictal *vs.* HC<br>↑**sFC:** HTh–R PreCeG/R MFG/L SParG/SupG/L ITG/R Planum Polare/L T pole/L MTG/L ParaHCG/L STG/BLatHC/L Cd/R NCoer/BLatPontN/L Cb crus I and II/ BLatCb lobule V/R Cb lobules V and VI/L Vermal lobules VIIIa and VIIIb/L DentN; ↓**sFC:** HTh– R PreCeG/L F pole/L ParaCG/R SFG/R FusG/L LinG [123].<br>Ictal *vs.* Interictal<br>↑**sFC:** HTh [110]. |
| | Ins | Interictal *vs.* HC<br>↑**sFC:** R Ins–L T lobe/R F lobe/L Par lobe [120]; **Atypical sFC:** AIns–Pul/MTC/ DMedTh/Precun/PAG/CC/IParC [124].<br>Ictal *vs.* Interictal<br>↑**sFC:** Ins [110]; ↓**sFC:** Ins (PInsC) [116]. |
| | PAG | Interictal *vs.* HC<br>↑**sFC:** PAG–R VentLatPFC/R SupG/R AIns/R PoCeG (S1)/R Th/L AnG/L SupG/ Par Operculum (S2)/BLatPreCeG; ↓**sFC:** PAG–R DLatPFC/R LatPFC/R AC/L DMedPFC/L MedPFC/L AIns [125]; R VentLatPAG–L PreCeG; L VentLatPAG– L PreCeG/L MFG/L IFG/BLatMTG/R SFG/R Supp; DLatPAG–R Pars Triangularis of IFG/MeSFG [126]. |
| | PFC | Interictal *vs.* HC<br>↑**sFC:** L MedPFC (BLatDLat PFC) [121]; R PFC–BLatPar lobe/L T lobe; L PFC– R Precun; BLatPar lobe [104]; R Occ lobe (L DLatPFC) [121]; ↓**sFC:** L PFC–L Ins/PParC [122]. |
| | PCG | Ictal *vs.* Interictal<br>↑**sFC:** L PoCeG [110]. |
| | Th | Interictal *vs.* HC<br>↑**sFC:** R Th–BLatCd/L T lobe/R Pu [104].<br>Ictal *vs.* Interictal<br>↑**sFC:** Th [110]; R Th–L SPar lobule/L InsC/L PrimMoC/L Supp/L OFC; ↓**sFC:** R Th–R S1/R PreMoC [127]. |

Table 2.3. Dynamic FC rs-fMRI studies in migraine and headache-related disorders.

| Citation | Population | Acquisition | Brain parcellation | Analysis | | |
|---|---|---|---|---|---|---|
| | | | | | Methods | Main FC-related findings |
| Wang et al. (2017) [95] | **CH** (21F, 7M): Migraine (13-) PrimH (7-) TTH (8-) **HC** (21F, 7M) | 3.0 T scanner 10-min scan TR = 2000 ms TE = 30 ms Scanning performed w/ eyes closed. | Seed-based analysis: 14 cortical ROIs. | **sFC** | Seed-based analysis w/ Pears. corr. The 6 ROIs with significant ≠ in sFC followed for dFC analysis. | CH vs. HC ↑**sFC**: L MedOFC–L PCC/L ITC/R SParC; L PCC–L SFC/L ITC; R SParC–R CunC. |
| | | | | **dFC** | SW w/ Pears. corr. (WSize = 15/30/60 TR, WStep = 1 TR); WTC w/ Morlet WT; Distr. and std. of corr. coefs. per SW (subj.- and group-level); Freq. spectrum of coefs. w/ FFT and max. ampl. ≠ between groups; Av. of WTC values; Corr. to dFC (group-level). | CH vs. HC ≠**dFC**: L MedOFC–L PCC/L ITC (WSize = 15/60 TR)/L PCC (0.02-0.033 Hz)/L ITC (0.015-0.01 Hz)/R SParC (0.015-0.01 Hz). |
| Tu et al. (2019) [96] | **MO interictal** (67F, 22M) **HC** (52F, 18M) | 3.0 T scanner 6-min scan TR = 2000 ms TE = 30 ms Scanning performed w/ eyes closed. | GICA: 52 ICNs, namely the VN, AudN, CogCN, DMN, SCN (w/ 2 ICNs of Th nuclei), SMN. | **dFC** | SW w/ graphic LASSO (WSize = 20 TR, WStep = 1 TR); k-means clustering on patient-specific exemplars; Graph theory (subj.- and group-level); Clin. corr. determined w/ multivariate linear regression model. | Interictal vs. HC ↑**dFC**: VN–SMN (all states); ↓**dFC**: VN (4 states); VN–SCN/DMN (1 state)/CogCN (3 states). Clin. corr. in MO group **Corr +**: dFC PTh–Precun w/ headache freq.; **Corr -**: dFC PTh–MOccG w/ headache freq. |
| Lee et al. (2019) [81] | **Migraine interictal** (13F, 3M) **Migraine ictal/peri-ictal** (22F, 12M) **HC** (35F, 15M) | 3.0 T scanner TR = 3000 ms TE = 30 ms Scanning performed w/ eyes opened. | GICA for the interictal dataset and HC: 47 ICNs, namely the VN, DMN, ECN, FPN, SMN, AudN, SN, ThN, BasN, CbN, BrN, pain matrix, used for the ictal/peri-ictal dataset. | **sFC** | Graph theory (nodes = ICNs, edges = Pears. corr. (*r*) between time series of ≠ nodes); Fisher's *r*-to-z transf. of FC matrices and EigC values (all groups). | Interictal vs. HC ≠**sFC**: BrN (lower pons-upper medulla). |
| | | | | **dFC** | SW w/ Pears. corr. (WSize = 22 TR, WStep = 1 TR, convolved w/ Gaussian kernel (Size = 3 TR, Stride = 1 TR); L1 reg. of dFC matrices; k-means clustering (subj.- and group-level for the interictal dataset, obtained brain states used in the ictal/peri-ictal dataset); EigC values for migraine groups; Clin. corr. determined w/ EigC values. | Interictal vs. HC ↑**dFC**: BrN (lower brainstem); ↓**dFC**: DMN; FPN; CbN; PModN (ACC, Cb and DMdb). Ictal/peri-ictal vs. HC ↑**dFC**: BrN; ThN; PModN (CeOpCs, Ins, S2); ↓**dFC**: FPN; CbN; PModN (ACC, BLatIns, MedPFC, Precun). Clin. corr in migraine group **Corr +:** dFC Br w/ disease dur.; **Corr -:** dFC Cb w/ disease dur. and headache freq. |

Table 2.3. *(Continued).*

| Citation | Population | Acquisition | Brain parcellation | Analysis | | |
|---|---|---|---|---|---|---|
| | | | | | Methods | Main FC-related findings |
| Dum-krieger et al. (2019) [97] | **Migraine** (21F, 12M) **PPTH** (16F, 28M) **HC** (17F, 19M) | 3.0 T scanner 10-min scanner TR = 2500 ms TE = 27 ms Scanning performed w/ eyes closed | ROI approach: 59 ROIs. | sFC | Seed-based analysis w/ Spear. corr. The ROI pairs w/ scorr. > 0.1 at least for one group were included in the next analyses; Variance analysis w/ *t*-tests (group-level comparison); ROI pairs w/ significant ≠ in sFC followed for clin. corr. determined w/ Pears. corr. corrected for sex and age. | Migraine vs. HC ≠**sFC:** R S1–L SupG; L VentMedPFC–R TPole; L S2–L MOccG/R Cun/L Cun/L ACC; L LinG–LPrecun. Migraine vs. PPTH ≠**sFC:** ACC; MCC; Cun; Precun; HTh; LinG; MOccG; S1; S2; PIns; PulN; SupG; SM; SParLobe; TPole; VentMedPFC; DLatPFC. Clin. corr in migraine group **Corr +:** sFC L S2–R Cun w/ headache freq.; **Corr -:** sFC R DLatPFC–R VentMedPFC w/ years w/ headache. |
| | | | | dFC | SW (WSize = 24 TR); Variance analysis w/ *t*-tests; The ROI pairs w/ significant ≠ in dFC followed for clin. corr determined w/ Pears. corr corrected for sex and age. | Migraine vs. PPTH ≠**dFC**: Amg; HTh; LinG; FusG; MFG; SupG; PreCeG; MCC; PCC; ParOccC; S2; SParG; SM; TPole. Clin. corr in migraine group **Corr +:** dFC R MCC–R SupG w/ headache freq; **Corr -:** dFC R PCC–R Amg w/ pain intensity at the time of testing. |
| Zou et al. (2020) [98] | **CM** (10F, 7M) **HC** (11F, 9M) | 3.0 T scanner TR = 2000 ms TE = 35 ms Scanning performed w/ eyes closed. | GICA: 13 ICNs, namely the DMN, ECN, DAN, AudN, VN and CbN. | sFC | Detrending, despiking and LP filtering (0.01-0.15 Hz) of the selected IC time courses; Pairwise corr. of the ICs; Fisher's *z*-transf. | CM vs. HC ↑**dFC:** ECN (L AnG); AudN (R SParG); ↓**dFC:** AudN (L SFG); VN (R CalSul); DMN (L Precun, L SFG). |
| | | | | dFC | SW (WSize = 30 TR, WStep = 1 TR); k-means clustering; Temporal metrics regarding the states (mean DT, FO and transition changes). | CM vs. HC ↑**dFC:** ECN–DMN/AudN/VN (1 state); ↓**dFC:** DMN–AudN (1 state). |

Table 2.3. *(Continued).*

| Citation | Population | Acquisition | Brain parcellation | Analysis | | |
|---|---|---|---|---|---|---|
| | | | | | Methods | Main FC-related findings |
| Imai et al. (2020) [99] | **Migraine interictal** (62F) Photo-phobia (37F) Phono-phobia (34F) Osmo-phobia (21F) | 3.0 T scanner TR = 2500 ms TE = 40 ms Scanning performed w/ eyes closed. | ROI approach w/ Harvard-Oxford atlas (91 C + 15 SC ROIs) and AAL atlas (26 Cb ROIs). | **sFC** | Seed-based analysis w/ Fisher transf. bivariate corr.; Group-level comparison of ROI-to-ROI corr. | Migraine w/ photophobia vs. without ≠**sFC:** 18 ROI pairs, namely Cb–TOccFusC; Cb hemisphere–TFusC. Migraine w/ phonophobia vs. without ≠**sFC:** 15 ROI pairs, namely Vermis Lobule IX–CunC; Vermis Lobule IX–Amg. Migraine w/ osmophobia vs. without ↑**sFC:** R Cb hemisphere Lobule IV–Br. |
| | | | | **dFC** | dICA; Group-level comparison of ROI-to-ROI corr. | Migraine w/ photophobia, phonophobia and osmophobia vs. without ≠**dFC:** 16 ROI pairs (mainly involving Cb hemisphere), 8 and 14 ROI pairs, respectively. |
| Chen et al. (2021) [100] | **MO** (5F, 16M) **HC** (8F, 13M) | 3.0 T scanner 8.3-min scanner TR = 2000 ms TE = 30 ms Scanning performed with eyes closed. | – | **dFC** | Transf. of the time series into the freq. domain; ALFF at the power within the low-freq. range (0.01-0.8 Hz); SW (WSize = 50 TR, WStep = 5 TR); dALFF; Conversion of dALFF maps into z-scores and statistical analyses; Clin. corr. determined w/ dALFF and VAS values. | MO vs. HC ↓**dALFF:** SN (BLatAIns, BLatACC); BLatOFC; BLatMedPFC; L MFC. ClinCorr in MO group **Corr -:** dALFF ACC w/ VAS scores. |
| Nie et al. (2021) [101] | **Migraine** (15F, 19M) **HC** (20F, 14M) **HC from a public database** (15F, 19M) | 3.0 T scanner 8/7.5/4.3-min scanner TR = 3000/ 2000/2000 ms (respective to each group) | ROI approach w/ Brainnetome atlas (210 C + 36 SC ROIs). | **dFC** | SW w/ Pears. corr. (WSize = 12/18/18 TR respective to each group, WStep = 1 TR); Automatic segm. algorithm to build the WQCP sample set; k-means combined w/ hierarchical clustering to construct the DFCPs; Local network metrics (degree and participation coefficient). | Migraine vs. HC ↑**dFC** regarding one significantly ≠DFCP: Pain matrix (Brodmann areas 1/2/3 (S1), 6 (S2), 10 (APFC), 24 (VentACC), 32 (DACC); InsG; Bas; Th); Pain processing-related areas outside the pain matrix (Brodmann areas 4 (PrimMotorC), 5 (Spar lobule), 7 (Visuomotor coordination)); PParC; MedVOccC). |

**Abbreviations**: **A** = Anterior; **AAL** = Automated Anatomical Labelling; **ALFF** = Amplitude of Low-Frequency Fluctuations; **Ampl**. = Amplitude; **An** = Angular; **Aud** = Auditory; **Av**. = Averaging; **Bas(N)** = Basal Ganglia (Network); **BLat** = Bilateral; **Br(N)** = Brainstem (Network); **C** = Cortex; **CalSul** = Calcarine Sulcus; **Cb(N)** = Cerebellar (Network); **CC** = Cingulate Cortex; **Cd(N)** = Caudate (Nucleus); **CE(N)** = Central Executive (Network); **Ce** = Central; **CG** = Central Gyrus; **CH** = Chronic Headache patients; **Clau** = Claustrum; **Clin** = Clinical; **Corr**. = Correlation; **CM** = Chronic Migraine patients; **Coef(s).** = Coefficient(s); **CogC(N)** = Cognitive Control (Network); **Cun** = Cuneus; **D** = Dorsal; **d** = Dynamic; **DA(N)** = Dorsal Attention (Network); **DentN** = Dentate Nucleus;

Studies following a dFC approach seemed to capture alterations in FC that were not detected with the conventional sFC analysis, being more suitable to study the dynamic nature of brain signals [81]. Nevertheless, despite the relevant findings, the variability of results across the dFC literature shows poor consistency, such as in sFC.

Overall, it is worth noticing that migraine fMRI studies present limitations. Firstly, the usual low number of participants restricts the statistical power of the study and the replication of results in the following investigations [93]. Moreover, the unpredictability of migraine due to the intra- and inter-subject variability in terms of attack duration and associated symptoms makes the ictal studies particularly challenging, together with the fact that these require conjugation of scanner schedules, availability of trained personnel and patient dedication and motivation. Additionally, the administration of preventive medications that may influence brain activity and FC is usually not considered [9].

All these limitations, together with a substantial variety of methods to acquire and analyse fMRI data, hamper the definition of a cohesive and consistent model to represent migraine brain abnormalities at a regional- and network-level [93].

Therefore, optimised fMRI studies are an essential progressive trend in migraine neuroimaging and an indispensable tool to better understand neural migraine dysfunction.

# Chapter 3

# Methods

*This chapter describes clinical data and methods used in the present dissertation. Section 3.1. comprises the description of the cohorts under study and the image acquisition protocol. Section 3.2. provides the reader with an overview of the methods used to preprocess and analyse rs-fMRI data.*

## 3.1. Participants and Image Acquisition

rs-fMRI imaging data used in the present Master Thesis was gathered in the scope of the *MIG_N2Treat* project[1] at Hospital da Luz, with data collected from October 2019. The participants of this project were 8 female patients with menstrual and menstrually-related episodic migraine without aura and 6 healthy controls. Regarding migraineurs, the exclusion criteria were the following: previous history of migraine with aura or chronic migraine; presence of another type of headache, neurological disorder or psychiatric disorder; taking any drugs affecting the central nervous system; being under phophylactic treatment; daily alcohol or tabacco consumption; and non-compatibility with MRI.

All migraine patients underwent the rs-fMRI scan in the interictal phase of the migraine cycle, whereas just 5 of the 8 patients were scanned in the ictal phase. The healthy controls were scanned in the mid-cycle/post-ovulation phase of the menstrual cycle to control for hormonal variation in the interictal phase of the migraine cycle. The ages of the participants ranged between 21 and 45 years old (mean ± standard deviation = 34.1 ± 9.0 years old) for the migraine group and between 22 and 39 years old (27.7 ± 6.0 years old) for the control group.

Within the migraine ictal group, clinical features regarding the ongoing attack were registered and averaged across the 5 patients: attack frequency per month of 3.9 ± 2.0; usual attack duration of (41.6 ± 23.0) hours; mean pain intensity of the attack in a mild (1)-to-severe (3) scale of 2.6 ± 0.5 and in the Visual Analogue Scale (0-10) of (6.2 ± 0.7) hours. Furthermore, regarding the migraine-associated symptoms, migraine patients in the ictal session were interrogated with a yes (1)-or-no (0) question and the answers were averaged across participants: 1.0 for nausea; 0.4 ± 0.5 for vomit; 0.8 ± 0.4 for photo-phobia; 1.0 for phonophobia; and 1.0 for motion sensitivity.

---

[1] ***MIG_N2TREAT Project**: https://welcome.isr.tecnico.ulisboa.pt/projects/multimodal-neuroimaging-biomarkers-throughout-the-migraine-cycle-towards-neurofeedback-training-for-personalized-anti-migraine-treatment/.* Accessed in 15 July 2021 at 2:30 PM.

Regarding the image acquisition, structural and functional data were acquired on a 3 Tesla Siemens Vida MRI system. The structural scans were collected with a $T_1$-weighted magnetization-prepared rapid gradient echo (MPRAGE) series, with TR = 2300 ms, time echo (TE) = 2.98 ms and 1 mm isotropic resolution. The rs-BOLD fMRI scans were acquired for 7 minutes using a $T_2$*-weighted gradient-echo 2D-EPI sequence, with TR = 1260 ms, TE = 30 ms and 2.2 mm isotropic resolution. In the rs-fMRI scans, 333 volumes were acquired, each consisting of 60 axial slices of the whole brain, with an SMS acceleration factor of 3 ($z$ direction) and a generalized autocalibrating partial parallel acquisition (GRAPPA) acceleration factor of 2 ($y$ or phase encoding direction). During the rs-scan, participants were asked to lie with eyes open without falling asleep and with the least possible movement.

In the present work, rs-fMRI data from the Human Connectome Project (HCP)[2] public database were also analysed. Participants included 99 young healthy adults, 54 females and 45 males from 20 to 35 years old. Structural and functional data were collected in a 3 Tesla Siemens Vida MRI system. The structural images were acquired with a $T_1$-weighted MPRAGE series with the following parameters: TR = 2400 ms, TE = 2.14 ms and 0.7 mm isotropic resolution [102]. Functional data were acquired using a $T_2$*-weighted gradient-echo 2D-EPI sequence in four 15-minute sessions (1250 volumes per acquisition), with TR = 720 ms,  TE = 33 ms and 2 mm isotropic resolution. During the session, subjects were asked to keep their eyes open and relax when looking at a white cross on a dark background and with the least possible movement [103].

## 3.2. rs-fMRI Data Processing and Analysis

### 3.2.1. Preprocessing

The rs-fMRI data analysed in this work were preprocessed by the *MIG_N2Treat* project team using the *FMRIB's Software Library® (FSL)*[3] and the *MATLAB 2016b Software® (The Math-Works Inc., Natick, MA, USA)*[4]. The preprocessing steps were the following:

**(i) Brain extraction** using the *Brain Extraction Tool (BET)*[5], which resorts to a stripping algorithm to remove the skull and other non-brain tissues [104].

**(ii) Segmentation and bias field correction** using *FMRIB's Automated Segmentation Tool (FAST)*[6], which is based on a hidden Markov random field model and an associated expectation-maximization algorithm [105]. The concept underlying segmentation is that the signal in each pixel of the image is a weighted contribution between the grey matter (GM), white matter (WM), and cerebrospinal fluid (CSF). Thus, the segmentation algorithm estimates the PVEs in each pixel of the image (fraction of the pixel volume belonging to each tissue type) and divides the brain into GM, WM and CSF. With

---

[2] **HCP**: *https://www.humanconnectome.org/study/hcp-young-adult/data-releases*. Accessed in 15 Sep. 2021 at 19:20 PM.

[3] **FMRIB's Software Library (FSL®):** *https://fsl.fmrib.ox.ac.uk/fsl/fslwiki/*. Accessed in 15 July 2021 at 2:30 PM.

[4] *MATLAB® 2016b Software: https://www.mathworks.com/products/matlab.html*. Accessed in 15 July 2021 at 2:35 PM.

[5] **BET**: *https://fsl.fmrib.ox.ac.uk/fsl/fslwiki/BET*. Accessed in 15 July 2021 at 2:40 PM.

[6] **FAST**: *https://fsl.fmrib.ox.ac.uk/fsl/fslwiki/FAST*. Accessed in 15 July 2021 at 3:00 PM.

the results of segmentation, WM and CSF masks were created and binarized in the structural space. Moreover, the bias field consists of spatial intensity variations (slower signal changes) corresponding to $B_1$ inhomogeneities. Its correction originates a restored bias field-corrected structural image.

**(iii) Motion correction** with the *Motion Correction FMRIB's Linear Registration Tool (MCFLIRT)*[7] due to the movement of the patient's head during the acquisition. The first step is estimating the six motion parameters (three directions of translation and three directions of rotation) for each volume with respect to the middle one, defined as the initial template image (reference). This process works on a mathematical framework of optimising an intensity-based cost function [106]. Then, a rigid body (RB) geometrical transformation is applied based on the motion parameters, and all volumes are aligned to the reference.

**(iv) EPI distortion correction (unwarping) and registration** with the *epi_reg* script[8]. The EPI distortions (geometric distortions and signal loss) arise from $B_0$ inhomogeneities due to magnetic susceptibility differences between tissues within the head (e.g. air/bone and air/tissue interfaces in the sinuses) and are corrected using a field map image. Regarding the registration, it is a two-stage process. The first step is performed with *FLIRT_Boundary-Based Registration (BBR)*[9], suitable for registrations from the EPI to the structural space, which aligns the subject's functional and structural images using a linear RB transformation with six degrees of freedom so that there is consistency in the anatomical areas over time with perfect correspondence between voxels. The second step uses the *FMRIB's Non-Linear Registration Tool (FNIRT)*[10] to perform the registration from the structural to the MNI152 standard space (2 mm), a $T_1$-averaged structural template image created by the Montreal Neurological Institute with 152 structural images, using a non-linear transformation [107]. The WM and CSF masks were also registered into the functional space and eroded with a spherical Gaussian kernel of 2.2 mm and 1.8 mm radius, respectively, to minimize PVEs.

**(v) Semi-automatic classification of ICA components** into the signal of interest, noise or unknown (the latter needs to be manually classified by the operator), with the *FMRIB's ICA-based Xnoiseifier (FIX)*[11], followed by visual inspection. **ICA noise clean-up** to regress the noise components out of the original fMRI data [65][108].

**(vi) Nuisance regression**, in which nuisance time series are regressed out of the data. The nuisance regressors considered were the six RB motion parameters, the motion outliers (time points with abrupt motion, identified with the *FSLMotionOutliers* tool[12]), and average WM and CSF signal, since

---

[7] **MCFLIRT**: *https://fsl.fmrib.ox.ac.uk/fsl/fslwiki/MCFLIRT*. Accessed in 15 July 2021 at 3:20 PM.

[8] **epi_reg**: *https://fsl.fmrib.ox.ac.uk/fsl/fslwiki/FLIRT/UserGuide#epi_reg*. Accessed in 15 July 2021 at 3:25 PM.

[9] **FLIRT_BBR**: *https://fsl.fmrib.ox.ac.uk/fsl/fslwiki/FLIRT_BBR*. Accessed in 15 July 2021 at 3:40 PM.

[10] **FNIRT**: *https://fsl.fmrib.ox.ac.uk/fsl/fslwiki/FNIRT*. Accessed in 15 July 2021 at 3:45 PM.

[11] **FIX**: *https://fsl.fmrib.ox.ac.uk/fsl/fslwiki/FIX*. Accessed in 15 July 2021 at 3:50 PM.

[12] **FSLMotionOutliers**: *https://fsl.fmrib.ox.ac.uk/fsl/fslwiki/FSLMotionOutliers*. Accessed in 15 July 2021 at 4:00 PM.

these likely only reflect physiological noise sources. These regressors enter into a General Linear Model fitted to the data using *FSL*'s tool *FEAT*[13] [109].

**(vii) High-pass filtering** with a cut-off period of 100 s to remove the very low-frequency fluctuations from the data (e.g. instrumentation, scanner drift and RF coil), using the *FSL*'s tool *FEAT*[13] [109].

**(viii) Spatial smoothing (low-pass filtering)** using the *FSL*'s tool *SUSAN*[14], which consists of convolving the BOLD signal with a Gaussian kernel, increasing the SNR and validating the assumptions of the Random Gaussian Field theory, used to correct for multiple comparisons in voxelwise statistical tests. The full width at half maximum of this function, which determines the extent of data smoothing, was set to 3.3 mm (1.5 times the voxel size) [8][110].

The following processing steps were performed using the *MATLAB 2016b software*®, and the LEiDA was applied following Cabral et al.'s pipeline[15] [86].

One should note that the HCP rs-fMRI data followed a minimal preprocessing pipeline to minimize the amount of information removed from the data while ensuring a minimum quality standard [102]. Briefly, these steps included the correction of field map distortions, EPI distortions, eddy-current-induced distortions, gradient-nonlinearities and motion and registration.

## 3.2.2. Parcellation

Since one of the goals of this work was to identify potential similarities and/or discrepancies between the FC results derived from different brain parcellations, four commonly used atlases were evaluated: AAL atlas with 90 cortical and subcortical ROIs[15], hereinafter called the AAL90 [72]; AAL atlas with 116 cortical, subcortical and cerebellar ROIs[16], the AAL116 [72]; Desikan atlas with 66 cortical ROIs[15] [73]; and Harvard-Oxford atlas with 63 cortical and subcortical ROIs[15].

One should note that the Desikan atlas was initially extracted with codification for 70 ROIs, including areas corresponding to the left and right WM and left and right corpus callosum. Hence, only to keep the GM regions for averaging the BOLD signal, the atlas was recoded, yielding the remaining 66 ROIs.

Furthermore, the cortical and subcortical Harvard-Oxford atlases were extracted separately, with 48 and 21 ROIs, respectively. Regarding the subcortical atlas, it was recoded not to consider the regions corresponding to the left and right WM, left and right ventricles and left and right cerebral cortices (that would already be studied with better resolution in the cortical atlas), yielding 15 ROIs. After merging both cortical and subcortical atlases, the final Harvard-Oxford atlas exhibited 63 ROIs.

The labels of the ROIs corresponding to the AAL90, AAL116, Desikan and Harvard-Oxford brain parcellation schemes and their respective brain location – cortical (frontal, parietal, temporal or occipital lobe), subcortical or cerebellar region – are listed in Figure 3.1.

---

[13] ***FEAT****: https://fsl.fmrib.ox.ac.uk/fsl/fslwiki/FEAT. Accessed in 15 July 2021 at 4:00 PM.
[14] ***SUSAN****: https://fsl.fmrib.ox.ac.uk/fsl/fslwiki/SUSAN. Accessed in 15 July 2021 at 4:10 PM.
[15] ***Github Joana Cabral****: https://github.com/juanitacabral/LEiDA. Accessed in 20 Mar. 2021 at 18:00 PM.
[16] ***Neurodata***: https://github.com/neurodata/neuroparc/tree/master/atlases/label/Human. Accessed in 1 Ap. 2021 at 15:00 PM.

## AAL116

1 L Precental Gyrus
2 R Precental Gyrus
3 L Frontal Superior Dorsolateral Gyrus
4 R Frontal Superior Dorsolateral Gyrus
5 L Frontal Middle Gyrus
6 R Frontal Middle Gyrus
7 L Frontal Inferior Triangular Gyrus
8 R Frontal Inferior Triangular Gyrus
9 L Frontal Inferior Opercular Gyrus
10 R Frontal Inferior Opercular Gyrus
11 L Frontal Inferior Orbital Gyrus
12 R Frontal Inferior Orbital Gyrus
13 L Rolandic Operculum
14 R Rolandic Operculum
15 L Supplementary Motor Area
16 R Supplementary Motor Area
17 L Olfactory Cortex
18 R Olfactory Cortex
19 L Frontal Superior Medial Gyrus
20 R Frontal Superior Medial Gyrus
21 L Frontal Superior Medial Orbital Gyrus
22 R Frontal Superior Medial Orbital Gyrus
23 L Gyrus Rectus
24 R Gyrus Rectus
25 L Frontal Superior Orbital Gyrus
26 R Frontal Superior Orbital Gyrus
27 L Frontal Middle Orbital Gyrus
28 R Frontal Middle Orbital Gyrus
29 L Orbitofrontal Posterior Cortex
30 R Orbitofrontal Posterior Cortex
31 L Orbitofrontal Lateral Cortex
32 R Orbitofrontal Lateral Cortex
33 L Insular Cortex
34 R Insular Cortex
35 L Anterior Cingulate Gyrus
36 R Anterior Cingulate Gyrus
37 L Medial Cingulate Gyrus
38 R Medial Cingulate Gyrus
39 L Posterior Cingulate Gyrus
40 R Posterior Cingulate Gyrus
41 L Hippocampus
42 R Hippocampus
43 L Parahippocampal Gyrus
44 R Parahippocampal Gyrus
45 L Amygdala
46 R Amygdala
47 L Calcarine Fissure
48 R Calcarine Fissure
49 L Cuneus Cortex
50 R Cuneus Cortex
51 L Lingual Gyrus
52 R Lingual Gyrus
53 L Occipital Superior Gyrus
54 R Occipital Superior Gyrus
55 L Occipital Middle Gyrus
56 R Occipital Middle Gyrus
57 L Occipital Inferior Gyrus
58 R Occipital Inferior Gyrus
59 L Fusiform Gyrus
60 R Fusiform Gyrus
61 L Postcentral Gyrus
62 R Postcentral Gyrus
63 L Parietal Superior Gyrus
64 R Parietal Superior Gyrus
65 L Parietal Inferior Gyrus
66 R Parietal Inferior Gyrus
67 L Supramarginal Gyrus
68 R Supramarginal Gyrus
69 L Angular Gyrus
70 R Angular Gyrus
71 L Precuneus Cortex
72 R Precuneus Cortex
73 L Paracentral Lobule
74 R Paracentral Lobule
75 L Caudate Nucleus
76 R Caudate Nucleus
77 L Lenticular Nucleus Putamen
78 R Lenticular Nucleus Putamen
79 L Lenticular Nucleus Pallidum
80 R Lenticular Nucleus Pallidum
81 L Thalamus
82 R Thalamus
83 L Heschl Gyrus
84 R Heschl Gyrus
85 L Temporal Superior Gyrus
86 R Temporal Superior Gyrus
87 L Temporal Pole Superior
88 R Temporal Pole Superior
89 L Temporal Middle Gyrus
90 R Temporal Middle Gyrus
91 L Temporal Pole Middle
92 R Temporal Pole Middle
93 L Temporal Inferior Gyrus
94 R Temporal Inferior Gyrus
95 L Cerebellum Crus1
96 R Cerebellum Crus1
97 L Cerebellum Crus2
98 R Cerebellum Crus2
99 L Cerebellum 3
100 R Cerebellum 3
101 L Cerebellum 4,5
102 R Cerebellum 4,5
103 L Cerebellum 6
104 R Cerebellum 6
105 L Cerebellum 7b
106 R Cerebellum 7b
107 L Cerebellum 8
108 R Cerebellum 8
109 L Cerebellum 9
110 R Cerebellum 9
111 L Cerebellum 10
112 R Cerebellum 10
113 Vermis 1,2
114 Vermis 4
115 Vermis 4,5
116 Vermis 6

## AAL90

1 L Precental Gyrus
2 R Precental Gyrus
3 L Frontal Superior Gyrus
4 R Frontal Superior Gyrus
5 L Frontal Superior Orbital Gyrus
6 R Frontal Superior Orbital Gyrus
7 L Frontal Middle Gyrus
8 R Frontal Middle Gyrus
9 L Frontal Middle Orbital Gyrus
10 R Frontal Middle Orbital Gyrus
11 L Frontal Inferior Opercular Gyrus
12 R Frontal Inferior Opercular Gyrus
13 L Frontal Inferior Triangular Gyrus
14 R Frontal Inferior Triangular Gyrus
15 L Frontal Inferior Orbital Gyrus
16 R Frontal Inferior Orbital Gyrus
17 L Rolandic Operculum
18 R Rolandic Operculum
19 L Supplementary Motor Area
20 R Supplementary Motor Area
21 L Olfactory Cortex
22 R Olfactory Cortex
23 L Frontal Superior Medial Gyrus
24 R Frontal Superior Medial Gyrus
25 L Frontal Medial Orbital Cortex
26 R Frontal Medial Orbital Cortex
27 L Gyrus Rectus
28 R Gyrus Rectus
29 L Insular Cortex
30 R Insular Cortex
31 L Anterior Cingulate Cortex
32 R Anterior Cingulate Cortex
33 L Middle Cingulate Cortex
34 R Middle Cingulate Cortex
35 L Posterior Cingulate Cortex
36 R Posterior Cingulate Cortex
37 L Hippocampus
38 R Hippocampus
39 L Parahippocampal Gyrus
40 R Parahippocampal Gyrus
41 L Amygdala
42 R Amygdala
43 L Calcarine Fissure
44 R Calcarine Fissure
45 L Cuneus Cortex
46 R Cuneus Cortex
47 L Lingual Gyrus
48 R Lingual Gyrus
49 L Occipital Superior Gyrus
50 R Occipital Superior Gyrus
51 L Occipital Middle Gyrus
52 R Occipital Middle Gyrus
53 L Occipital Inferior Gyrus
54 R Occipital Inferior Gyrus
55 L Fusiform Gyrus
56 R Fusiform Gyrus
57 L Postcentral Gyrus
58 R Postcentral Gyrus
59 L Parietal Superior Gyrus
60 R Parietal Superior Gyrus
61 L Parietal Inferior Gyrus
62 R Parietal Inferior Gyrus
63 L Supramarginal Gyrus
64 R Supramarginal Gyrus
65 L Angular Gyrus
66 R Angular Gyrus
67 L Precuneus Cortex
68 R Precuneus Cortex
69 L Paracentral Lobule
70 R Paracentral Lobule
71 L Caudate Nucleus
72 R Caudate Nucleus
73 L Lenticular Nucleus Putamen
74 R Lenticular Nucleus Putamen
75 L Lenticular Nucleus Pallidum
76 R Lenticular Nucleus Pallidum
77 L Thalamus
78 R Thalamus
79 L Heschl Gyrus
80 R Heschl Gyrus
81 L Temporal Superior Gyrus
82 R Temporal Superior Gyrus
83 L Temporal Pole Superior
84 R Temporal Pole Superior
85 L Temporal Middle Gyrus
86 R Temporal Middle Gyrus
87 L Temporal Pole Middle
88 R Temporal Pole Middle
89 L Temporal Inferior Gyrus
90 R Temporal Inferior Gyrus

## Desikan

1 L Precentral Gyrus
2 R Precentral Gyrus
3 L Frontal Superior Gyrus
4 R Frontal Superior Gyrus
5 L Frontal Middle Gyrus
6 R Frontal Middle Gyrus
7 L Frontal Middle Rostral Gyrus
8 R Frontal Middle Rostral Gyrus
9 L Frontal Inferior Opercular Gyrus
10 R Frontal Inferior Opercular Gyrus
11 L Frontal Inferior Triangular Gyrus
12 R Frontal Inferior Triangular Gyrus
13 L Frontal Inferior Orbital Gyrus
14 R Frontal Inferior Orbital Gyrus
15 L Orbitofrontal Lateral Cortex
16 R Orbitofrontal Lateral Cortex
17 L Orbitofrontal Medial Cortex
18 R Orbitofrontal Medial Cortex
19 L Frontal Pole
20 R Frontal Pole
21 L Anterior Cingulate Cortex Caudal
22 R Anterior Cingulate Cortex Caudal
23 L Anterior Cingulate Cortex Rostral
24 R Anterior Cingulate Cortex Rostral
25 L Posterior Cingulate Cortex
26 R Posterior Cingulate Cortex
27 L Parahippocampal Gyrus
28 R Parahippocampal Gyrus
29 L Cingulate Isthmus
30 R Cingulate Isthmus
31 L Cuneus Cortex
32 R Cuneus Cortex
33 L Lingual Gyrus
34 R Lingual Gyrus
35 L Occipital Lateral Cortex
36 R Occipital Lateral Cortex
37 L Fusiform Gyrus
38 R Fusiform Gyrus
39 L Postcentral Gyrus
40 R Postcentral Gyrus
41 L Parietal Superior Gyrus
42 R Parietal Superior Gyrus
43 L Parietal Inferior Gyrus
44 R Parietal Inferior Gyrus
45 L Supramarginal Gyrus
46 R Supramarginal Gyrus
47 L Pericalcarine Cortex
48 R Pericalcarine Cortex
49 L Precuneus Cortex
50 R Precuneus Cortex
51 L Paracentral Gyrus
52 R Paracentral Gyrus
53 L Temporal Superior Gyrus
54 R Temporal Superior Gyrus
55 L Temporal Middle Gyrus
56 R Temporal Middle Gyrus
57 L Temporal Inferior Gyrus
58 R Temporal Inferior Gyrus
59 L Banks Superior Temporal Sulcus
60 R Banks Superior Temporal Sulcus
61 L Entorhinal Cortex
62 R Entorhinal Cortex
63 L Temporal Pole
64 R Temporal Pole
65 L Temporal Transverse Cortex
66 R Temporal Transverse Cortex

## Harvard-Oxford

1 Frontal Superior Gyrus
2 Frontal Middle Gyrus
3 Frontal Inferior Opercular Gyrus
4 Frontal Inferior Triangular Gyrus
5 Frontal Medial Cortex
6 Supplementary Motor Area
7 Subcallosal Cortex
8 Subcallosal Cortex
9 Paracingulate Gyrus
10 Orbitofrontal Cortex
11 Frontal Opercular Cortex
12 Central Opercular Cortex
13 Anterior Cingulate Gyrus
14 Posterior Cingulate Gyrus
15 Frontal Pole
16 Insular Cortex
17 L Hippocampus
18 R Hippocampus
19 Parahippocampal Anterior Gyrus
20 Parahippocampal Posterior Gyrus
21 L Amygdala
22 R Amygdala
23 Intracalcarine Cortex
24 Cuneus Cortex
25 Lingual Gyrus
26 Supracalcarine Cortex
27 Occipital Superior Lateral Cortex
28 Occipital Inferior Lateral Cortex
29 Occipital Pole
30 Fusiform Gyrus
31 Postcentral Gyrus
32 Parietal Superior Lobule
33 Supramarginal Anterior Gyrus
34 Supramarginal Posterior Gyrus
35 Angular Gyrus
36 Precuneus Cortex
37 Parietal Opercular Cortex
38 Heschl Gyrus
39 Temporal Pole
40 Temporal Superior Anterior Gyrus
41 Temporal Superior Posterior Gyrus
42 Temporal Middle Anterior Gyrus
43 Temporal Middle Posterior Gyrus
44 Temporal Middle Temporooccipital Gyrus
45 Temporal Inferior Anterior Gyrus
46 Temporal Inferior Posterior Gyrus
47 Temporal Inferior Temporooccipital Gyrus
48 Planum Polare
49 Temporal Fusiform Anterior Cortex
50 Temporal Fusiform Posterior Cortex
51 Temporal Occipital Fusiform Cortex
52 Planum Temporale
53 L Thalamus
54 R Thalamus
55 L Caudate Nucleus
56 R Caudate Nucleus
57 L Putamen
58 R Putamen
59 L Pallidum
60 R Pallidum
61 L Nucleus Accumbens
62 R Nucleus Accumbens
63 Brain-Stem

**Legend:**
- Frontal
- Parietal
- Temporal
- Occipital
- Subcortical
- Cerebellar

Figure 3.1. Labels of the ROIs belonging to the AAL90, AAL116, Desikan and Harvard-Oxford brain parcellation schemes, characterised by their brain spatial location with the color on the right – cortical (frontal, parietal, temporal or occipital lobe), subcortical or cerebellar region.

### 3.2.3. dFC Estimation

The estimation of the dFC was performed using two different approaches: the SW and the PC.

The first step for both methods consisted of filtering the preprocessed ROI-averaged BOLD signal in the low-frequency range of 0.01-0.1 Hz using a second-order Butterworth band-pass filter (Figure 3.2.A). This filter focuses on the most meaningful frequencies of resting-state fluctuations by discarding the signal coming from non-neuronal causes, such as slow drifts (< 0.01 Hz) and high frequencies associated with cardiac and respiratory signals (> 0.1 Hz) [56][75].

#### 3.2.3.1. SW Method

To implement the SW analysis (described in section 2.2.2.4. **(i)**) it was necessary to choose the window size and step. According to the literature, window sizes in the range of 30 s to 60 s are a reasonable choice to capture dFC patterns, and steps of 1 TR are commonly used [96]. Thus, three windows with different sizes were studied – 25 TR (corresponding to 31.5 s), 35 TR (44.1 s) and 45 TR (56.7 s) – to evaluate the whole range used in previous studies, slid in steps of 1 TR (1.26 s). Afterwards, the pairwise Pearson correlation coefficient was computed within each window for all pairs of filtered ROI-averaged BOLD time courses (Equation (2.1)), yielding an *N x N* symmetric dFC matrix per window (time) and subject, in which *N* stands for the number of brain regions of the atlas.

#### 3.2.3.2. PC Method

The PC analysis was performed resorting to the Hilbert transform approach (in section 2.2.2.4. **(ii)**). The filtered ROI-averaged BOLD signals were Hilbert transformed and converted into its complex analytic version, from which it was extracted the instantaneous phase of each region over time (Figure 3.2.B). Finally, the dFC was obtained by computing the phase synchronisation for all pairs of ROIs (Equation (2.6)), originating an *N x N* symmetric dFC matrix per TR and subject, capturing the BOLD phase synchronisation through the whole brain over time. This matrix is illustrated in Figure 3.2.C, with the colours ranging from red (full synchrony of BOLD phases) to blue (phase difference of 180°).

#### 3.2.3.3. Comparison of dFC Matrices Between SW and PC Methods

In order to evaluate the degree of similarity between the dFC matrices obtained with both methods, the cosine similarity coefficient was used. The literature suggests that this metric provides better results than the Pearson correlation [86]. Thus, the dFC matrices obtained per TR with the PC (higher temporal resolution) were averaged within each window used in the SW approach. Then, the cosine similarity coefficient ($CS_{SW,PC}$) was computed between the *Nx(N-1)/2* upper triangular elements (concatenated into a vector) of the dFC matrices obtained with the SW ($x_{SW}$) and the averaged ones obtained with the PC ($x_{PC}$). The expression is described in Equation (3.1):

$$CS_{SW,PC} = \frac{x_{SW} \cdot x_{PC}}{\|x_{SW}\| \|x_{PC}\|} \tag{3.1}$$

where $\| \ \|$ is the Euclidean norm. The cosine similarity is equal to 1 for maximal similarity and -1 for maximal dissimilarity.

### 3.2.4. dFC States

#### 3.2.4.1. LEiDA

After estimating the connectivity time courses, the LEiDA was implemented following Cabral et al.'s pipeline [86] to reduce the dimensionality of the data and improve clustering performance (consult section 2.2.2.5. for more detail). This method was implemented into the dFC matrices yielded by PC and SW since the leading eigenvectors were able to explain the majority of the dFC variance in both metrics.

Regarding the PC method, which characterises each brain region by the respective instantaneous phase, $V_1$ describes the main orientation of BOLD signal phases across the $N$ brain regions over time, and each element of $V_1$ represents the projection of the BOLD phase of the given brain region into this leading eigenvector (Figure 3.2.D). If all elements of $V_1$ have the same sign, then all BOLD phases are pointing in the same direction and following the main orientation determined by $V_1$ (strong coherence), also called the global mode of BOLD signal fluctuation. Instead, if BOLD signals have different orientations with respect to $V_1$ (positive and negative signs), the brain can be divided into two communities according to the BOLD phase relationships between the brain regions. The magnitude of each element of $V_1$ represents the strength with which brain regions belong to those communities [89]. The present work used the convention that the global mode is characterized by positive values of $V_1$ across all brain regions, so detachments from the global mode are represented by negative values.

#### 3.2.4.2. Estimation and Characterisation

In order to identify recurrent FC patterns, the k-means clustering algorithm was implemented at a group-level in the migraine interictal dataset (8 subjects, total of 8 samples); in a group composed of the interictal and ictal dataset (5 subjects in the interictal and ictal phases of the migraine cycle, total of 10 samples); and, finally, in a group including the interictal and healthy controls dataset (6 subjects in the interictal phase of the migraine cycle and 6 healthy controls, total of 12 samples).

This factorisation technique received as input the leading eigenvectors estimated from the dFC matrices concatenated over time and subjects (Figure 3.2.E) and was run with $k$ ranging from 3 to 15 (i.e., dividing the total number of leading eigenvectors into 3 to 15 clusters) to cover the range of functional networks that is commonly found in the literature [89][111]. Moreover, the cosine distance was chosen as the distance metric for minimization since it gave more meaningful results than the squared euclidean distance (higher specificity in detecting well-established RSNs). To increase the likelihood of escaping local minima and ensure consistency in the results, the k-means clustering algorithm was run 1000 times, and the best result that minimized the distance between the cluster point and its centroid was selected.

After implementing this method, the leading eigenvectors were reorganised into a predefined $k$ number of clusters or dFC states representing recurrent patterns of BOLD phase coherence. Each FC pattern was described through its $Nx1$ cluster centroid vector $V_c$ ($c = 1, \ldots, k$) (leading eigenvector of the dFC state) in three different ways (Figure 3.2.F **(i)**, **(ii)** and **(iv)**), and through its $NxN$ dFC matrix, corresponding to the average of the dFC matrix over the time points in which the respective state occurred (Figure 3.2.F **(iii)**) [86][89].
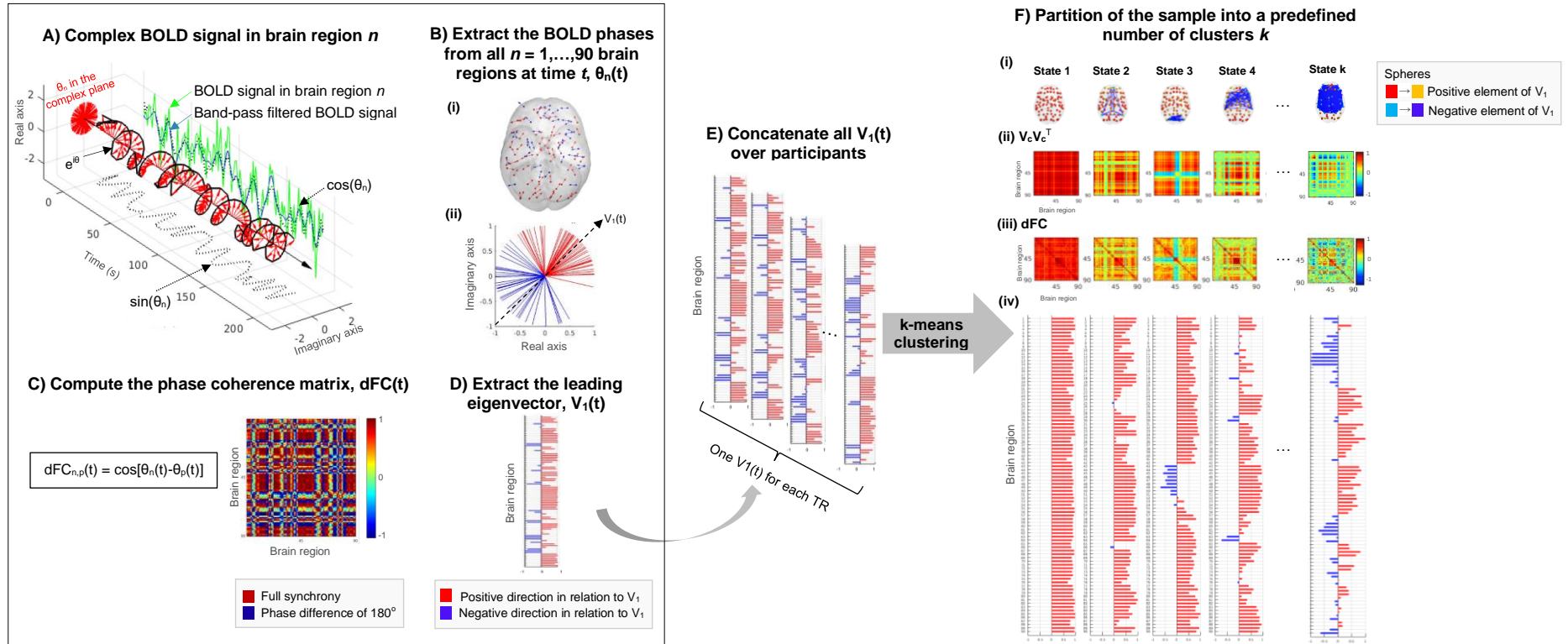
Figure 3.2. Pipeline for the identification of recurrent dFC patterns using LEiDA, with the AAL90 atlas chosen as the brain parcellation scheme and the PC selected as the method to compute the dFC. **A)** The BOLD signal in a given brain region *n* (green) is band-pass filtered between 0.01 and 0.1 Hz (blue) and Hilbert transformed into a complex analytic signal. The signal phase is represented by $e^{i\theta}$ over time *t* (black line) and at each TR (red arrows), where the real part is given by *cos($\theta_n$)* and the imaginary part by *sin($\theta_n$)*. **B)** The BOLD phases of all *N* = 90 brain regions at *t*, $\theta_n(t)$, are represented in **(i)** cortical space, with arrows centered at the center of gravity of each ROI and **(ii)** in the complex plane, with phases centered in the origin of a unit circle with real and imaginary axis. **C)** The PC matrix (dFC(t)) captures the BOLD phase synchronisation between all pairs of regions over *t*. **D)** The leading eigenvector of the dFC matrix ($V_1(t)$) represents the main orientation of all BOLD phases over *t* with respect to $V_1$ (black dashed arrow in B). **E)** The eigenvectors estimated from the dFC matrices are concatenated over time and across subjects and partitioned into a predefined number of clusters or dFC states (*k*), which describe recurrent patterns of BOLD phase coherence, using the k-means clustering algorithm. **F)** dFC states are displayed according to their decreasing probability of occurrence and represented by the respective $V_c$: **(i)** as a network in the AAL90 cortical space (axial slice), in which the elements of $V_c$ are placed at the center of gravity of the respective brain region, shaped as spheres colored according to their sign (red to yellow spheres represent positive elements from 1 to 0, cyan to dark blue represent negative elements from 0 to -1), and areas with $V_c \leq 0.1$ are linked with blue edges; **(ii)** by the outer product $V_cV_c^T$, that represents a N×N connectivity pattern where each $V_c(n)$ weights the contribution of each brain region n to that pattern; and **(iv)** as a bar plot displaying the projection of the BOLD phase in each brain region into $V_c$. dFC states are also characterised by their **(iii)** dFC matrix.

In Figure 3.2.F **(i)**, the cluster centroid vector is represented as a network in the atlas cortical space. Each element of $V_c$ is represented as a sphere placed at the centre of gravity of the respective brain region and coloured according to the respective value of the element of $V_c$ (yellow-to-red spheres represented regions with positive values of $V_c$ following the global mode, and blue-to-cyan spheres represent regions with negative values of $V_c$ detaching from the global mode). To distinguish the network created by the smallest community of brain regions and facilitate the interpretation of the dFC states, areas with elements of $V_c$ equal or inferior to 0.1 were linked with blue edges. Several thresholds for the links were tested, though, this value allowed for better specificity in the network detection. Furthermore, Figure 3.2.F **(ii)** represents the cluster centroid vectors of the dFC states back into matrix format through the outer product of $V_c$ with $V_c^T$. This results in an *NxN* connectivity pattern with rank 1 (since the matrix is obtained from a single vector), with each element weighting the contribution of each brain region to that pattern. Positive red values are set to pairs of brain regions with the same sign of $V_c$ (coherent BOLD signals) and negative blue values to pair of areas with different signs of $V_c$. Finally, Figure 3.2.F **(iv)** displays $V_c$ as a bar plot, showing the projection of the BOLD phase of each brain region into $V_c$.

After estimating the dFC states, they were characterised in terms of their temporal metrics (mean lifetime, probability of occurrence and switching profile), as described in section 2.2.2.5.

### 3.2.4.3. dFC Labels: Temporal Smoothing Algorithm

After k-means clustering, a temporal smoothing algorithm adapted from Pascual-Marqui and colleagues [112][113] was applied to the dFC labels of the states. This algorithm guarantees that the detected FC patterns do not switch faster than the highest frequency of the BOLD signal (0.1 Hz) by ensuring that the assignment of the dFC labels to the leading eigenvectors is not based only on the distance between the leading eigenvector ($x_s$) and cluster centroid ($c_k$) but also on the dFC labels of the neighbouring leading eigenvectors. Thus, the temporal filter minimizes the distance function in Equation (3.2), in which the first term corresponds to the cosine distance (1 - cosine similarity [114]) between the leading eigenvector and cluster centroid and the second one to the temporal smoothing.

$$d_{ks}^2 = \left(1 - \frac{x_s \cdot c_k}{\|x_s\| \|c_k\|}\right) - \lambda b_{ks} \tag{3.2}$$

The *k* corresponds to the dFC label of the cluster, *s* is the sample, $\lambda$ represents the weight of temporal smoothing and $b_{ks}$ is the number of time points with the corresponding dFC label in a window surrounding the given sample. The parameter $\lambda$ was set to 0.5 (intermediate degree of smoothing) after testing it with the values 0.3, 0.5 and 0.8, and the window size chosen was 10 s, which corresponds to the highest frequency of the BOLD signal. The effect of the temporal smoothing implemented on the dFC labels for the partition model *k* = 5 and a single subject, with one colour representing each cluster, is displayed in Figure 3.3.
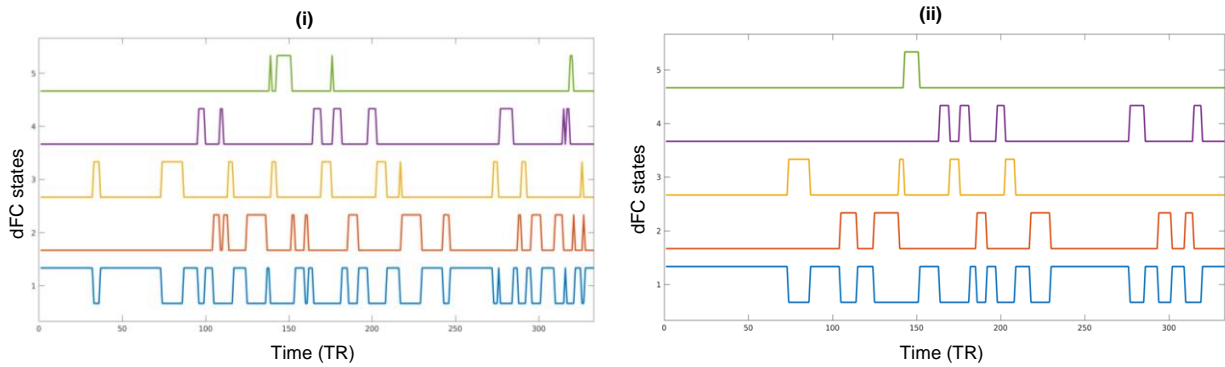
Figure 3.3. Cluster time course **(i)** before and **(ii)** after the implementation of the temporal smoothing algorithm to the dFC labels of a single subject obtained for a k-means clustering algorithm ran with 5 clusters (one colour for each cluster), for the AAL90 as the brain parcellation scheme and PC as the method to compute dFC.

### 3.2.5. Statistical Analysis

#### 3.2.5.1. Correlation of dFC States with RSNs

While RSNs consist of temporal patterns that replicate across space, dFC states represent spatial patterns that replicate over time [86]. Nevertheless, the latter are expected to reveal sub-parts of specific RSNs, combinations of different RSNs or even resemble entire RSNs.

In order to assess the correspondence of the obtained dFC states with well-established RSNs reported in the literature, the correlation of the cluster centroid vectors with the vectors corresponding to the RSNs in atlases spaces was computed, following the method used by Cabral and colleagues [86] [111][115].

Firstly, the seven Yeo RSNs defined in 2 mm$^3$ MNI space by Yeo and colleagues [61] were transformed into the atlas (AAL90, AAL116, Desikan and Harvard-Oxford) space. This process yielded a matrix with size $N$ ROIs × 7 RSNs, i.e., seven vectors with as many elements as the number of ROIs of the given atlas, where each element corresponds to the number of voxels in each brain area belonging to the corresponding Yeo network. Since the network contrasting from the global mode in each state is represented by elements with a negative sign in the respective element of $V_c$, the RSNs vectors were transformed to their symmetric, so that they could be compared to the $V_c$'s. This transformation is depicted in Figure 3.4. for the AAL90 atlas and Figure A.1. of Appendix A for the remaining parcellation schemes. Moreover, since the global mode does not define a functional network of BOLD signal decoupling, the correlation with RSNs was not computed for this state.

This sequence of steps was also applied to the ten RSNs defined by Smith and colleagues in 2 mm$^3$ MNI space [62], and the results are shown in Figure A.2. of Appendix A.

After this transformation, the Pearson correlation coefficient was computed between the cluster centroid vectors of the dFC states corresponding to the partition model being studied and the transformed RSNs vectors. For all partition models studied with the k-means clustering, $k$ hypotheses were tested for each FC repertoire. Therefore, to correct for multiple comparisons, the standard significance threshold 0.05 was adjusted with a Bonferroni correction to 0.05/$k$, and the statistically significant correlations were those with the respective $p$-values inferior to that threshold [89].
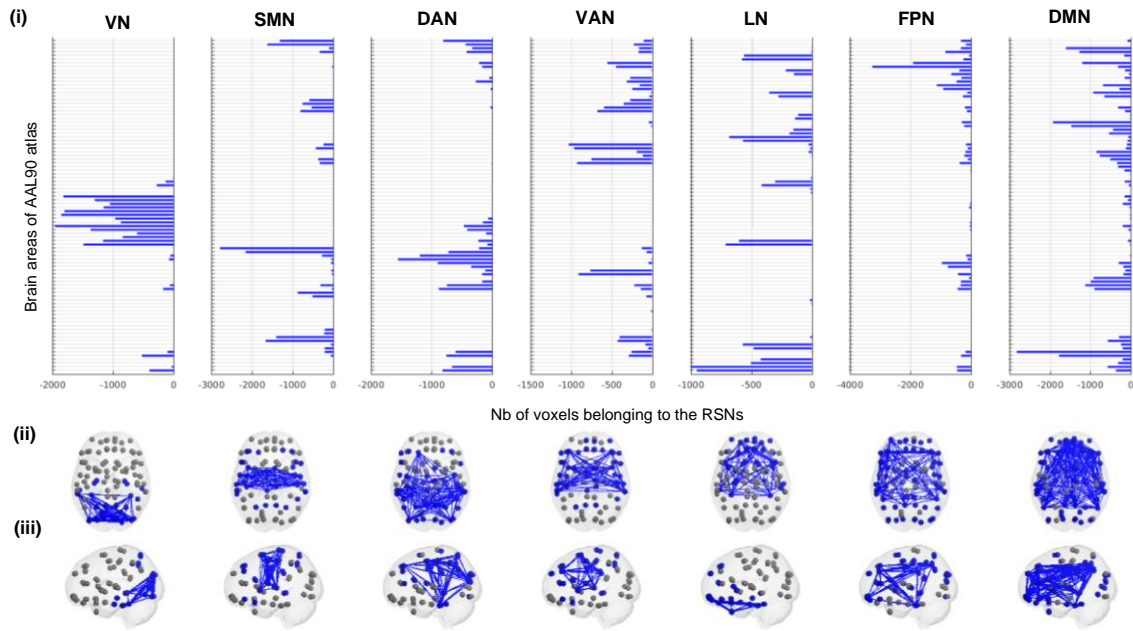
Figure 3.4. Yeo repertoire transformed into the AAL90 atlas space and represented through RSN vectors by **(i)** the distribution of the number of 2 mm$^3$ MNI voxels in each AAL90 brain area belonging to the corresponding RSN, obtaining a vector with N = 90 elements that can be correlated with the cluster centroid vectors of the dFC states and the functional network that detach from the global mode of BOLD signal fluctuation represented in the AAL90 atlas cortical space (**(ii)** axial and **(iii)** sagittal slices). The brain areas contributing to each RSN are displayed with dark blue color and those without any voxel belonging to the RSN are displayed with grey color. The brain areas with more than 400 MNI voxels contributing to the RSN are linked with blue edges. VN = Visual Network; SMN = Somatomotor Network; DAN = Dorsal Attention Network; VAN = Ventral Attention Network; LN = Limbic Network; FPN = Frontoparietal Network; DMN = Default Mode Network.

### 3.2.5.2. Comparison Between Groups

In order to statistically assess between-group significant differences in terms of the temporal metrics (mean lifetime and probability of occurrence) of the obtained dFC states, non-parametric permutation-based *t*-tests with 10,000 permutations were implemented on these two metrics. This non-parametric two-sample hypothesis test resorts to permutations of group labels to build an empirical estimate of the null distribution, which is determined independently for each population instead of relying on the test-type standard distribution [111][116]. In the results obtained with the group composed of the migraine patients in the interictal and ictal sessions, a permutation-based paired *t*-test was implemented, since it compared paired observations of the same subject in two different conditions. Instead, in the results obtained with the group including the migraine patients scanned in the interictal phase and healthy controls, a permutation-based unpaired *t*-test was applied, since it compared two unrelated and independent groups [116]. Afterwards, the results were analysed by plotting the *p*-values for the whole FC repertoire over the range of *k*s. The significance of the results was evaluated using as reference three thresholds for the *p*-values: the standard significance threshold, 0.05; the Bonferroni corrected significance threshold, $0.05/k$, to correct for multiple comparisons by considering the number of states (independent hypotheses) compared within each partition model; and the corrected significance threshold, $0.05/\Sigma k$, to correct for multiple comparisons by considering all hypothesis independent across models, including the whole sample of tests performed [89].

# Chapter 4

# Results and Discussion

*This chapter provides the reader with the results of the present work and their discussion. Firstly, section 4.1. compares the connectivity information obtained with the PC and SW methods. Secondly, section 4.2. shows the results of the proportion of variance explained by the leading eigenvectors in PC and SW methods. Then, section 4.3. comprises an exploratory analysis of the migraine interictal dataset with the AAL90 atlas, and section 4.4. displays the results obtained with the same dataset across different atlases. Finally, section 4.5. provides the statistical analyses and comparisons between groups.*

## 4.1. Comparison between dFC matrices: SW vs. PC methods

In order to compare the dFC matrices estimated for the AAL90, AAL116, Desikan and Harvard-Oxford atlases with the SW and PC methods in the interictal dataset, the cosine similarity was computed between the dFC matrices obtained with the SW and the averaged ones obtained with PC within the respective window (sizes of 25 TR, 35 TR and 45 TR and step of 1 TR), as described in section 3.2.3.3. The results are depicted in Figure 4.1.
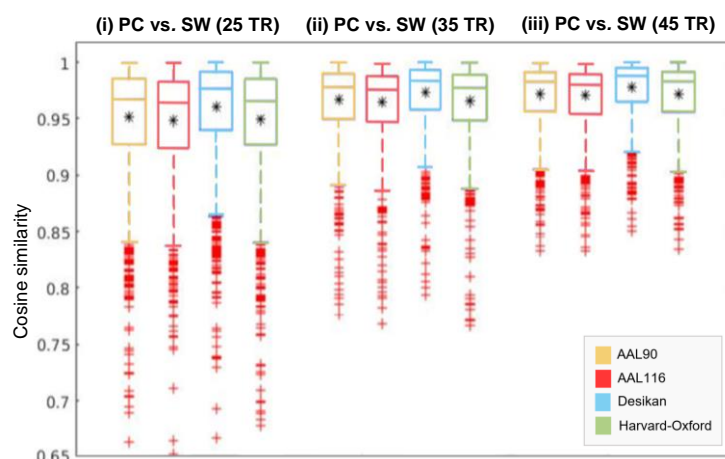


Figure 4.1. Cosine similarity values computed between the dFC matrices obtained with the SW and the averaged ones obtained with PC within the respective window (size of **(i)** 25 TR, **(ii)** 35 TR, and **(iii)** 45 TR, all slid in steps of 1 TR), for the AAL90, AAL116, Desikan and Harvard-Oxford atlases in the interictal group. The median is represented by the horizontal line within the box plot, the mean value is denoted with a black asterisk (∗) and the outliers are marked with the red plus (+).

By looking at the box plots, it is possible to observe that, regardless of the brain parcellation scheme and the window size chosen for the SW, the cosine similarity values are always above 0.650, the medians above 0.960 and the means above 0.940. Furthermore, it was found that the distribution of data points tends to narrow for larger window sizes (fewer outliers with lower cosine similarity values), resulting in a slight increase in the medians and means. This observation might be associated with the fact that larger window sizes lead to the inclusion of more data points in the average of the PC dFC matrices within the window and, consequently, to the increase of the SNR, which would explain a slightly higher similarity between the dFC matrices obtained with the PC and SW with a size of 45 TR.

Thus, despite the methodological differences between the SW and PC, these results suggest that the connectivity information they provide is overall similar.

## 4.2. Variance explained by the leading eigenvector

After estimating the connectivity patterns using SW and PC methods, the LEiDA approach was applied [86]. To confirm the prior assumption that the reduced dimensionality of the leading eigenvector could still explain the majority of dFC data, the proportion of variance explained by this vector was computed for each TR and all subjects by dividing the leading eigenvalue by the sum of all eigenvalues. The results are shown in Figure 4.2.
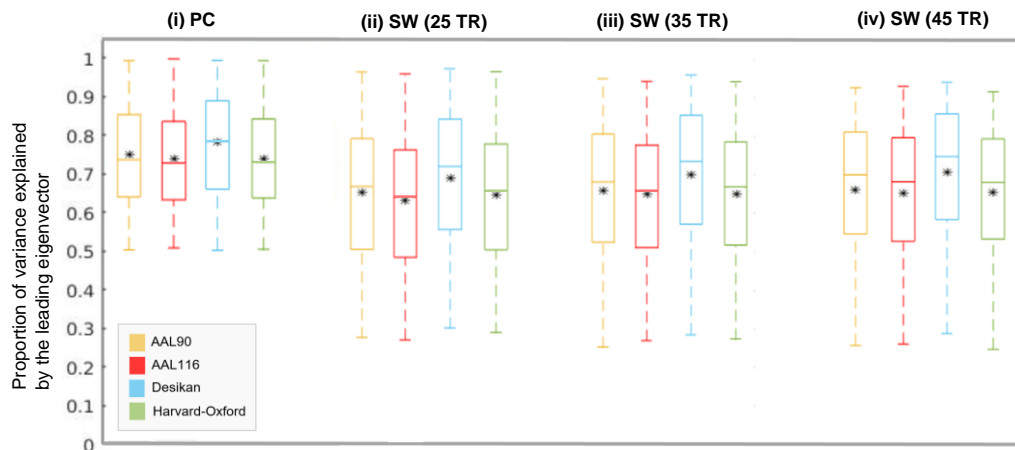


Figure 4.2. Proportion of variance explained by the leading eigenvector for all subjects and the AAL90, AAL116, Desikan and Harvard-Oxford atlases, obtained from the dFC matrices computed with the **(i)** PC and SW of **(ii)** 25 TR, **(iii)** 35 TR and **(iv)** 45 TR, slid in steps of 1 TR. The median is represented by the horizontal line within the boxes and the mean value is denoted with a black asterisk (*).

For the PC method, the percentage of variance explained by the leading eigenvector is above 50 % for all data points across the brain parcellation schemes (by definition), and the median and mean values are above 70 %. This observation is consistent with the findings reported by Cabral et al. [86][111][115] and results from the fact that in this case only two eigenvalues exist and, consequently, the leading eigenvalue represents more than half of the total sum of the eigenvalues. Instead, for the SW method, although the leading eigenvector explains less than 50 % of the total variance in some data points, the mean and median values are still above 60 % for the three sliding windows. Therefore, the leading eigenvector was considered an appropriate method to represent the dFC matrices computed by both PC and SW methods.

## 4.3. Analysis of migraine interictal dataset: AAL90 atlas

After extracting the leading eigenvectors of the dFC matrices estimated with both PC and SW methods, the k-means clustering algorithm was implemented in the interictal group with the predefined number of clusters ranging from $k = 3$ to $k = 15$, in order to assess changes in the dFC repertoire. The recurrent FC states obtained with the AAL90 atlas and PC method are displayed in Figure 4.3., according to their decreasing probability of occurrence within each $k$. This atlas was chosen as the brain parcellation scheme of reference as it is the most commonly used in literature [83][86][111].

The results obtained with the remaining atlases are depicted in Figure B.1. of Appendix B.
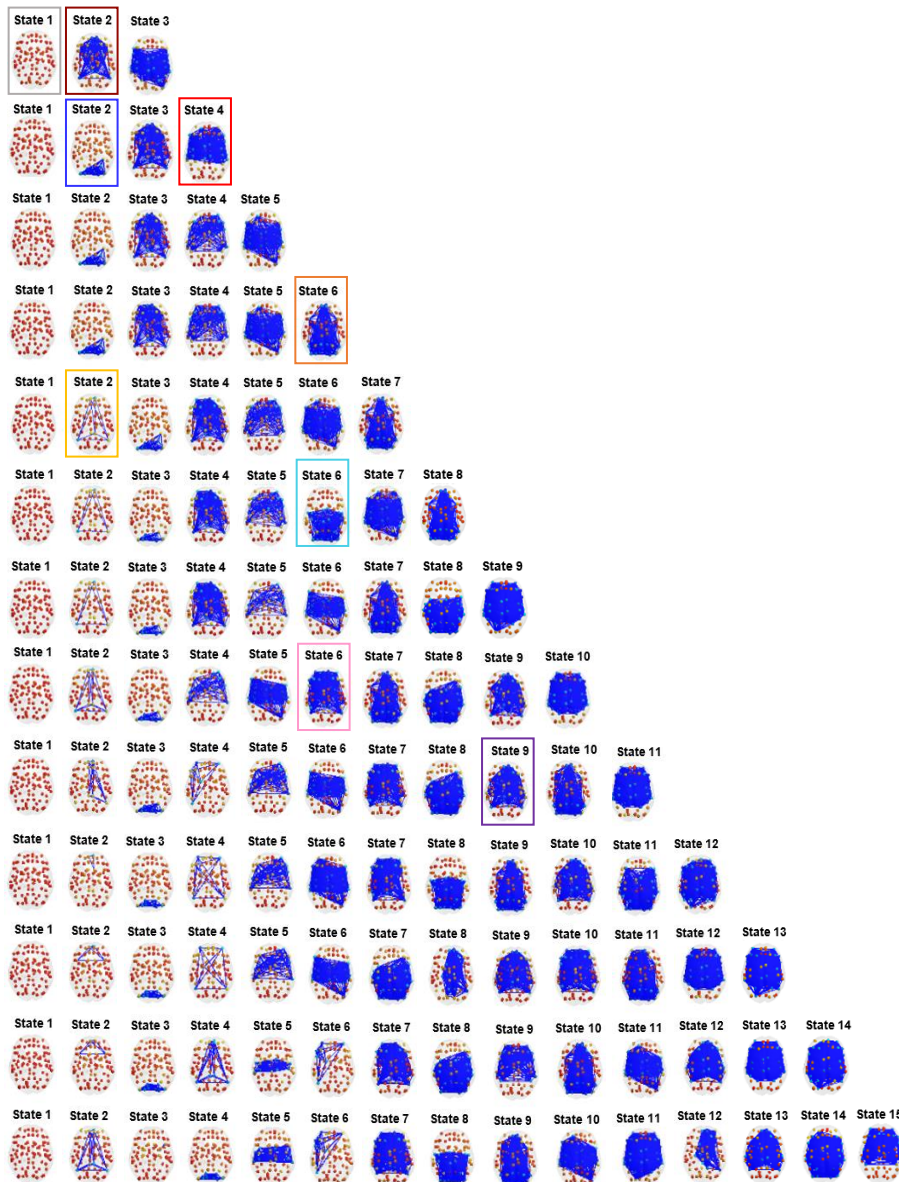


Figure 4.3. dFC states obtained with the k-means clustering algorithm ($k = 3$ to $k = 15$), displayed according to their decreasing probability of occurrence within each $k$, for the AAL90 atlas as the brain parcellation scheme and PC as the method to compute dFC. Each dFC state is represented by its $V_c$ as a network in the AAL90 cortical space (axial slice), in which the elements of $V_c$ are placed at the center of gravity of the respective brain region, shaped as spheres colored according to their sign (red to yellow spheres represent positive elements from 1 to 0, cyan to dark blue spheres represent negative elements from 0 to -1), and areas with $V_c \leq 0.1$ are linked with dark blue edges. States marked with coloured rectangles reappear throughout the FC repertoire.

By looking at Figure 4.3., it was found that state 1 (coloured in grey for the lowest $k$ in which it is observable) appears consistently across all clustering solutions and, regardless of the chosen $k$, is the most prevalent state. This fully connected cluster exhibits all brain regions with BOLD phases aligned with each other and projected toward the same direction into the leading eigenvector (i.e., only positive red elements in the cluster centroid vector), and does not show the separation of any particular subsystem nor a significant correlation with RSNs of reference, being called the global mode. This state is extensively reported in the literature [83][86][89].

From the second state on, small groups of brain regions exhibit BOLD phases that deviate from the global coherence state and start to form functional networks (areas with $V_c$ equal or inferior to 0.1 linked by the dark blue edges). For example, state 2 for $k = 3$ (coloured in brown) is characterised by a network composed of regions from the frontal lobe (frontal superior medial gyrus, rectal gyrus, and frontal medial orbital, olfactory, anterior and posterior cingulate cortices); parietal lobe (angular gyrus); temporal lobe (middle temporal pole); and subcortical regions (hippocampus and amygdala). This state reappears in other $k$'s, such as in $k = 4$ to $k = 6$ (state 3), $k = 7$ to $k = 9$ (state 4) and $k = 14$ (state 7), and is reported in several studies [89][111][115].

Furthermore, this pattern can be identified with some modifications. It appears in a lesser extent in $k = 7$ to $k = 11$ (state 2), $k = 14$ (state 4) and $k = 15$ (state 2) (coloured in yellow), and with additional regions in $k = 10$ (state 6), $k = 11$ and $k = 12$ (state 7), $k = 13$ (state 10) and $k = 15$ (state 7) (coloured in pink), namely including the frontal lobe (frontal superior gyrus, frontal superior, middle and inferior orbital gyri, and frontal inferior triangular gyrus); parietal lobe (parietal inferior gyrus); temporal lobe (Heschl's and temporal inferior gyri); and subcortical regions (caudate nucleus and lenticular nucleus putamen). Other variations of this network can be identified, one including less regions in the frontal lobe for $k = 11$ (state 9), $k = 12$ (state 10), $k = 13$ (state 9), $k = 14$ (state 12) and $k = 15$ (state 13) (colored in purple), and another one extending to the occipital lobe for $k = 6$ (state 6), $k = 7$ (state 7), $k = 8$ (state 8), $k = 9$ and $k = 10$ (state 7), $k = 11$ (state 10), $k = 12$ (state 9), $k = 13$ (state 11), $k = 14$ (state 10) and $k = 15$ (state 9) (colored in orange).

Another FC configuration characteristic of all $k$'s is the network composed of regions from the occipital lobe, mainly including the calcarine fissure, cuneus cortex, occipital superior, middle and inferior gyrus, and lingual gyrus, as well as the network including the frontal pole (frontal superior and middle orbital gyri, frontal middle gyrus, frontal inferior opercular and triangular gyri, and rolandic operculum); insular cortex, located deep within the lateral sulcus and hidden bellow parts of the frontal, parietal and temporal lobes [117]; parietal lobe (supramarginal gyrus); and subcortical regions (lenticular nuclei putamen and pallidum). The first functional subsystem is observed in state 2 for $k = 4$ to $k = 6$, state 3 for $k = 7$ to $k = 14$ and state 4 for $k = 15$ (dark blue), and the second one is present in state 4 for $k = 4$ to $k = 6$, state 5 for $k = 7$ to $k = 9$, state 4 for $k = 10$, state 5 for $k = 11$ to $k = 13$, state 9 for $k = 14$ and state 15 for $k = 15$ (red). Both networks are aligned to the findings reported in the literature [83][89][111]. Moreover, it is also interesting to notice that one cluster appears for the first time in $k = 8$ (state 6), but is consistently verified for higher $k$'s (state 8 for $k = 9$ to $k = 12$, state 7 for $k = 13$ and state 8 for $k = 14$ and $k = 15$) (cyan blue) and in the literature [89][111][115].

By examining the formation of the functional networks throughout the whole range of $k$'s, it was found

that higher values of *k* provide more fine-grained network configurations, which tend to be less frequent and, in some cases, less symmetric. Results also reveal that, when *k* increases, some networks reappear throughout the range of *k*'s (and sometimes within each *k*), often covering a wider set of brain regions and forming more extensive networks.

### 4.3.1. Impact of a robust preprocessing (ICA clean-up and nuisance regression)

rs-fMRI data analysed in Figure 4.3. underwent a preprocessing sequence including the semi-automatic classification of ICs into the signal of interest or noise, with the subsequent ICA noise clean-up and nuisance regression, as described in section 3.2.1. To evaluate the influence on the dFC states of performing these additional clean-up steps in the rs-fMRI data preprocessing, the dFC analysis was repeated on minimally preprocessed rs-fMRI data, which did not include ICA clean-up and nuisance regression. The obtained FC repertoire for $k = 3$ to $k = 15$ can be consulted in Figure B.2. of Appendix B.

The recurrent dFC states obtained without the two denoising techniques revealed similarities with those obtained without their implementation, exhibiting the same characteristic FC patterns described in the previous section. However, a major discrepancy was found: a remarkable frontal pattern (see Figure 4.4.), which was not identified in the results obtained with the ICA clean-up and nuisance regression, appeared in the group analysis without these steps from $k = 6$ to $k = 14$, with the second-highest probability of occurrence until $k = 13$ and the third-highest one in $k = 14$. For the partition model represented in Figure 4.4. ($k = 6$), this state is the second most prevalent functional subsystem (probability of occurrence ± standard error = 0.146 ± 0.007) and the third longest-lasting state on average (mean lifetime ± standard error = 4.28 ± 0.46 TR). It is characterised by a set of frontal regions whose BOLD phases deviate from the global mode, namely the frontal superior and middle orbital gyri, gyrus rectus, and frontal medial orbital and olfactory cortices (Figure 3.1.).
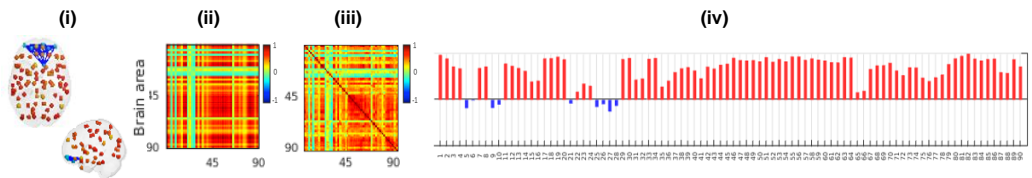


Figure 4.4. Frontal state obtained with the k-means clustering algorithm (state 2, $k = 6$), for the rs-fMRI data preprocessing without the ICA clean-up and nuisance regression steps, for the AAL90 atlas and PC method. This dFC state is represented by its $V_c$: **(i)** as a network in the AAL90 cortical space (axial slice), in which the elements of $V_c$ are placed at the center of gravity of the respective brain region, shaped as spheres colored according to their sign (red to yellow spheres represent positive elements from 1 to 0, cyan to dark blue spheres represent negative elements from 0 to -1), and areas with $V_c \leq 0.1$ are linked with dark blue edges; **(ii)** by the outer product $V_c V_c^T$; and **(iv)** as a bar plot displaying the projection of the BOLD phase in each brain region into $V_c$. This dFC state is also characterised by its **(iii)** dFC matrix.

A plausible explanation for the emergence of this dFC state in the repertoire obtained without the more refined preprocessing is its artefactual origin. The frontal location of the functional network suggests that it could correlate with susceptibility artefacts arisen from field inhomogeneities due to the magnetic susceptibility difference in the air/bone tissue interface, which would make the effect of any motion (e.g. head motion or eye movement) more impactful. Hence, the removal of such susceptibility artefact with the ICA clean-up would explain its absence in the repertoire obtained with that preprocessing step and its prevalence in the results obtained with the denoising.

### 4.3.1.1. Correlation of dFC states with RSNs

In order to understand the impact of implementing the ICA clean-up and nuisance regression preprocessing steps in the relative validity of results, the cluster centroid vectors of the dFC states obtained with and without the denoising were compared to well-established RSNs, as explained before in section 3.2.5.1. Figure 4.5. displays the Pearson correlation coefficient computed between the cluster centroid vectors of the dFC states obtained for the partition model $k = 6$, with and without implementing these two additional preprocessing steps, and the seven Yeo transformed RSNs vectors.
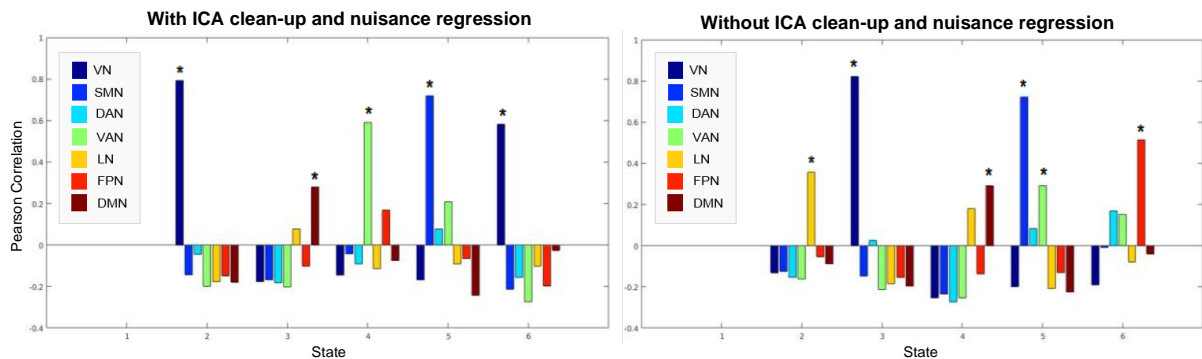


Figure 4.5. Pearson correlation coefficient computed between the cluster centroid vectors of the dFC states ($k = 6$) obtained with the PC method and the seven Yeo RSNs transformed into the AAL90 space, with and without the ICA clean-up and nuisance regression preprocessing steps. *: Statistically significant correlations after correcting for the number of clusters ($p$-value < 0.05/$k$); VN = Visual Network; SMN = Somatomotor Network; DAN = Dorsal Attention Network; VAN = Ventral Attention Network; LN = Limbic Network; FPN = Frontoparietal Network; DMN = Default Mode Network.

Results show that, regardless of implementing the ICA clean-up and nuisance regression steps, there are statistically significant correlations of the dFC states with the VN, SMN, VAN and DMN. Notwithstanding, it can be inferred that the results obtained with the denoising show more specificity in detecting RSNs, as on the right plot of Figure 4.5., the SMN and VAN appear intermingled in state 5.

Furthermore, it is interesting to note that, in the results obtained without the ICA clean-up and nuisance regression steps, the frontal state 2, previously associated with susceptibility artefacts, exhibits a significant correlation to the LN (Pearson correlation coefficient $r = 0.36$, $p$-value = $5.44 * 10^{-4}$), and state 6 appears correlated with the FPN ($r = 0.51$, $p$-value = $2.13 * 10^{-7}$). These two functional subsystems do not arise in the results obtained with the denoising for $k = 6$, which leads to question whether this state has, in fact, an artefactual origin, or the ICA clean-up incorrectly eliminated frontal and limbic components that were not purely artefactual.

Hence, to clarify the relevance of performing a robust preprocessing in rs-fMRI data, the auto-classification of ICs should be reviewed across subjects that spent more time in the frontal state (see Figure 4.6., subjects 3 and 8) or held that synchronisation pattern in specific epochs (Figure 4.6., subject 7). In both cases, the correlation of the occurrence of the frontal state with the motion parameters (time courses) of the respective subject could be a strong evidence of artefactual origin. However, this was not evident in our data.
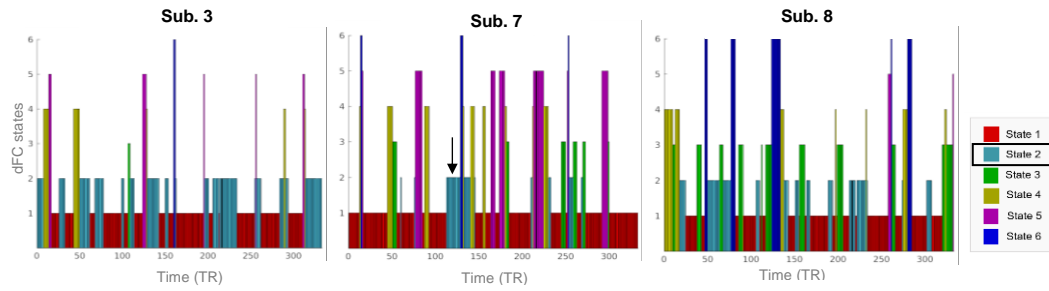
Figure 4.6. Cluster time courses ($k = 6$) across subjects 3, 7 and 8, obtained with the PC and without the ICA clean-up and nuisance regression preprocessing steps. The subjects 3, 7 and 8 spent, respectively, 38.7 %, 11.7 % and 23.1 % of the total acquisition time on the frontal state (state 2). The occurrence of the frontal state in a specific epoch is denoted with a black arrow. Sub. = Subject.

## 4.3.2. Comparison between SW and PC methods

In order to evaluate how dFC states varied between methods, the k-means clustering algorithm with $k = 5$ was run for both PC and SW (with sizes of 25 TR, 35 TR and 45 TR and step of 1 TR). This partition model was chosen since it has been used in several studies as the best clustering solution to represent FC data [83][86] and provides a low set of synchronisation patterns, facilitating the following analyses. The results are depicted in Figure 4.7.
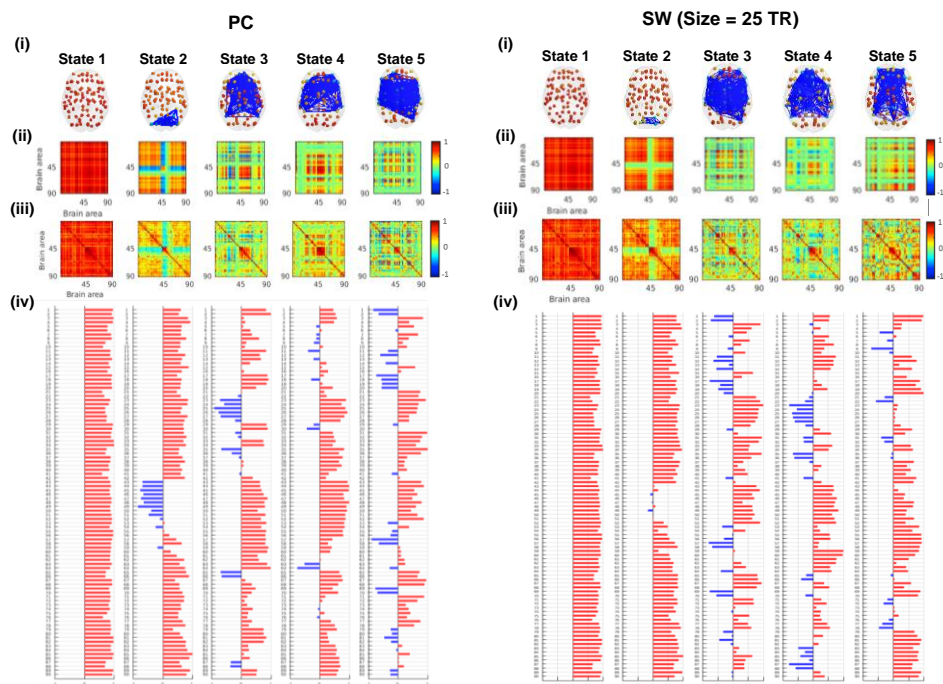


Figure 4.7. dFC states obtained with the k-means clustering algorithm ($k = 5$), displayed according to their decreasing probability of occurrence, for the AAL90 atlas and PC and SW (sizes of 25 TR, 35 TR and 45 TR, step of 1 TR) methods. Each dFC state is represented by its $V_c$: **(i)** as a network in the AAL90 cortical space (axial slice), in which the elements of $V_c$ are placed at the center of gravity of the respective brain region, shaped as spheres colored according to their sign (red to yellow spheres represent positive elements from 1 to 0, cyan to dark blue spheres represent negative elements from 0 to -1), and areas with $V_c \leq 0.1$ are linked with dark blue edges; **(ii)** by the outer product $V_c V_c^T$; and **(iv)** as a bar plot displaying the projection of the BOLD phase in each brain region into $V_c$. Each dFC state is also characterised by its **(iii)** dFC matrix.

Figure 4.7. *(Continued)*

Although the average dFC matrices yielded by PC method presented a high degree of similarity with those yielded by SW (Figure 4.1.), results obtained with the k-means clustering algorithm for $k = 5$ reveal that the dFC states differ greatly between both methods.

By qualitative analysis of Figure 4.7., the FC patterns identified with the PC seem to be more consistent with those obtained with the SW of 25 TR, showing notable deviations compared to the results of SWs with larger sizes (35 TR and 45 TR) that present more irregular states. In particular, the occipital state, which is observed in the PC FC repertoire from $k = 4$ to $k = 15$ (see Figure 4.3.) and validated in the PC literature [86][118], can be identified in the results obtained with the SW of 25 TR (although with less pronunciation than in PC) but it does not appear for the wider SWs.

### 4.3.2.1. Correlation of cluster centroid vectors between methods

To quantitatively understand the similarities between the dFC states obtained with different methods, the Pearson correlation coefficient was computed for each pair of cluster centroid vectors (excluding the global mode) obtained with the PC and SW methods for the partition model $k = 5$ (Figure 4.8.).
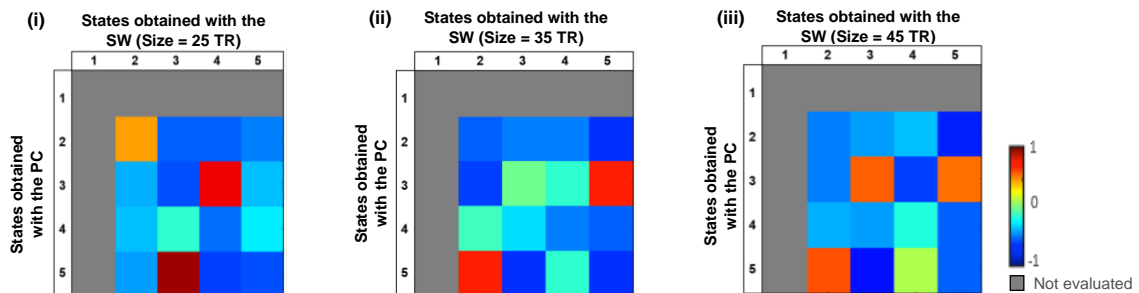


Figure 4.8. Pearson correlation coefficient computed between the cluster centroid vectors of the dFC states ($k = 5$) obtained with the PC method and the SW of **(i)** 25 TR, **(ii)** 35 TR and **(iii)** 45 TR.

By analysing the correlation matrices, it was not found any univocal correlation between states of different methods. However, results from Figure 4.8. **(i)** reveal that the centroid vectors of state 2, state 3 and state 5 obtained with PC and those of state 2, state 4 and state 3 identified with the SW with a size of 25 TR are, respectively, meaningfully correlated. For the dFC states yielded by larger SWs, the number of correlated states increases, such that a single state from the PC FC repertoire presents multiple meaningful correlations with states yielded by SW (e.g., in Figure 4.8. **(iii)**, the state 3 obtained with the PC is greatly correlated with state 3 and state 5 yielded by SW of 45 TR). This suggests that, contrarily to the PC, the functional subsystems identified with the SW start to appear intermingled within each cluster, such that the correlation departs from univocity.

Furthermore, results show that the wider the window, the lower the correlation with the centroid vectors obtained with the PC (the maximum $r$ in Figure 4.8. **(i)**, **(ii)** and **(iii)** is 0.95, 0.75 and 0.69, respectively). Hence, this quantitative analysis reinforces the higher degree of similarity between the repertoire obtained with the PC and the SW of 25 TR, and the divergence of results for larger windows, as expected. In fact, although the connectivity time courses yielded by PC and SW of 45 TR display slightly higher similarity (Figure 4.1.), smaller SWs produce dynamic analyses on closer temporal scales (or resolution), and therefore yield more similar dFC states.

### 4.3.2.2. Correlation of dFC states with RSNs

In order to quantitatively assess the influence of using the PC or SW on the relative validity of the results, the cluster centroid vectors of the dFC states obtained with both methods were compared to well-established RSNs from literature. Figure 4.9. shows the Pearson correlation coefficient computed between the cluster centroid vectors of the dFC states obtained with the PC and the SWs for $k = 5$ and the seven Yeo transformed RSNs vectors.

Results reveal that the FC patterns obtained with the PC present statistically significant correlations with the VN ($r = 0.80$, $p$-value = $2.27 * 10^{-21}$), SMN ($r = 0.73$, $p$-value = $5.27 * 10^{-16}$), VAN ($r = 0.58$, $p$-value = $1.53 * 10^{-9}$) and DMN ($r = 0.28$, $p$-value = $7.40 * 10^{-3}$) in distinct clusters.

In the SW of 25 TR, the VN is also detected separately in state 2, although it does not present a statistically significant correlation with the Yeo RSN. Regarding the remaining SWs, the VN arises in the state 5 obtained with the window of 35 TR ($r = -0.31$, $p$-value = $2.80 * 10^{-3}$) and 45 TR ($r = -0.32$, $p$-value = $2.10 * 10^{-3}$), though, it is not detected separately, as it appears intermingled with the DMN with lower correlation coefficients (absolute value) and statistical significance ($r = 0.38$, $p$-value = $2.29 * 10^{-4}$ for the SW of 35 TR and $r = 0.34$, $p$-value = $1.00 * 10^{-3}$ for a size of 45 TR). In the SW of 25 TR, the DMN arises separately in state 4 ($r = 0.34$, $p$-value = $9.10 * 10^{-4}$). Regarding the SMN, it appears for the three SWs ($r = 0.66$, $p$-value = $1.02 * 10^{-12}$ for the SW of 25 TR, $r = 0.42$, $p$-value = $3.76 * 10^{-5}$ for a size of 35 TR, and $r = 0.52$, $p$-value = $1.89 * 10^{-7}$ for a size of 45 TR).

In contrast to the PC method, none of the SWs can detect the VAN. However, in the results obtained with the window of 45 TR, the DAN arises in state 4 ($r = 0.41$, $p$-value = $6.36 * 10^{-5}$). This network does not correlate with any dFC state obtained with the PC.
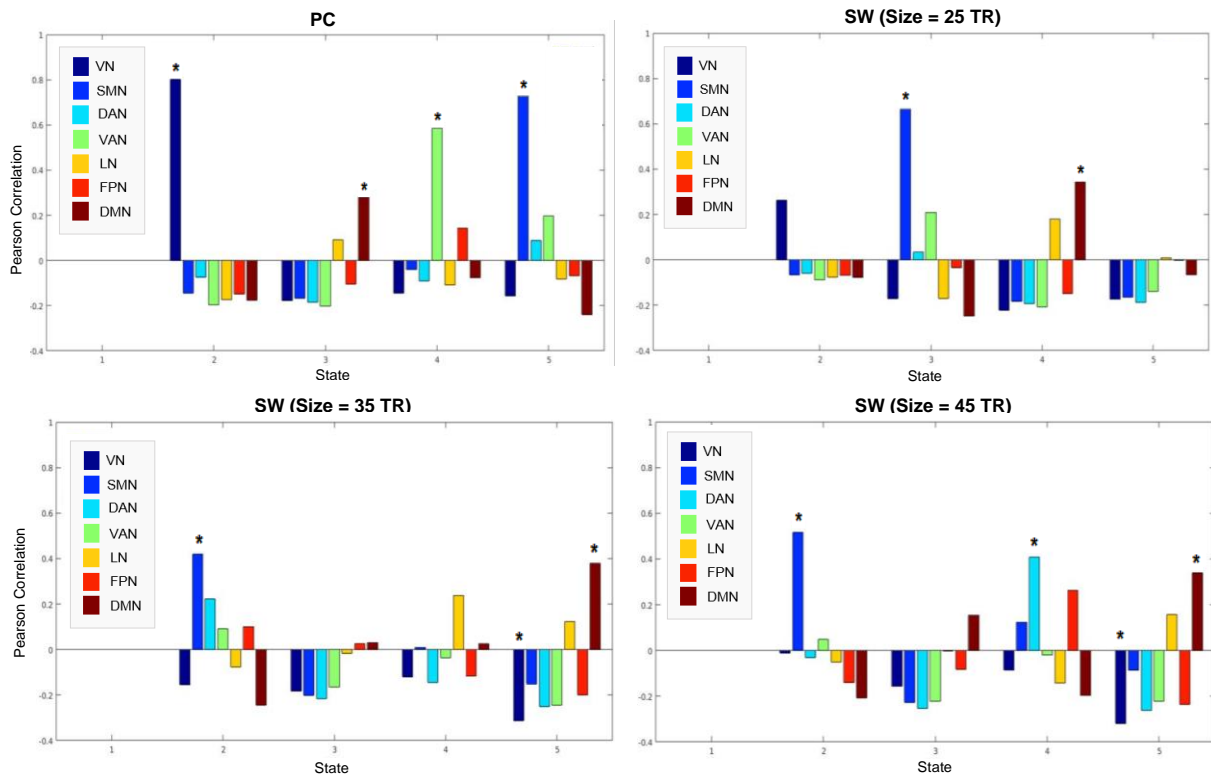
Figure 4.9. Pearson correlation coefficient computed between the cluster centroid vectors of the dFC states ($k$ = 5) obtained with the PC and SW (sizes of 25 TR, 35 TR and 45 TR) methods and the seven Yeo RSNs transformed into the AAL90 space. *: Statistically significant correlations after correcting for the number of clusters ($p$-value < 0.05/$k$); VN = Visual Network; SMN = Somatomotor Network; DAN = Dorsal Attention Network; VAN = Ventral Attention Network; LN = Limbic Network; FPN = Frontoparietal Network; DMN = Default Mode Network.

Hence, results suggest that the recurrent states obtained with the PC method are more similar to the functional networks of reference VN and SMN than those obtained with the SW method (higher correlation coefficients) and present stronger statistical significance, i.e., lower $p$-values. Furthermore, excluding the global mode, while each of the four dFC states obtained with the PC method presents a statistically significant correlation to one network of reference (in total, four Yeo RSNs are detected), states obtained with the SWs of 25 TR, 35 TR, and 45 TR significantly correlate with a total of two, three, and four Yeo RSNs, respectively. These observations show that, for the shortest window size, just half of the Yeo RSNs is significantly detected compared to the PC results, and for larger window sizes, the overlap with the Yeo RSNs increases, but they start to appear intermingled within each state. Thus, we may speculate that the PC is more sensitive than SW in detecting RSNs, presumably due to the inherently higher temporal resolution

As explored previously in section 2.2.2.4., whereas the PC method allows for a maximal temporal resolution, estimating the instantaneous synchronisation of BOLD phases (one connectivity matrix per TR), the SW describes statistical relationships between brain regions within successive fixed-length windows (25 TR, 35 TR and 45 TR, in this case). Thus, the concept underlying the SW method implies focusing on the lower frequencies of the data (introduction of 31.5 s, 44.1 s and 56.7 s of period, respectively), which worsens the temporal resolution and may affect the detection of recurrent FC patterns with shorter mean lifetimes (i.e., that occur more rapidly). It should also be noted that the percentage of variance explained by the leading eigenvector was not above 50 % for all data points in

the SW, which may have led to a misleading representation of the FC dominant pattern by the leading eigenvectors in some cases, and affected the representation of dFC states.

Therefore, although the PC presents more susceptibility to noise than the SW, results suggest that it is more suitable to assess faster fluctuations of dFC, since it captures a dynamic that effectively exists and is not purely noise (otherwise the SW would probably detect it more reliably). This conclusion was also presented by Cabral and colleagues [83], which suggested the existence of a fast dynamic of functional FC patterns evolving, at least, at the temporal resolution of acquisition (in this case, corresponding to TR = 1.26 s), which would only be detected by keeping the high frequency components of the BOLD signal.

### 4.3.2.3. Dynamics of FC states

In order to compare the dynamics of dFC states obtained with the PC and SW methods, their mean lifetime and probability of occurrence are displayed in Figure 4.10. for the partition model $k = 5$. Furthermore, the impact of implementing a temporal smoothing algorithm on the dFC labels of the states was also analysed.
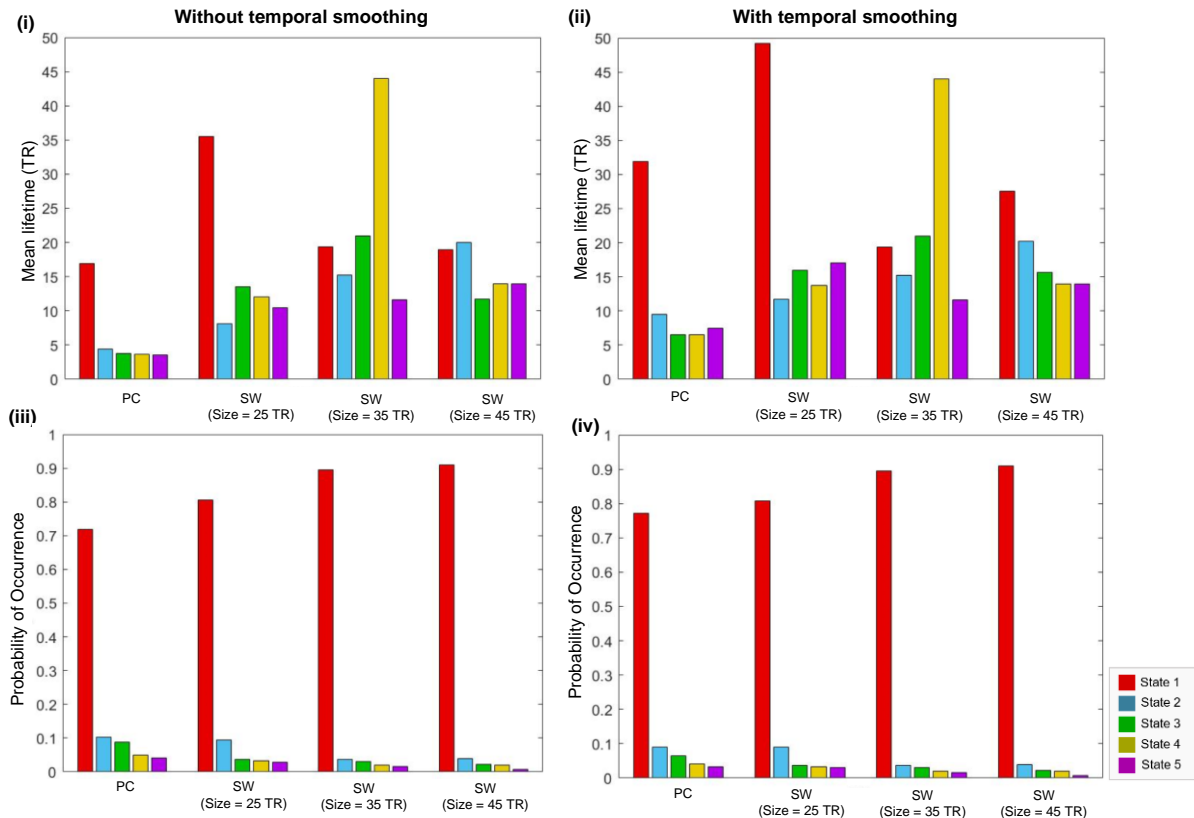


Figure 4.10. Mean lifetime (**i**, **ii**) and probability of occurrence (**iii**, **iv**) of each dFC state ($k = 5$), obtained without and with the implementation of the temporal smoothing algorithm to the dFC labels, respectively, for the PC and SW with window sizes of 25 TR, 35 TR and 45 TR.

Firstly, by comparing the mean lifetimes across the dFC states obtained with the PC, without (Figure 4.10. **(i)**) and with (Figure 4.10. **(ii)**) the temporal smoothing of the dFC labels, the global mode presents the longest mean lifetime in both cases (16.96 ± 2.15 TR and 31.88 ± 7.05 TR, respectively). The remaining states (state 2 to state 5) last less than 5 TR without the temporal filter (4.44 ± 0.41 TR, 3.76 ± 0.45 TR, 3.71 ± 0.65 TR and 3.56 ± 0.78 TR, respectively), and more than 6.5 TR with the filter (9.54

± 0.97 TR, 6.52 ± 0.77 TR, 6.53 ± 1.12 TR and 7.50 ± 1.48 TR, respectively).

In fact, the main impact of implementing the temporal smoothing is the increase of the duration of the states, since it imposes a minimum lifetime for the FC patterns (10 s, corresponding to 7.94 TR), ensuring that they do not switch faster than the highest frequency of the BOLD signal (0.1 Hz). Table 4.1. shows the increased averaged mean lifetimes across states with the temporal smoothing algorithm vs. without its implementation. However, since the temporal smoothing is not strict (no imposition of a cut-off frequency), the duration of the states can be slightly inferior to 7.94 TR, which is verified for state 3 to state 5 obtained with the PC (Figure 4.10. **(ii)**). Also, since the filter affects all states equally, the relative probabilities of occurrence present similar behaviours (Figure 4.10. **(iii)** and **(iv)**).

Table 4.1. Average of mean lifetimes across the five dFC states (k = 5) obtained with the AAL90 atlas, without and with temporal smoothing of the state labels.

| | Average of mean lifetimes across the dFC states (TR) | | | |
|---|---|---|---|---|
| | **PC** | **SW (Size = 25 TR)** | **SW (Size = 35 TR)** | **SW (Size = 45 TR)** |
| **Without temporal smoothing** | 6.49 ± 2.35 | 15.94 ± 4.46 | 22.24 ± 5.08 | 15.75 ± 1.42 |
| **With temporal smoothing** | 12.40 ± 4.38 | 21.55 ± 6.24 | 22.24 ± 5.08 | 18.28 ± 2.30 |

Next, by comparing the temporal metrics between the PC and SW methods without the implementation of the temporal smoothing to the dFC labels (see Figure 4.10. **(i)** and first row of Table 4.1), it was found that the mean lifetimes of the dFC states are higher in the SW. Within the SW method, since the duration of the states tends to increase for wider window sizes, the mean lifetime of the global mode decreases, approximating the duration of the remaining patterns.

In fact, as described in the previous section, the SW method focuses on the lower frequency components of the BOLD signal. This method introduces by itself a temporal smoothing (or low-pass filtering) during the estimation of the FC within successive intervals of time, which increases the period of fluctuations and the mean lifetimes of the dFC states. Thus, synchronisation patterns with mean lifetimes shorter than the window size are hardly detected by this method. Following the same reasoning, wider window sizes (stricter low-pass filter) are expected to originate dFC states with higher mean lifetimes on average, which is also observed (except for the SW with a size of 45 TR).

The findings above do not clarify whether the FC patterns present short mean lifetimes that appear longer in the SW because the method extends their duration over time and excludes shorter instances, or if the states have, in fact, high mean lifetimes, being better detected by filtering the high frequencies of the signal. Nonetheless, the correlation with the Yeo repertoire analysed in section 4.3.2.2. shows the importance of a fine-grained temporal specificity in detecting functional networks, and Cabral et al. [83] emphasize the relevance of keeping the higher frequencies of the BOLD signal to detect the fast evolution of the dFC at a scale at least as fast as the acquisition TR. These observations point to the ability of the PC method to capture a fast functional dynamic that exists and approximates the dynamic of the rs-fMRI (0.01 Hz to 0.1 Hz), which can not be reproduced with the SW method.

Furthermore, Figure 4.10. **(iii)** reveals that, without implementing the temporal filter to the dFC labels, the global coherence state tends to be more prevalent (higher probability of occurrence) and occur in

shorter continuous time periods (lower mean lifetime) for the SW method than the PC method. As expected, the higher the probability of occurrence of the global mode, the lower the probabilities of the remaining FC patterns, which is visually detected in the same figure.

Since the goal of the PC method is to analyse the dFC at each TR (maximal temporal resolution) and detect states that can evolve, at least, at the temporal resolution of acquisition, the application of the temporal smoothing algorithm was not considered in the following analyses.

**(i) Comparison between SW and PC methods in the HCP dataset**

The main goal of repeating the previous analyses in the HCP dataset was to validate the results obtained in sections 4.3.2.2. and 4.3.2.3. in a larger dataset. The results can be found in Appendix C.

Comparing PC and SW, both methods provide similar dFC states significantly correlated with the same RSNs, contrarily to the migraine dataset. This is consistent with findings from Pedersan et al. [119] and Honari et al. [120], which also analyse the HCP dataset and suggest that PC and SW convey comparable connectivity information and similar brain states, with PC ensuring finer temporal resolution. In fact, since the Yeo's template was originated from a large dataset [61], reference RSNs are expected to be more easily recoverable when more data are analysed. Hence, this observation suggests that the choice of the method to compute the dFC (either through the synchronisation of BOLD phases or the pairwise Pearson correlation coefficient) is more critical for smaller datasets.

Moreover, the analysis of the temporal metrics of the dFC states for the partition model $k = 5$ in the HCP dataset reinforces the dynamic behaviour described for the migraine dataset. The duration of dFC states is overall higher in the SW method, and the wider the window, the higher the mean lifetimes. One should note that this trend revealed a more linear behaviour for the HCP dataset, which was expected due to the much higher number of subjects. Regarding the probabilities of occurrence, the global mode is again the most likely state to occur. Furthermore, its probability of occurrence is higher in the SW method when compared to the PC, and displays a positive tendency for larger sizes.

### 4.3.2.4. Subject-level assessment

The k-means clustering analysis at a group-level contributed to evaluating the recurrent FC patterns across the whole interictal dataset. In this section, the subject-level differences are explored, concerning the cluster time courses and the sFC analyses.

**(i) Cluster time courses**

Figure 4.11. displays the dFC labels obtained for each subject with the PC and SW of 25 TR over time, for $k = 5$. Firstly, by comparing the cluster time courses between the PC and SW, the longer duration of the states obtained with the second method is visually ascertained (each pattern occurs in longer continuous time periods).

Then, results reveal that the distribution of recurrent FC patterns over time is highly heterogeneous across subjects. Whereas some participants exhibit synchronisation patterns that switch between all states over time (all subjects for the PC method except subject 2 and 4, and subjects 6 and 7 for the SW), others present patterns transiting from the global mode to just one (subjects 5 for the SW), two (subjects 2, 3 and 8 for the SW) or three (subjects 2 and 4 for the PC, subject 1 for the SW) states.

Regarding subject 4, the PC method detects fluctuations of FC from the global mode to states 2, 3 and 4, and the SW does not detect any transition during the whole rs-fMRI scan (the participant remains in the global mode). These observations confirm that the number of detected states for each subject is overall higher in PC and show how the reduced temporal resolution of SW may lead the method to fail in capturing some recurrent states.
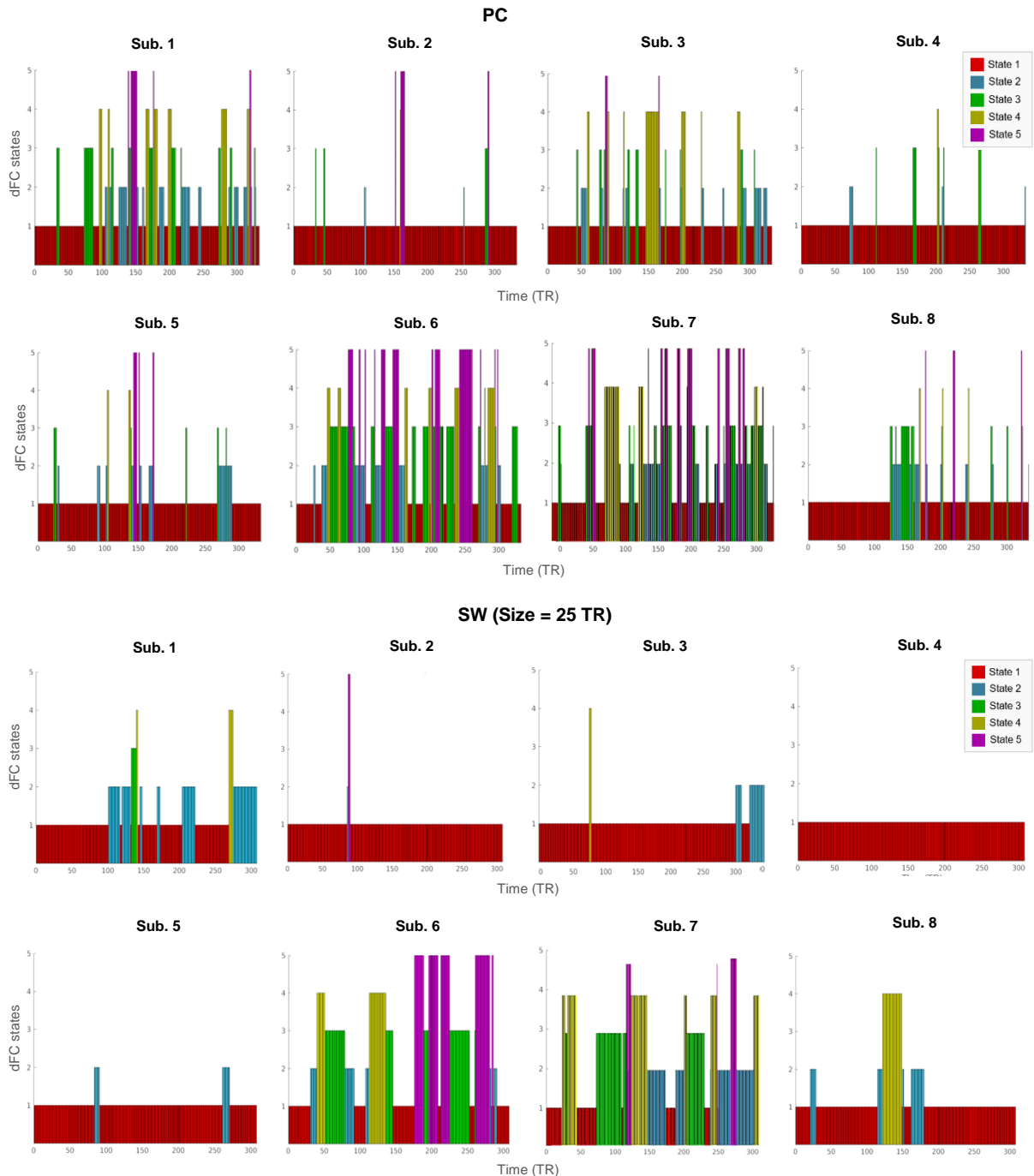


Figure 4.11. Cluster time courses ($k = 5$) across subjects obtained with the PC and SW with a size of 25 TR. Sub. = Subject.

## (ii) sFC analysis

To assess the behaviour of the FC assuming stationarity over short time periods at a subject-level, Figure 4.12. displays the sFC observed for each subject during the acquisition time, obtained by avera-

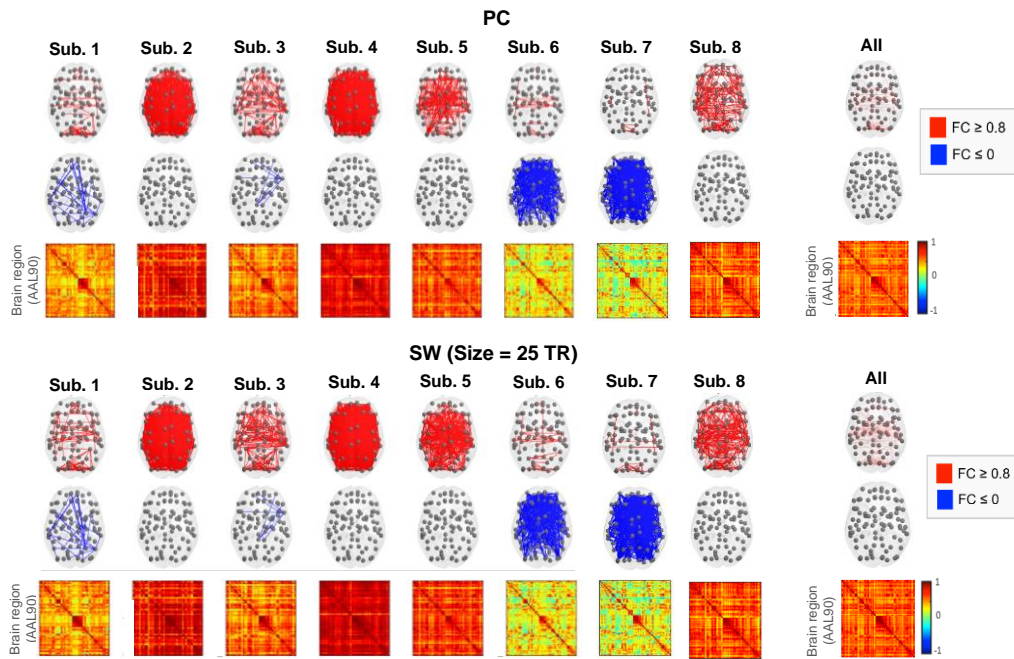ging the dFC matrices obtained with the PC and the SW of 25 TR over time.



Figure 4.12. sFC across subjects obtained with the PC and SW with a size of 25 TR. Subj. = Subject; FC = Functional Connectivity.

Firstly, the average of the FC over the acquisition time is not expected to vary greatly between methods, which is observable in Figure 4.12.

Furthermore, results reveal evident differences across participants. Subjects 2 and 4 spent most of the scan duration in the global coherence state (94.0 % and 93.4 % of the time, respectively, with the PC, and 98.7 % and 100 % of the time, respectively, with the SW), as already visualised in Figure 4.11. Thus, since the longer the duration of the dFC state, the closer it gets to the averaged static connectivity, the sFC of these subjects reveal a strong (FC ≥ 0.8) fully connected state following the global mode.

Moreover, the strong positive sFC patterns (FC ≥ 0.8) obtained for subject 1 reveal the predominance of the occipital state (VN), which is extensively found across the clustering results obtained for the group-level analysis (Figure 4.3). For the same subject, the negative sFC patterns reveal a functional subsystem that, by visual analysis, seems to be forming the DMN.

Despite the few common synchronisation patterns identified with the sFC and dFC analyses, results prove that the dFC assessment captures FC alterations that are not detected with the conventional sFC, being the first method better suited to model the dynamic changes of the human brain.

Next, in order to evaluate the similarities between the sFC matrices obtained for all subjects and the ones obtained with the dFC analysis for each method (PC and SW with three window sizes), the Pearson correlation coefficient was computed between the sFC matrix averaged across all subjects and the sum of the $V_cV_c^T$ matrices (Figure 4.7. **(ii)**) weighted with the probability of occurrence of the states. The correlation coefficients obtained for the PC and SWs of 25 TR, 35 TR and 45 TR were, respectively, $r = 0.80$, $r = 0.72$, $r = 0.70$ and $r = 0.69$ for the partition model $k = 5$. These results show that the sFC matrix can be fairly described as a linear combination of the five eigenvectors in all methods, but the PC better captures the coupling between BOLD signals than the SW, which tends to get worse for larger sizes. In turn, for $k = 10$, the results obtained with these methods were, respectively, $r = 0.81$, $r = 0.74$,

$r = 0.72$ and $r = 0.71$, which suggests that the higher the number of eigenvectors (higher $k$), the better the approximation of the weighted sum of the $V_c V_c^T$ matrices to the sFC matrix averaged across all subjects.

## 4.4. Analysis of migraine interictal dataset across atlases: PC method

In order to understand the impact of choosing different brain parcellation schemes in the FC repertoire, the results obtained with the k-means clustering algorithm ($k = 5$ to $k = 12$) and PC method are depicted in Figure 4.13 for the AAL90, AAL116, Desikan and Harvard-Oxford atlases.



Figure 4.13. dFC states obtained with the k-means clustering algorithm ($k = 5$ to $k = 12$), displayed according to their decreasing probability of occurrence within each $k$, for the AAL90, AAL116, Desikan and Harvard-Oxford atlases. Each state is represented by its $V_c$ as a network in the respective atlas cortical space (axial slice), in which the elements of $V_c$ are placed at the center of gravity of the respective brain region, shaped as spheres colored according to their sign (red to yellow spheres represent positive elements from 1 to 0, cyan to dark blue spheres represent negative elements from 0 to -1), and areas with $V_c \leq 0.1$ are linked with dark blue edges. The colored rectangles represent the Yeo transformed RSNs to which the given cluster centroid vector presents a statistically significant Pearson correlation ($p$-value $< 0.05/k$).

**Desikan atlas**

**Harvard-Oxford atlas**
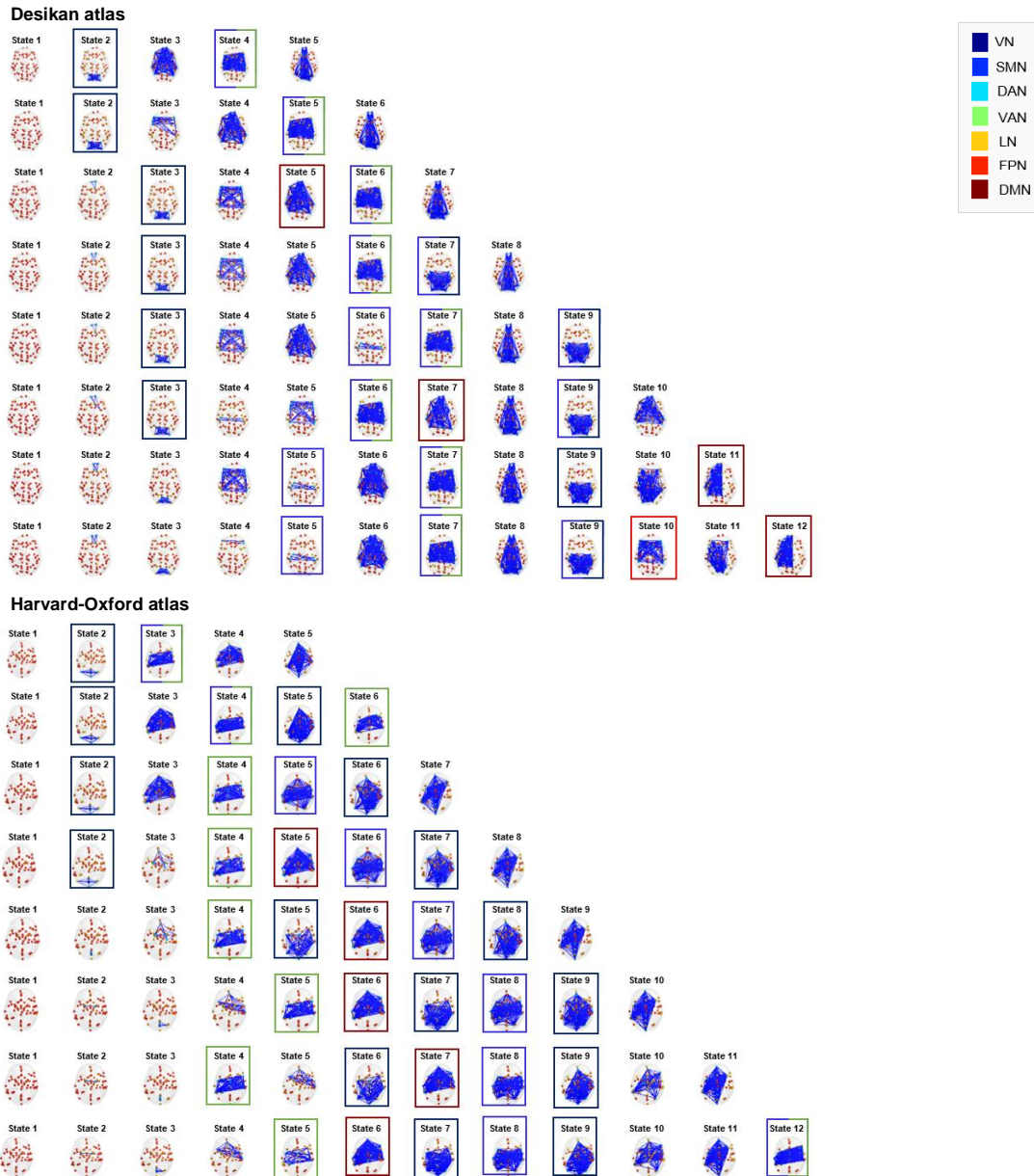
Figure 4.13. (*Continued*).

The statistically significant correlations between the cluster centroid vectors of the dFC states and the seven Yeo transformed RSNs vectors are surrounded with rectangles, coloured according to the Yeo RSN to which the given cluster centroid vector is correlated. One should note that this range of *k*'s was enough to capture non-redundantly the maximum of Yeo RSNs possible across atlases.

The qualitative inspection of Figure 4.13. reveals that the most similar distributions of dFC states are those obtained with the AAL90 and AAL116 atlases, which was expected since the brain parcels are overall identical (see Figure 3.1.: labels 1 to 90 of AAL90 atlas and 1 to 94 of AAL116 atlas). The major difference between these two versions of AAL is the addition of cerebellar regions in the AAL116 atlas (Figure 3.1.: labels 95 to 116). Furthermore, it is interesting to note that the inclusion of the cerebellum in the FC analysis does not contribute to a redistribution of the dFC states. Instead, it appears intermingled with the functional networks as an additional area with a BOLD phase detaching from the global coherence.

This statement is easily noted in Figure 4.14. for the partition model $k = 7$ and states 3, 4, 6 and 7.
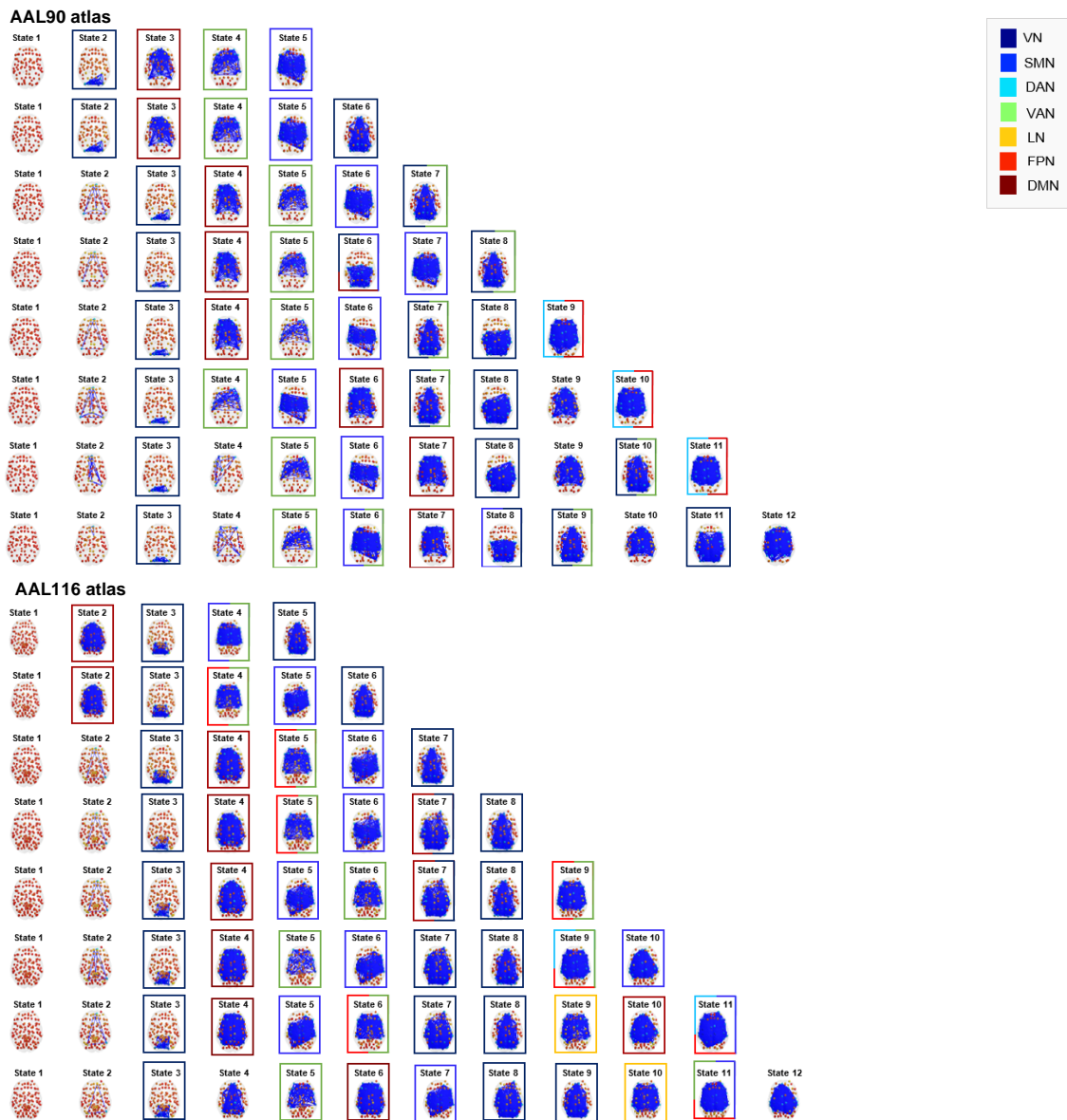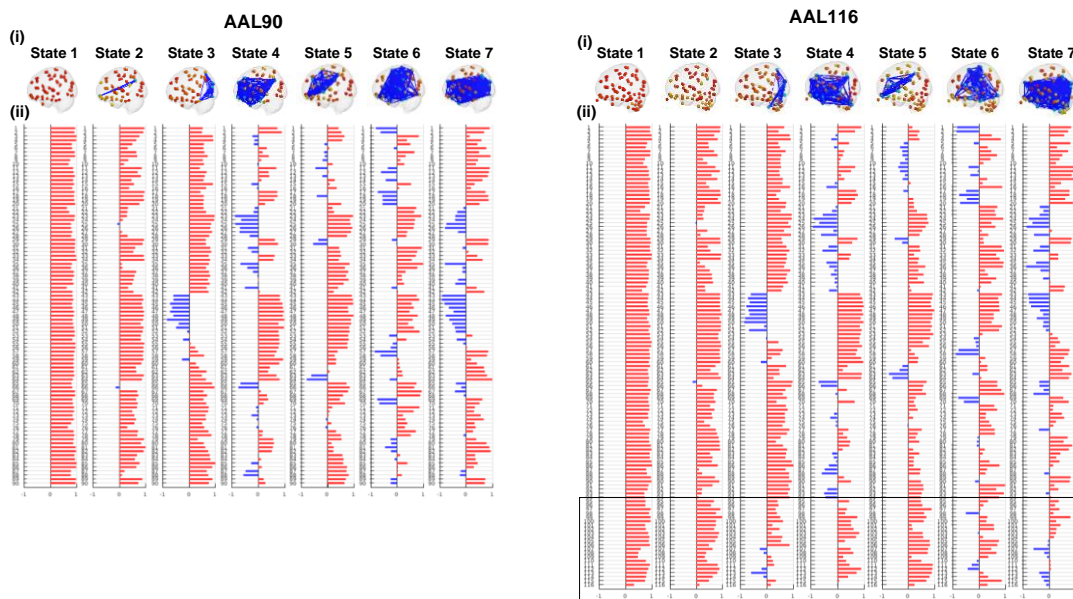


Figure 4.14. dFC states obtained with the k-means clustering algorithm ($k = 7$), displayed according to their decreasing probability of occurrence, for the AAL90 and AAL116 atlases. Each state is represented by its $V_c$ as **(i)** a network in the respective atlas cortical space (axial slice), in which the elements of $V_c$ are placed at the center of gravity of the respective brain region, shaped as spheres colored according to their sign (red to yellow spheres represent positive elements from 1 to 0, cyan to dark blue spheres represent negative elements from 0 to -1), and areas with $V_c \leq 0.1$ are linked with dark blue edges; and **(ii)** a bar plot, showing the projection of the BOLD phase in each brain region into $V_c$. The black rectangle points out the labels of the AAL116 atlas corresponding to the cerebellum.

Additionally, a prevalent dFC state identified in the results obtained with the four atlases is the occipital state, significantly correlated with the VN. To assess its peculiarities in terms of neuromorphology and temporal metrics, this synchronisation pattern is displayed in Figure 4.15.

Figure 4.15. reveals that the occipital state includes the cuneus cortex and lingual gyrus deviating from the global mode across the results of the four atlases. Furthermore, regions belonging to the calcarine part of the cortex are identified in those obtained with the AAL90 and AAL116 (calcarine fissure), Desikan (pericalcarine cortex) and Harvard-Oxford (intracalcarine and supracalcarine cortices). Also, the cortical resolution of the AAL90 and AAL116 parcellation schemes makes it possible to detect shifts in the BOLD phase of the superior, middle and inferior occipital gyri with the first one and in the parahippocampal gyrus with the second one. Some subcortical regions are also identified, such as the amygdala and cerebellum (vermis 1,2) with the AAL116 and the amygdala with the Harvard-Oxford.

Regarding the duration of the occipital state, the mean lifetime is consistent across the AAL90 (3.89 ± 0.43 TR), Desikan (3.40 ± 0.39 TR) and Harvard-Oxford (3.74 ± 0.30 TR) atlases. For the AAL116, the duration of this pattern is discrepantly higher (7.82 ± 0.83 TR). In terms of probabilities of occurrence, this state is more prevalent when obtained from the Harvard-Oxford atlas (probability of 0.094 ± 0.006) and less prevalent when yielded from Desikan (0.063 ± 0.005). For the AAL90 and AAL116 atlases, the probability is similar (0.077 ± 0.006 and 0.076 ± 0.006, respectively).
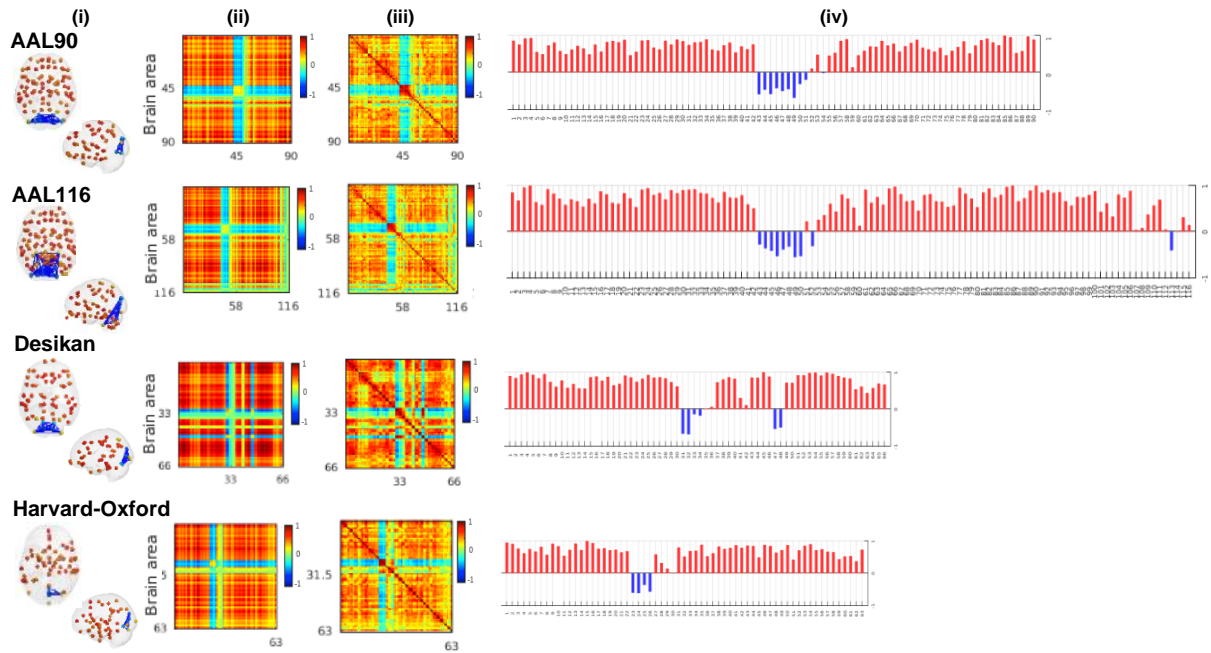
Figure 4.15. Occipital state obtained with the k-means clustering algorithm (state 3, *k* = 12), for the AAL90, AAL116, Desikan and Harvard-Oxford atlases and the PC method. This dFC state is represented by its $V_c$: **(i)** as a network in the AAL90 cortical space (axial slice), in which the elements of $V_c$ are placed at the center of gravity of the respective brain region, shaped as spheres colored according to their sign (red to yellow spheres represent positive elements from 1 to 0, cyan to dark blue spheres represent negative elements from 0 to -1), and areas with $V_c \leq 0.1$ are linked with dark blue edges; **(ii)** by the outer product $V_c V_c^T$; and **(iv)** as a bar plot displaying the projection of the BOLD phase in each brain region into $V_c$. This dFC state is also characterised by its **(iii)** dFC matrix.

## 4.4.1. Correlation of dFC states with RSNs

By analysing Figure 4.13., it is interesting to notice the effect of distinct brain parcellation schemes, with different ROIs and cortical resolutions, in the ability to obtain separated reference RSNs.

In addition to the VN, results suggest that the SMN and DMN are the only Yeo RSNs identified separately across the studied atlases. Furthermore, the VAN, which can be identified independently in the dFC states obtained with the AAL90, AAL116 and Harvard-Oxford atlases, appears intermingled with the SMN in the repertoire obtained with the Desikan atlas. In contrast, the results obtained with the Desikan atlas are the only ones where the FPN can be detected separately, without other significant correlations with Yeo RSNs in the same state. Regarding the DAN, it appears together with the FPN in the AAL90 atlas, and with VAN, SMN and FPN in the AAL116 atlas, but it can not be detected separately in any parcellation scheme. Moreover, the LN only appears in the AAL116 atlas.

Hence, it is possible to observe that the higher the number of ROIs considered in the parcellation scheme (better cortical resolution), the wider the number of statistically significant correlations established with Yeo RSNs: in the AAL116 atlas, all seven RSNs are detected; in the AAL90 atlas, only six RSNs are identified (the LN does not appear); in the Desikan atlas, there is a register of five RSNs (without any FC pattern significantly correlated with the DAN and LN); and, finally, in the Harvard-Oxford atlas, only 5 RSNs are identified (the DAN, LN and FPN do not appear).

The discrepancies found in the dFC states obtained with the four atlases justify per se the importance of comparing different criteria to divide the brain when assessing the FC repertoire at a group-level.

Relevant functional networks may not be detected in the results obtained with a specific parcellation scheme but may be notable with others. However, despite the differences highlighted above, the resemblances exhibited by the results obtained with the four atlases were expected due to the meaningful degree of similarity between them. As seen in Figure 2.6., the adjusted mutual information scores computed between the AAL, Desikan and Harvard-Oxford atlases ranged, approximately, from 0.5 to 0.6).

## 4.5. Comparison between groups

### 4.5.1. Migraineurs: Interictal vs. Ictal sessions

Migraine interictal and ictal sessions were compared by implementing a permutation-based paired $t$-test on the mean lifetime and probability of occurrence of the dFC states. Then, the FC patterns with statistically significant between-session differences on those temporal metrics were analysed. The $p$-values associated with the solutions obtained for the whole FC repertoire studied ($k = 3$ to $k = 15$) with the AAL90 atlas and PC method are displayed in Figure 4.16.

The red dashed line represents the standard significance threshold, $p$-value = 0.05; the green dashed line corresponds to the Bonferroni corrected significance threshold to correct for multiple comparisons by considering the number of states (independent hypotheses) compared within each partition model, $p$-value = 0.05/$k$; and the blue dashed line represents the corrected significance threshold to correct for multiple comparisons by considering all hypothesis independent across models, including the whole sample of tests performed, $p$-value = 0.05/$\Sigma k$ [89].
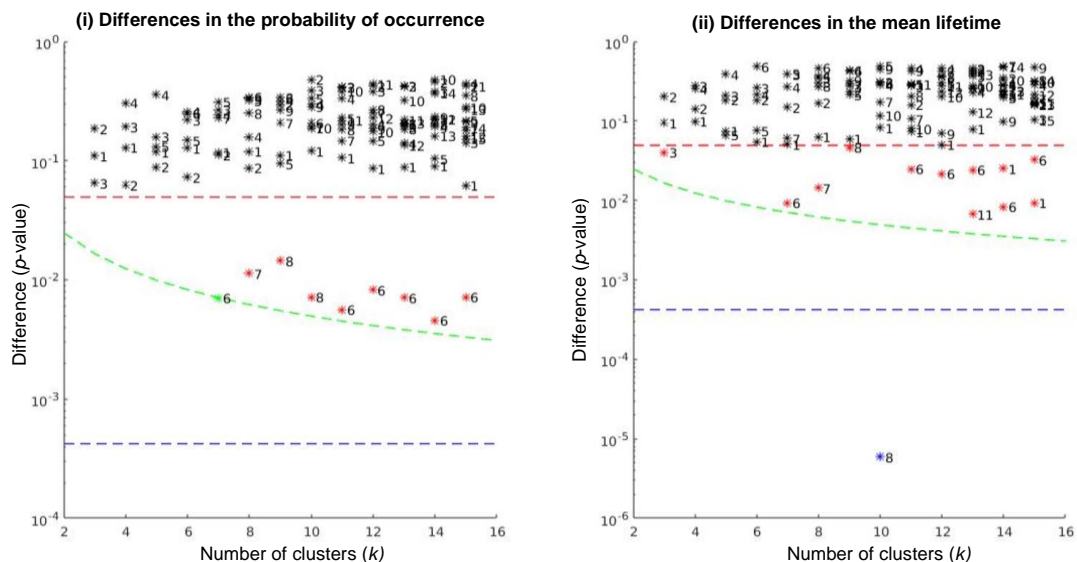


Figure 4.16. Significance of differences in the **(i)** probability of occurrence and **(ii)** mean lifetime of dFC states obtained with the AAL90 atlas and PC method, between migraine interictal and ictal sessions, as a function of $k$. The red, green and blue dashed lines represent $p$-values equal to 0.05, 0.05/$k$ and 0.05/$\Sigma k$, respectively. Thus, all dFC states noted with a black asterisk (above the red line) passed the null hypothesis, i.e., present no significant difference between sessions; the FC patterns marked with a red asterisk (above the green and below the red lines, $p$-value < 0.05, > 95 % of confidence) rejected the null hypothesis but did not pass the correction for multiple comparisons, being considered possible false positives; the states noted with a green asterisk (above the blue and below the green lines) rejected the null hypothesis with $p$-value < 0.05/$k$; and the states noted with a blue asterisk (below the blue line) rejected the null hypothesis with $p$-value < 0.05/$\Sigma k$.

Of the clustering solutions considered, most dFC states did not present any significant difference between the interictal and ictal sessions (black asterisks). Moreover, several solutions obtained for the probability of occurrence and mean lifetime were revealed to be possible false positives (red asterisks). Only two solutions survived the correction for multiple comparisons: state 6 for $k = 7$ (green asterisk, $p$-value $< 0.05/k$) and state 8 for $k = 10$ (blue asterisk, $p$-value $< 0.05/\Sigma k$), with significant between-session differences in the probability of occurrence and mean lifetime, respectively.

For the subsequent analyses, the partition model with the lowest $k$ and, simultaneously, with the solution displaying the $p$-value below the most significant threshold will be studied. For example, the chosen partition model for this atlas will be $k = 10$, since it is the shortest repertoire displaying a solution below the most significant threshold ($p$-value $< 0.05/\Sigma k$). Furthermore, the FC pattern with significant between-session differences in temporal metrics will be analysed and correlated with reference RSNs (Yeo and Smith repertoires).

### 4.5.1.1. Analysis of relevant dFC states: temporal metrics and correlation with RSNs

The partition model $k = 10$ obtained with the AAL90 atlas and PC method is displayed in Figure 4.17.
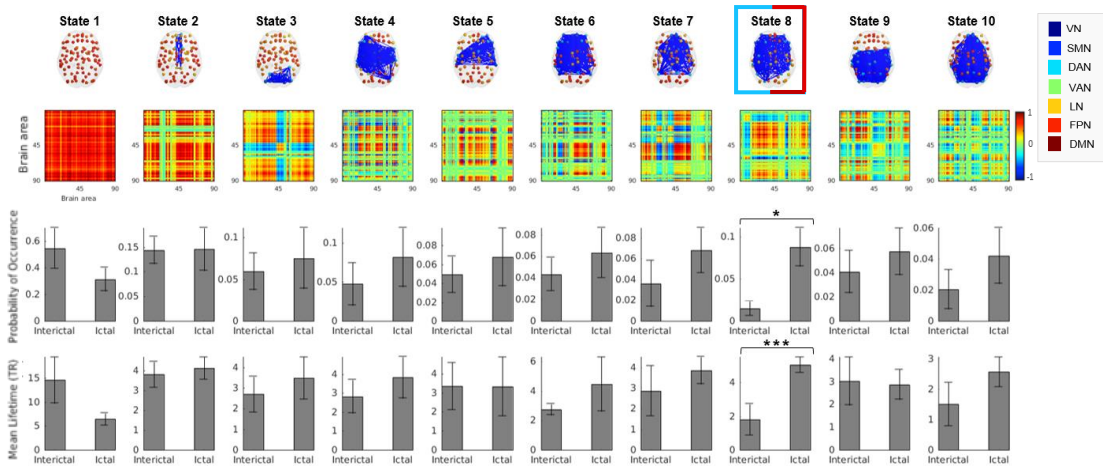


Figure 4.17. dFC states obtained with the k-means clustering algorithm ($k = 10$), displayed according to their decreasing probability of occurrence, for the AAL90 atlas and PC method. Each dFC state is represented by its $V_c$ as: a network in the AAL90 cortical space (axial slice), in which the elements of $V_c$ are placed at the center of gravity of the respective brain region, shaped as spheres coloured according to their sign (red to yellow spheres represent positive elements from 1 to 0, cyan to dark blue spheres represent negative elements from 0 to -1), and areas with $V_c \leq 0.1$ are linked with dark blue edges; and by the outer product $V_c V_c^T$. Below the representation of each state, the respective probabilities of occurrence and mean lifetimes are displayed for the migraine patients in the interictal and ictal sessions. The rectangle marks states with statistically significant between-session differences and correlation to any Yeo RSN, with the colours representing the RSN. * Significant difference before correcting for multiple comparisons ($p$-value $< 0.05$); ** Significant difference after correcting for multiple comparisons ($p$-value $< 0.05/k$); *** Significant difference after correcting for multiple comparisons ($p$-value $< 0.05/\Sigma k$).

In detail, for the partition model $k = 10$, state 8 displays a statistically significant between-session difference in the mean lifetime ($p$-value $= 5.92 * 10^{-6}$), spending longer continuous time periods in the ictal session (averaged mean lifetime ± standard error $= 5.05 ± 0.46$ TR) than in the interictal session (1.80 ± 0.92 TR). Furthermore, the frequency of this FC pattern is also significantly higher during the ictal phase (averaged probability of occurrence ± standard error $= 0.088 ± 0.023$) than in the interictal phase (0.015 ± 0.009), although this metric did not pass the correction for multiple comparisons.

In order to evaluate the correlation of state 8 with the well-established functional networks, the Pearson correlation coefficient computed between the cluster centroid vector of this dFC state with the Yeo and Smith transformed RSNs vectors is presented in Figure 4.18.
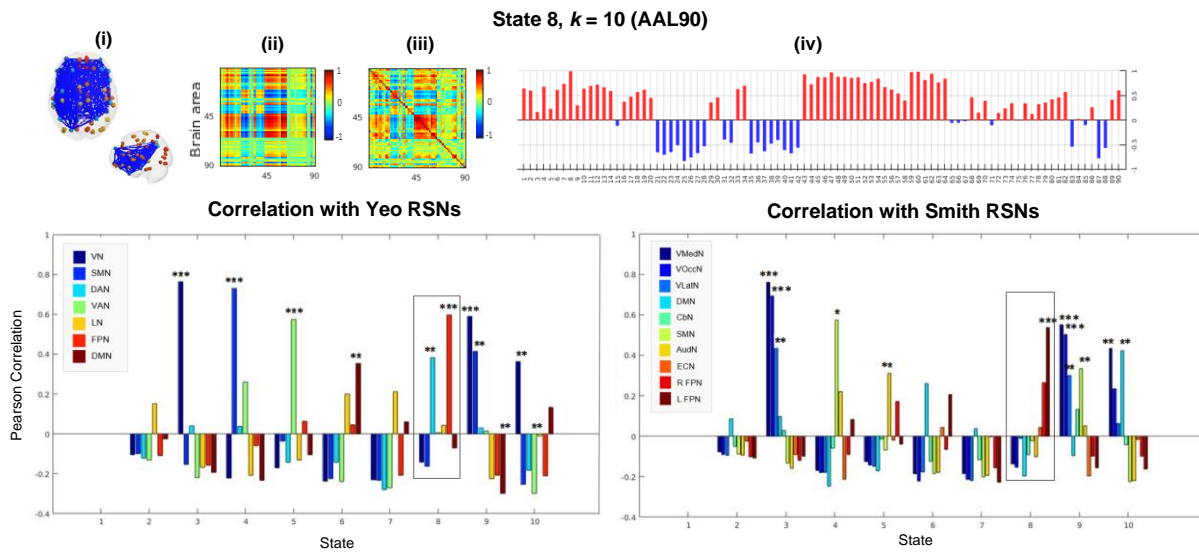


Figure 4.18. State obtained with the k-means clustering algorithm (state 8, $k = 10$), for the AAL90 atlas and PC method, and its Pearson correlation with Yeo and Smith repertoires. This dFC state is represented by its $V_c$: **(i)** as a network in the AAL90 cortical space (axial slice), in which the elements of $V_c$ are placed at the center of gravity of the respective brain region, shaped as spheres coloured according to their sign (red to yellow spheres represent positive elements from 1 to 0, cyan to dark blue spheres represent negative elements from 0 to -1), and areas with $V_c \leq 0.1$ are linked with dark blue edges; **(ii)** by the outer product $V_c V_c^T$; and **(iv)** as a bar plot displaying the projection of the BOLD phase in each brain region into $V_c$. Each dFC state is also characterised by its **(iii)** dFC matrix. **: Statistically significant correlations after correcting for the number of clusters (*p*-value < 0.05/*k*); *** Significant difference after correcting for multiple comparisons (*p*-value < 0.05/Σ*k*). VN = Visual Network; SMN = Somatomotor Network; DAN = Dorsal Attention Network; VAN = Ventral Attention Network; LN = Limbic Network; (R/L) FPN = (Right/Left) Frontoparietal Network; DMN = Default Mode Network; VMedN = Visual Medial Network; VOccN = Visual Occipital Network; VLatN = Visual Lateral Network; CbN = Cerebellar Network; AudN = Auditory Network; ECN = Executive Control Network.

By analysing Figure 4.18., it is possible to observe that the functional network detaching from the global mode in state 8 is composed of regions mainly from the frontal lobe (frontal inferior orbital and frontal superior medial gyri, gyrus rectus, olfactory cortex, frontal medial orbital cortex, and anterior and posterior cingulate cortices). However, it also presents areas from the parietal lobe (angular gyrus and precuneus cortex); temporal lobe (parahippocampal gyrus, temporal middle gyrus and temporal superior and middle poles); and subcortical regions (hippocampus, amygdala and caudate nucleus).

In terms of correlation to well-established functional templates, this FC pattern significantly overlaps with the DAN ($r = 0.38$, *p*-value = $2.02 * 10^{-4}$) and FPN ($r = 0.60$, *p*-value = $5.00 * 10^{-10}$) of Yeo repertoire, and with the left FPN ($r = 0.54$, *p*-value = $4.92 * 10^{-8}$) of Smith repertoire.

Next, to evaluate the FC strength of dFC states (how coherent paired brain regions are), especially in those revealing significant between-session differences in terms of temporal metrics, the eigenvalues of dFC matrices were averaged over the time points in which the respective FC patterns occurred in the interictal and ictal sessions, which is displayed in Figure 4.19.

Figure 4.19. reveals that the DAN/FPN state (state 8) presents significantly different (*p*-value = 0.015) mean eigenvalues between both sessions, with stronger FC during the ictal phase (mean eigenvalue of

56.16 ± 1.34) than in the interictal phase (52.28 ± 0.73), and lower eigenvalues than the global mode in both sessions. Indeed, the global mode is the most strongly connected state regardless of the phase of the migraine cycle (higher mean eigenvalues in both sessions in comparison to the remaining states), exhibiting significantly higher FC strength ($p$-value < 0.05) when occurring in the interictal session (mean eigenvalue of 70.94 ± 2.61) than in the ictal session (64.36 ± 0.88).
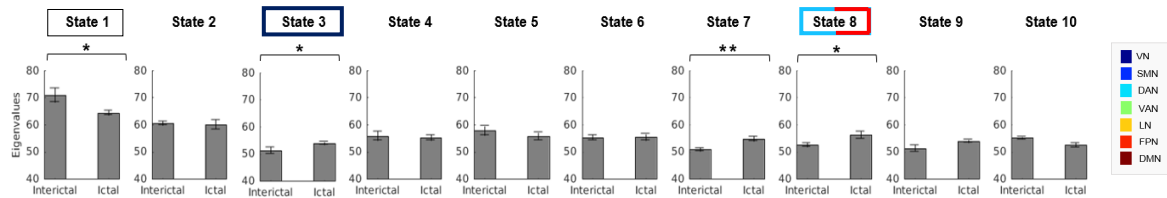


Figure 4.19. Mean eigenvalues of each dFC state obtained with the k-means clustering algorithm ($k$ = 10), for the AAL90 atlas and PC method, displayed for the interictal and ictal sessions. * Significant difference before correcting for multiple comparisons ($p$-value < 0.05); ** Significant difference after correcting for multiple comparisons ($p$-value < 0.05/$k$); *** Significant difference after correcting for multiple comparisons ($p$-value < 0.05/$\Sigma k$). The rectangle marks states with statistically significant between-group differences and correlation to any Yeo RSN, with the colors representing the RSN. The black rectangle marks the global mode.

Furthermore, state 3, which is significantly correlated with Yeo's VN and Smith's VMedN, VOccN and VLatN ($p$-value < 0.05/$\Sigma k$), and state 7, without any significant correlation to Yeo RSNs, both reveal significantly higher FC strength ($p$-values < 0.05 and 0.05/$k$, respectively) in the ictal session than in the interictal session. The VN in state 3 is composed of regions from the occipital lobe (calcarine fissure, cuneus cortex, lingual gyrus, occipital superior, middle and inferior gyri); fusiform gyrus, belonging to both occipital and temporal lobes; and parietal lobe (parietal superior gyrus).

Hence, results suggest that during the migraine attack, besides the higher mean lifetime and probability of occurrence of the DAN/FPN state, this network also presents stronger FC in comparison to the attack-free period. This observation is also valid for the VN (state 3), however, the differences in terms of mean lifetime and probability of occurrence did not present statistical significance for this atlas.

Regarding the remaining atlases, the $p$-values of the solutions with statistically significant differences in terms of the temporal metrics can be consulted in Figure D.1. of Appendix D. The partition models chosen to be analysed for each atlas followed the aforementioned criteria, being $k$ = 14 for the AAL116, $k$ = 9 for Desikan and $k$ = 13 for Harvard-Oxford. A more detailed description of the states is displayed in Figure D.2. of the same appendix.

Firstly, the DAN/FPN functional system described for the AAL90 atlas (state 8, $k$ = 10) can also be found with significant between-session differences in the results obtained with the AAL116 atlas – state 10 ($k$ = 14), significantly correlated with Yeo's DAN and FPN and Smith's left FPN ($r$ = 0.28, 0.57 and 0.52, respectively) – and the Harvard-Oxford atlas – state 9 ($k$ = 13), significantly correlated with Yeo's DAN and FPN and Smith's right and left FPN ($r$ = 0.54, 0.47, 0.56 and 0.64, respectively). Regarding the Desikan atlas, state 9 ($k$ = 9) overlaps with Yeo's FPN and Smith's left FPN ($r$ = 0.46 and 0.46, respectively). One should note that all the correlations with RSNs passed the significance threshold corrected for the whole sample of tests performed ($p$-value < 0.05/$\Sigma k$).

Similar to the AAL90 atlas, the DAN/FPN state presents significantly higher mean lifetime ($p$-value < 0.05/$\Sigma k$), probability of occurrence ($p$-value < 0.05) and FC strength ($p$-value < 0.05) in the ictal session

than in the interictal session for the AAL116 and Harvard-Oxford atlases. For the Desikan atlas, the FPN occurs in significantly longer continuous time periods ($p$-value < 0.05/$k$), with a higher probability ($p$-value < 0.05/$\Sigma k$) and stronger FC ($p$-value < 0.05) in the ictal session than in the interictal session.

Also, besides the DAN/FPN, other states correlated to well-established RSNs ($p$-value < 0.05/$\Sigma k$) presented significant between-session differences for the partition models studied before.

The global mode revealed a mean lifetime (AAL116 and Desikan, $p$-value < 0.05), probability of occurrence (Desikan, $p$-value < 0.05) and FC strength (Harvard-Oxford atlas, $p$-value < 0.05/$k$) significantly higher in the interictal session when compared to the ictal session.

Regarding the VN, state 5 (Yeo's VN) and state 8 (Yeo's VN and Smith's VMedN, VOccN and VLatN) obtained with the AAL116 and state 5 (Yeo's VN and Smith's VMedN) obtained with the Harvard-Oxford revealed significantly higher mean lifetime and probability of occurrence ($p$-value < 0.05) in the ictal session than in the interictal session.

Finally, with respect to the SMN, state 8 (Yeo's SMN and Smith's SMN and AudN) obtained with Desikan showed significantly higher mean lifetime and probability of occurrence ($p$-value < 0.05) and FC strength ($p$-value < 0.05/$\Sigma k$) for the ictal session than the interictal session. This state is composed of regions from the frontal lobe (precentral gyrus, orbitofrontal medial cortex, anterior cingulate cortex rostral, posterior cingulate cortex); parietal lobe (postcentral gyrus); paracentral gyrus, belonging to both parietal and frontal lobes; and temporal lobe (temporal superior gyrus, banks superior temporal sulcus, entorhinal cortex, temporal pole and temporal transverse cortex).

The VN and SMN, which displayed statistically significant between-session differences across atlases, are displayed in Figure 4.20. The first one was obtained with the AAL90 atlas, and the second one was yielded with Desikan.
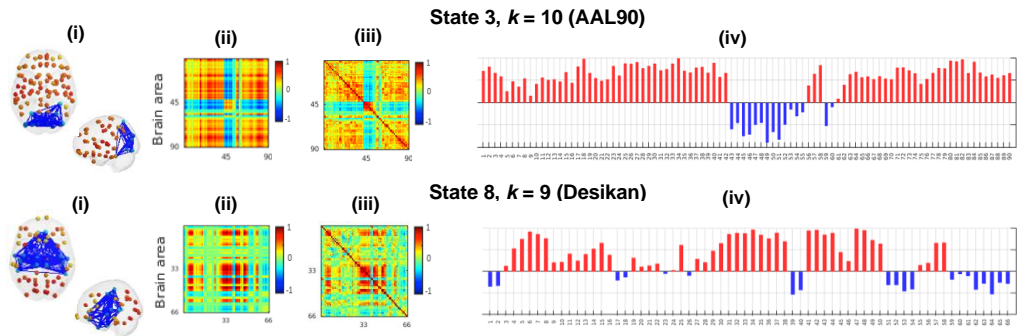


Figure 4.20. States obtained with the k-means clustering algorithm for the AAL90 (state 3, $k$ = 10) and Desikan (state 8, $k$ = 9) atlases and PC method, represented by their $V_c$: **(i)** as a network in the atlas cortical space (axial slice), in which the elements of $V_c$ are placed at the center of gravity of the respective brain region, shaped as spheres colored according to their sign (red to yellow spheres represent positive elements from 1 to 0, cyan to dark blue spheres represent negative elements from 0 to -1), and areas with $V_c \leq 0.1$ are linked with dark blue edges; **(ii)** by the outer product $V_c V_c^T$; and **(iv)** as a bar plot displaying the projection of the BOLD phase in each brain region into $V_c$. Each dFC state is also characterised by its **(iii)** dFC matrix.

The switching profile of the dFC states characteristic of each session, with the probabilities of switching from a given dFC state to another, was also obtained for $k$ = 10 with the AAL90 atlas. However, none of the transition probabilities revealed statistically significant between-session differences surviving the thresholds for multiple comparisons. The results can be found in Figure D.3.

Next, a permutation-based paired $t$-test was also applied on the mean lifetime and probability of occurrence of the dFC states obtained with the AAL90 atlas and the SW of 25 TR instead of the PC, in order to evaluate the impact of changing the method to estimate dFC in the between-session differences (see Figure D.1. and Figure D.2. of Appendix D).

The results obtained with the SW reveal more solutions surviving the threshold corrected for the whole sample of tests performed ($p$-value $< 0.05/\Sigma k$) compared to the results obtained with the PC, especially regarding the mean lifetimes. However, most of these states poorly resemble well-established RSNs from Yeo and Smith repertoires, contrary to those obtained from the PC method. This observation reinforces, once again, the reduced specificity of the SW in detecting functional networks.

Regarding the solutions showing statistically significant between-session differences and correlation with Yeo and Smith RSNs ($p$-value $< 0.05/k$), state 2 for $k = 3$ (significantly correlated with Yeo's and Smith's SMN) reveals significantly higher mean lifetime ($p$-value $< 0.05/\Sigma k$) in the ictal session; state 9 for $k = 12$ (Yeo's DAN and FPN and Smith's left FPN) presents significantly higher mean lifetime ($p$-value $< 0.05$) in the ictal session; and state 6 for $k = 15$ (Yeo's and Smith's SMN) shows significantly higher mean lifetime ($p$-value $< 0.05$) and probability of occurrence ($p$-value $< 0.05$) in the ictal session, all compared to the interictal session. These observations suggest consistency across the PC and the SW methods.

### 4.5.2. Migraineurs vs. Controls

Regarding migraine patients scanned in the interictal phase and healthy controls, the groups were compared by applying a permutation-based unpaired $t$-test on the temporal metrics of the dFC states. The *p-values* associated with the solutions obtained for the whole FC repertoire ($k = 3$ to $k = 15$) with the AAL90 atlas and PC method are displayed in Figure 4.21.
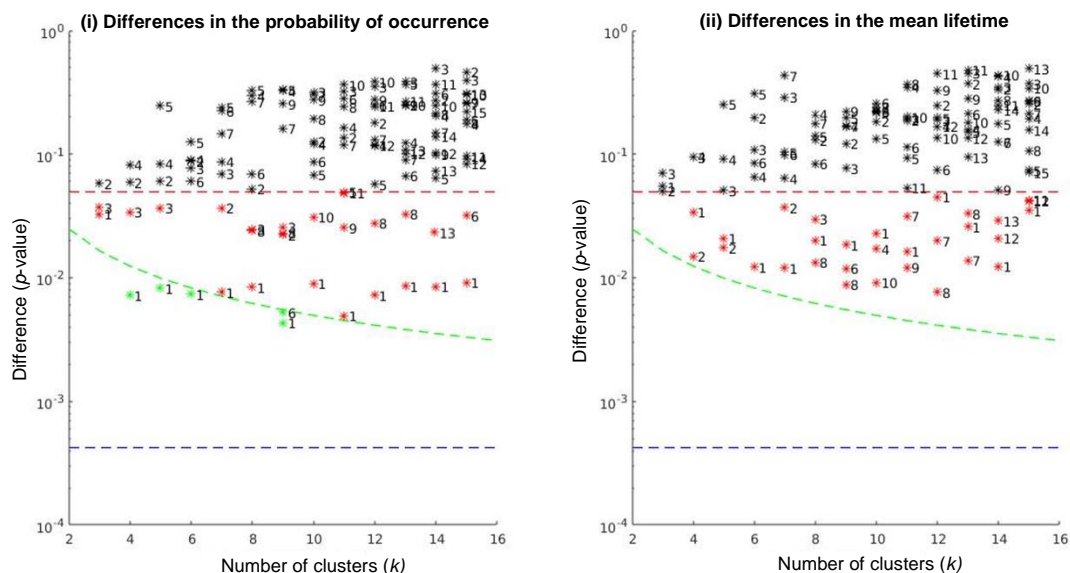


Figure 4.21. Significance of between-group differences in the **(i)** probability of occurrence and **(ii)** mean lifetime of each dFC state, obtained with the AAL90 atlas and PC method, between migraine patients scanned in the interictal phase and healthy controls, as a function of $k$. The red, green and blue dashed lines represent $p$-values equal to 0.05, $0.05/k$ and $0.05/\Sigma k$, respectively.

Results in Figure 4.21. show that the global mode displays statistically significant between-group differences in the probability of occurrence and mean lifetime from $k = 4$ to $k = 15$ ($0.05/\Sigma k < p$-value $<$

< 0.05) between migraine patients scanned in the interictal phase and healthy controls. In this case, the partition model chosen to be analysed is k = 4, following the aforementioned criteria.

#### 4.5.2.1. Analysis of relevant dFC states: temporal metrics and correlation with RSNs

Figure 4.22. displays the clustering solution $k = 4$ in more detail, including the states' temporal properties and mean eigenvalues for both patients and controls.
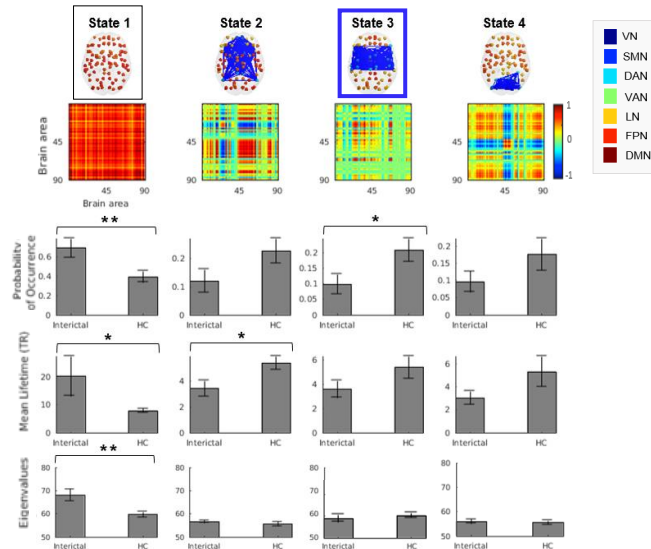


Figure 4.22. dFC states obtained with the k-means clustering algorithm ($k = 4$), displayed according to their decreasing probability of occurrence, for the AAL90 atlas and PC method. Each dFC state is represented by its $V_c$ as: a network in the AAL90 cortical space (axial slice), in which the elements of $V_c$ are placed at the center of gravity of the respective brain region, shaped as spheres colored according to their sign (red to yellow spheres represent positive elements from 1 to 0, cyan to dark blue spheres represent negative elements from 0 to -1), and areas with $V_c \leq 0.1$ are linked with dark blue edges; and by the outer product $V_c V_c^T$. Below the representation of each state, the respective probabilities of occurrence, mean lifetimes and mean eigenvalues are displayed for the migraine patients in the interictal phase and healthy controls. The rectangle marks states with statistically significant between-group differences and correlation to any Yeo RSN, with the colors representing the RSN. The black rectangle marks the global mode. * Significant difference before correcting for multiple comparisons (*p*-value < 0.05); ** Significant diffence after correcting for multiple comparisons (*p*-value < 0.05/*k*); *** Significant difference after correcting for multiple comparisons (*p*-value < 0.05/Σ*k*). HC = Healthy Controls.

For $k = 4$, the global mode reveals a significantly higher probability of occurrence (*p*-value = = 7.23 ∗ 10$^{-3}$), mean lifetime (*p*-value = 3.40 ∗ 10$^{-2}$) and FC strength (*p*-value = 1.40 ∗ 10$^{-3}$) in migraine patients in the interictal session compared to healthy controls. This state occurs with a probability of 0.687 ± 0.099, mean lifetime of 20.08 ± 7.08 TR, and FC strength of 67.91 ± 2.50 for the migraine group, and probability of 0.391 ± 0.057, mean lifetime of 7.88 ± 0.72 TR, and FC strength of 59.63 ± 1.22 for the control group. As expected, and similarly to the behaviour observed when comparing the two phases of the migraine cycle (section 4.5.1.1.), the global coherence state is the only FC pattern with a higher probability of occurrence (and in this case, higher mean lifetime) in migraineurs scanned in the interictal phase compared to control group. Thus, these findings suggest that, during the interictal phase, patients spend longer continuous time periods in the global mode and present a lower probability of occurring in the remaining synchronisation patterns.

Other patterns that show significant between-group differences in this partition model, although not surviving multiple comparisons correction, are states 2 and 3, in which healthy controls reveal higher

mean lifetime and probability of occurrence than migraineurs, respectively. State 2 does not present any significant correlation with well-established RSNs, being composed of regions from the frontal lobe (frontal superior medial gyrus, frontal medial orbital cortex, gyrus rectus, olfactory cortex, and anterior and posterior cingulate cortices); parietal lobe (angular gyrus); temporal lobe (parahippocampal gyrus and temporal middle pole); and subcortical regions (hippocampus and amygdala). Moreover, state 3 is significantly correlated with Yeo's SMN and Smith's SMN and AudN and exhibits a functional network composed of regions from the frontal lobe (precentral gyrus, frontal middle gyrus, frontal middle orbital gyrus, frontal inferior opercular and triangular gyri, rolandic operculum and supplementary motor area); insular cortex; parietal lobe (postcentral gyrus, parietal superior and inferior gyri and supramarginal gyrus); paracentral lobe, which is part of the parietal and frontal lobes; temporal lobe (Hechl's gyrus, temporal superior and inferior gyri); and subcortical regions (lenticular nuclei putamen and pallidum). These functional subsystems are more weakly connected than the global mode.

Regarding the remaining atlases, the $p$-values of the solutions with significant differences in terms of the temporal metrics can be consulted in Figure D.4. of Appendix D. The partition models chosen to be analysed for each atlas following the aforementioned criteria were $k = 5$ for the AAL116, $k = 5$ for Desikan and $k = 4$ for Harvard-Oxford. A more detailed description of the states is displayed in Figure D.5. of the same appendix.

The significant differences found in the global mode obtained with the AAL90 atlas can also be verified with statistical significance in the repertoires obtained with the remaining parcellation schemes.

Furthermore, other states present statistically significant between-group differences and significant overlap with Yeo and Smith RSNs ($p$-value $< 0.05/ \Sigma k$). In the results obtained with the AAL116 atlas, state 5 (significantly correlated with Yeo's SMN and Smith's SMN and AudN) revealed significantly higher mean lifetime (p-value $< 0.05$) and probability of occurrence (p-value $< 0.05/\Sigma k$) in migraineurs scanned in the interictal phase compared to controls. Regarding the FC repertoire obtained with the Harvard-Oxford atlas, state 4 (Yeo's VN and Smith's VMedN and VOccN) displayed significantly higher mean lifetime (p-value $< 0.05$) and probability of occurrence (p-value $< 0.05$) for patients than controls.

Although the partition models were studied following the criterium of lowest $k$ and $p$-value below the most significant threshold, to observe the behaviour of the DAN/FPN network found in section 4.5.1.1. in the present comparison, the partition model $k = 14$ obtained with the AAL90 was analysed (Figure D.4. of Appendix D). For this clustering solution, it was found that state 13, which significantly ($p$-value $< 0.05/\Sigma k$) overlaps with Yeo's DAN and FPN and Smith's right and left FPN, exhibits lower mean lifetime and probability of occurrence ($p$-value $< 0.05$) in the patients group than in controls.

Regarding the switching profile of the dFC states characteristic of patient and control groups obtained for $k = 4$ with the AAL90 atlas (consult Figure D.6.), no statistically significant between-group differences surviving the thresholds for multiple comparisons were registered. However, it is interesting to note that the only transition in which migraineurs in the interictal phase present a significantly higher ($p$-value $<$ $0.05$) transition probability than controls is from state 4 to the global mode, which reinforces the tendency of patients to align the BOLD phases towards the main orientation determined by the leading eigenvector and switch to the global mode in this phase of the migraine cycle.

### 4.5.3. Interpretation of results and association with migraine pathophysiology

A summary of the results obtained in the statistical comparisons across atlases and with the PC method between migraineurs in the interictal and ictal phases and between migraineurs in the interictal phase and healthy controls is displayed in Table 4.2. The stronger statistical significance (lower *p*-value) associated with the results across atlases is also registered on the table. Also, the labels of the AAL atlas were chosen to describe the composition of the RSN detaching from the global mode.

Table 4.2. Summary of the results obtained with the statistical comparisons between the migraine interictal session vs. ictal session and migraine interictal session vs. healthy controls.

| FC pattern | Composition of the RSN detaching from global mode | Main findings |
|---|---|---|
| **Global mode** | – | Interictal vs. Ictal<br>↑ LT*, PO*, FC**<br>Interictal vs. HC<br>↑ LT*, PO**, FC*** |
| **DAN/FPN** | F lobe (FIOG, IOG, OlfC, FSMedG, FMedOC, GRec, ACC, PCC); Par lobe (AnG, PrecunC); T lobe (ParaHiCG, TMG, TS and TM poles); SC regions (HiC, Amg, CdN) (AAL90) | Interictal vs. Ictal<br>↓ LT***, PO*, FC*<br>Interictal vs. HC<br>↓ LT*, PO* |
| **VN** | Occ lobe (CalFis, CunC, LinG, OccSG, OccMG, OccIG); Occ/T lobe (FusG); Par lobe (ParSG) (AAL90) | Interictal vs. Ictal<br>↓ LT*, PO*, FC*<br>Interictal vs. HC<br>↓ LT*, PO* |
| **SMN/AudN** | F lobe (PreCeG, FMG, FMOG, FIOpG, FITriG, RolOp, SuppMoA); Par/T lobes (InsC); Par lobe (PostCeG, ParSG, ParIG, SupG); Par/F lobes (ParaCe lobe); T lobe (Hechl's G, TSG, TIG); SC regions (LentNPut, LentNPal) (AAL116) | Interictal vs. Ictal<br>↓ LT*, PO*, FC***<br>Interictal vs. HC<br>↓ LT*, PO*** |

**Abbreviations: A** = Anterior; **Amg** = Amygdala; **An** = Angular; **C** = Cortex; **CalFis** = Calcarine Fissure; **CC** = Cingulate Cortex; **Cd(N)** = Caudate (Nucleus); **Ce** = Central; **Cun** = Cuneus; **F** = Frontal; **FC** = Functional connectivity; **Fus** = Fusiform; **G** = Gyrus; **HC** = Healthy Controls; **HiC** = Hippocampus; **I** = Inferior; **Ins** = Insular; **L** = Left; **LentN** = Lentiform Nucleus; **Lin** = Lingual; **LT** = Mean Lifetime; **M** = Middle; **Med** = Medial; **O** = Orbital; **Olf** = Olfactory; **Occ** = Occipital; **Op** = Opercular; **P** = Posterior; **Par** = Parietal; **Precun** = Precuneus; **Pal** = Pallidum; **PO** = Probability of occurrence; **Put** = Putamen; **Rec** = Rectus; **RolOp** = Rolandic Operculum; **S** = Superior; **SC** = Subcortical; **Sup** = Supramarginal; **SuppMoA** = Supplementary Motor Area; **T** = Temporal; **Tri** = Triangular; ↑/↓ = Increased/Decreased; * Significant difference before correcting for multiple comparisons ($p$-value < 0.05); ** Significant difference after correcting for multiple comparisons ($p$-value < 0.05/k); *** Significant difference after correcting for multiple comparisons ($p$-value < 0.05/Σk).

Over the past years, neuroimaging studies have revealed alterations in the functional state of migraineurs' brain compared to the normal brain condition [121]. One of the main goals of this work was to identify those FC variations between migraine patients scanned in the interictal and ictal phases, and between migraineurs and healthy controls, which could potentially constitute clinical neuroimaging biomarkers helpful to predict migraine attacks and more accurately diagnose and understand the disorder pathophysiology.

Neuroimaging studies reveal that the pathological alteration of the migraine brain involves the sensitivity of FC to plastic and developmental changes in the functional architecture. This sensitivity may lead to the adaptation of cortical networks and reshape of functional connections to altered cognitive and emotional demands, such as chronic pain [122]. Indeed, converging evidence suggests that the increased nociceptive synaptic transmission derived from recurring headaches involves a survival pain experience that demands attention and is intimately associated with learning. Thus, the unconditioned pain stimuli may bring cognitive and sensory processing-related regions to a heightened state [123].

### 4.5.3.1. DAN/FPN

The DAN and FPN play an essential role in cognitive and executive processes, involving goal-directed attention, working memory, stimulus processing and perception-somesthesis-pain (consult Table 2.1.) [62][121]. Hence, the study of dFC changes in these brain networks may provide indirect information about brain cognitive and executive integrity.

The present work results suggest that migraineurs spend longer continuous time periods, with a higher probability of occurrence and more strongly coherent brain regions in a state composed of the DAN and FPN during the ictal phase compared to the interictal phase. The temporal metrics of this FC pattern are also higher for controls than for migraine patients in the interictal phase.

To the best of our knowledge, comparisons throughout the migraine cycle and between migraineurs and healthy controls in terms of dynamics of FC states have not been performed so far. In contrast, FC findings have already been reported in several studies comparing these groups, although lacking consistency and reproducibility ( Table *2.2.* and Table *2.3.*).

Regarding the DAN, Niddam et al. [124] suggest an increased sFC between the DAN and the orbital, rectal, fusiform and parahippocampal gyri, and middle temporal and occipital gyri in migraine patients scanned in the interictal phase compared to controls.

With respect to the FPN, Russo et al. [125] report a decrease in the sFC of the FPN with the middle frontal gyrus and dorsal anterior cingulate cortex, Li et al. [126] suggest a decrease in the sFC of the right FPN with the precuneus and Lee and colleagues [81] point to a decrease in the dFC of FPN, all during the migraine interictal phase compared to controls.  In contrast, findings from Xue and colleagues [127] report an increased sFC within the frontoparietal central executive network (FPCEN), more precisely in the left inferior frontal gyrus for the left FPCEN and right middle frontal gyrus for the right FPCEN, and an increased sFC between the right FPCEN and the anterior insula in migraine patients scanned in the interictal phase compared to controls.

Regarding the comparison between migraine interictal and ictal phases, literature is scarce, and as far as we are aware no statistically significant results have been published.

Converging evidence has suggested that pain and cognition systems are partially overlapped and share resources. Indeed, the "pain-cognition interactions" consist of connections between brain regions with altered activity involved in pain processing and modulation, namely amygdala, anterior cingulate cortex, middle prefrontal cortex (affective components of pain) and S1, S2, and insula (sensory components of pain), and areas belonging to the FPN that act on the cognitive control of pain (ventrolateral and dorsolateral cortices and parietal gyrus). Some of these interactions may begin before the migraine attack but are more prevalent during the ictal phase [5][24][127].

Two main mechanisms have been hypothesized regarding the functioning of pain-cognition interactions during the attack. When simultaneously activated, pain and cognition systems may compete for resources. In those conditions, whereas healthy individuals show a mildly reduced brain activity in response to acute pain, and pain has a low ability to affect the performance of cognitive systems, migraineurs reveal a decreased cognitive task-related brain activity in response to painful stimulation [24]. This decrease can be explained by a "self-compensatory adaptation response" driven when the brain is exposed to a high sensorial load (nociceptive inputs), which induces a distraction or filtering

mechanism to guarantee a less painful experience and avoid suffering [126]. Furthermore, the sole activation of pain systems (resting-state condition) is interpreted by several authors as an "additional cognitive load" that requires focused attention and management. In that case, pain enhances activity in attention-specific networks (DAN) that share resources with cognitive-related networks (FPN) [98]. Following this reasoning, it is rational to expect that, during the attack, migraineurs spend longer continuous time periods in a goal-directed attentional and cognitive state, with a higher probability of occurrence and FC strength than in the attack-free period.

Seminowics et al. [128] describe an fMRI study that exposes healthy subjects to an attention-demanding cognitive task and painful stimulation. Interestingly, results show that participants subjected solely to the cognitive task or solely to the painful stimulation reveal alterations in an attention-specific network, including increased activity in the inferior frontal cortex, superior parietal cortex, premotor cortex, and anterior insula cortex, and decreased activity in the precuneus/posterior cingulate cortex, medial frontal cortex and inferior parietal/temporal cortex. The authors suggest that, in the presence of increased cognitive demand, the task-positive subsystem suppresses the task-negative one, ensuring a "common platform" for the pain and cognition circuits to interact. Furthermore, they propose that the same mechanism could underlie patients with chronic pain during resting-state, in which the focus would be centred on ongoing pain, operating a more active task-positive network in that condition [128]. This statement is consistent with the present findings.

### 4.5.3.2. SMN and VN

The SMN and the VN are sensory RSNs both involved in processing external stimuli [98]. The SMN plays a vital role in action-execution motor tasks and perception-somesthesis paradigms, and the VN is associated with the visual behavioural domain, namely the processing of simple, complex emotional and high-order visual stimuli [62][129]. For some partition models studied, the SMN appears intermingled with the AudN, which is also integrated into the sensory system and associated with action-execution, cognition-language, and perception-audition-speech paradigms [62].

The present work suggests that migraineurs hold the SMN for longer periods, with a higher probability of occurrence and more strongly coherent brain regions during the ictal phase than in the interictal phase. This behaviour of temporal metrics is also repeated for the VN in the ictal phase compared to the interictal phase, and for both networks in controls compared to patients in the interictal phase.

Comparing migraineurs in the interictal session with healthy controls. Zang et al. [130] suggest an increased sFC between the left S1 and right S1, anterior, superior parietal and temporal lobes, bilateral premotor cortex, inferior frontal gyrus, insula, primary motor cortex, and middle occipital gyrus in the interictal phase. Moreover, Tu et al. [96] point to an enhanced dFC between the SMN and VN, and a decrease in the dFC of VN dFC, both in the interictal group compared to the control group.

Comparing migraine ictal and interictal sessions, Araújo [131] reports a decrease in the sFC within the SMN (somatomotor cortex), and Hougaard and colleagues [132] suggest an increase of the sFC between the visual cortex (aura-side V5) and the lower middle frontal gyrus, both for the ictal session.

One possible theory to explain the observed increased permanence and FC strength in the SMN during the ictal phase compared to attack-free periods is that the recurrent brain activation to persistent migraine attacks enhances the strength of the functional connections between brain regions involved in

nociceptive processing, or in other words, it evokes the activity of pain processing networks [97]. For that matter, besides the stronger FC, it would be plausible to speculate that patients in the ictal phase spend significantly longer periods and with a higher probability in a network involved in processing pain information (SMN). Another hypothesis to support the increased permanence of migraineurs in this synchronisation pattern during the attack is the "psychological manipulation" theory [133]. Studies have shown that pain experience is hugely influenced by attention and emotion, and several brain regions associated with attentional/cognitive and emotional processes also participate in pain processing. Thus, it has been suggested that psychological manipulation (e.g. distraction) can profoundly impact on our perception of pain, such does the emotional state: a positive state lowers the pain and a negative state increases the pain [133]. Hence, the attempt of migraineurs in the ictal phase to distract from pain and return to a normal state may justify its frequency in dFC states participating in attention/cognitive and pain processing systems such as in a normal brain condition (healthy subjects).

Furthermore, following the reasoning of Dumkrieger and colleagues [97], the communication of sensory-discriminative pain processing regions (SMN) with stimulus processing regions (VN and AudN) may be indicative of a relationship that is inherent to the migraine brain. In fact, evidence has shown that in the presence of simultaneous sensory stimulation, such as visual stimuli, and pain stimulation, both inputs are sent from posterior thalamic neurons via dural and retinalthalamocortical pathways to the cortex, which might affect the external sensory sensitivity in migraine patients: the perception of pain stimulation is amplified in the presence of visual inputs, converging in an increased pain sensation, and the saliency of visual inputs is enhanced in the presence of pain [98][134]. This could explain a higher mean lifetime, probability of occurrence and FC strength of a visual processing-related network during the ictal phase of the migraine cycle compared to the interictal phase.

Additionally, previous migraine studies have reported associations between enhanced sensitivity to sensory inputs and hyperactivation in brain regions involved in their processing [135]. For example, migraine patients reporting hypersensitivity to light during the attack revealed photoresponsive areas in the visual cortex and increased BOLD response in the primary visual cortex and high-order visual areas [135]. In the present study, four of the five participants scanned in the ictal phase reported photophobia as a common symptom during the attack (see section 3.1.), which could also explain the higher permanence in the VN during the ictal phase when compared to the interictal phase.

It is important to be noted that the previously mentioned functional subsystems deviating from the global mode with higher temporal metrics in the ictal session than in the interictal session also comprise areas directly involved in pain processing, such as the anterior cingulate cortex, frontal medial orbital cortex, supplementary motor area, amygdala and insula. Indeed, neuroimaging studies suggest that increased activity in regions belonging to the pain matrix (namely in the S1, S2, prefrontal cortex, thalamus, basal ganglia, anterior cingulate cortex, supplementary motor area, amygdala, and insula) may be one of the possible factors that drive pain sensation [101].

### 4.5.3.3. The global mode

Results of the present work reveal that migraine patients scanned in the interictal phase spend longer continuous time periods in the global mode of BOLD signal fluctuation with a higher probability and FC strength compared to the ictal phase and healthy controls, presenting less tendency to occur in other

functional subsystems. Therefore, interestingly, migraineurs reveal a more similar behaviour to the healthy controls during the attack than in the attack-free period. This effect might be associated with the habituating response deficit characteristic of migraine patients in this phase of the cycle.

The habituation effect is proposed to be a cortical mechanism of protection against sensory overload, consisting of a decreased response to repeated stimuli (see section 2.1.1.). In patients with migraines, the repetition of sensory (visual, auditory, olfactory, somatosensitive, and nociceptive) inputs leads, on the contrary, to a successive intensification of the response with each repetition of the stimuli, which requires a higher energy demand [24][28]. This deficit contributes to the cortical hyperexcitability and vulnerability of sensory signals in migraine.

Coppola et al. [28] report that, during the days preceding the migraine attack (interictal phase), the habituation deficit reaches its maximum, with an exaggerated habituation decrease to sensory and stress overload accompanied by increased energy demand, lower thalamo-cortical activity and thalamic control. The decreased cortical activity and increased energy demand required by migraineurs in this phase of the cycle could explain its permanence in a strongly coherent state (which reflects an increased power and connectome energy [83]), and its lower probability to occur in other functional subsystems detaching from the global BOLD phase coherence (attractor states or energy landscapes characterised by local energy minima [136]) compared to the ictal phase or healthy subjects.

Furthermore, sequential recordings show that, within the interval of 12 hours to 24 hours that precede the attack (preictal phase), and with the appearance of the premonitory symptoms, the electrocortical patterns and energy demand tend to normalize, such as the habituation response. During the attack (ictal phase), this normalization is even more notable, so a higher tendency of migraineurs to occur in functional subsystems deviated from the global coherence state compared to the interictal period could be expected. Indeed, this is verified in the present work, since overall migraineurs present a higher mean lifetime and probability of occurrence in dFC states misaligned from the global mode in the ictal phase compared to the interictal phase (and in controls compared to migraineurs in the interictal phase).

Approximately one or two days after the attack (postictal phase), the electrocortical patterns tend to destabilize again, with the disruption of thalamo-cortical loops between the sensory cortex and the thalamus, the increased energy demand and the deficit in the habituation response (Figure 4.23.).
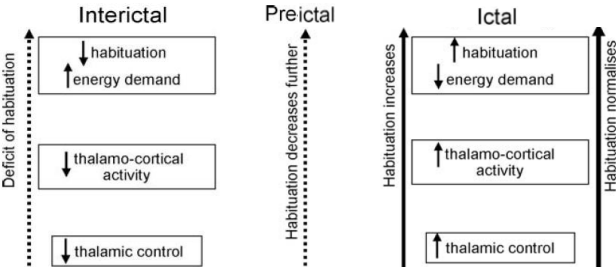


Figure 4.23. Schematic representation of changes in the habituation response, energy demands and thalamo-cortical circuits throughout the migraine cycle (interictal, preictal and ictal phases). Figure extracted from Coppola et al. [28].

Therefore, these results suggest that the migraine cycle might be characterised by an increased permanence in the global mode during the interictal phase due to the habituation response deficit and an increased probability to occur in attentional/cognitive and stimulus processing-related functional networks during the attack.

# Chapter 5

# Conclusion

*This chapter highlights the main conclusions of the present dissertation. Additionally, section 5.1. points out a few limitations and suggestions for future work.*

The main goal of the present dissertation was to study dFC in the migraine brain, which is still a novel field in the literature, and compare the temporal properties and FC strength of the recurrent dFC states between migraine patients scanned in the interictal and the ictal sessions, and between patients scanned in the interictal phase and healthy controls, in order to infer the relation of these alterations to the disorder mechanisms and the possibility of them constituting neuroimaging biomarkers to predict migraine progression or response to treatment.

A number of tests were first performed on the migraine interictal dataset to investigate the impact of different methodological options in the LEiDA approach. In particular, we verified that the proportion of variance explained by the leading eigenvector for the PC and SW methods with the AAL90 atlas was generally over 50 % and hence that the leading eigenvectors of the dFC matrices serve effectively to characterise brain activity over time by its whole-brain BOLD phase pattern, allowing for a significant reduction of the dimensionality of the data while explaining the majority of its variance.

Furthermore, the implementation of an ICA clean-up step in the preprocessing of rs-fMRI data was revealed to be important, as a dFC state potentially correlated with susceptibility artefacts appeared throughout the FC repertoire for the dataset without this denoising step. Nevertheless, this observation needs further analyses and validation, as explained in the next section.

The comparison between SW and PC revealed that, although both metrics provided similar connectivity matrices, the dFC states obtained with the k-means clustering algorithm differed between methods. The interpretation proposed for this divergence of results is that the SW fails in capturing synchronisation patterns that switch more rapidly to other functional subsystems due to the inherent temporal smoothing (increased period of fluctuations) that this method entails when computing the Pearson correlation coefficient between pairs of BOLD time courses within fixed-length windows. Thus, we observed a general increase in the mean lifetimes of dFC states in the SW compared to the PC, which was also validated for a larger (HCP) dataset, and this effect was more prominent for wider windows. Moreover, it was also found that this behaviour affects the specificity of SW to detect well-established RSNs (Yeo and Smith templates) for shorter datasets, which points to the PC as the best choice to compute dFC and model dynamic aspects of the migraine brain.

Also, the cluster timecourses and sFC analyses at a subject-level demonstrated the high inter-subject variability in the migraine interictal dataset and corroborated the idea that dFC better reflects the FC alterations of the migraine brain compared to the sFC, which looses information when averaging the connectivity time courses over time.

Regarding the application of a temporal smoothing algorithm to the dFC labels over time, it can be important in studies in which the duration of FC patterns is relevant to be controlled (for example, to ensure that dFC states last less than the faster oscillations of the BOLD signal). However, if the goal is to analyse dFC at each TR (maximal temporal resolution) and detect dFC states that can evolve, at least, at the temporal resolution of acquisition, the application of this filter might be counter-intuitive.

Furthermore, by comparing the results across different parcellation schemes, the FC repertoires exhibited partition models with similar dFC states. However, the number of statistically significant correlations with Yeo RSNs was higher for better cortical resolutions (higher number of ROIs). Additionally, some functional subsystems were only found with specific atlases, which justified the importance of exploring several brain parcellation schemes in the analysis.

Finally, between-group comparisons revealed statistically significant altered dynamics in four specific BOLD phase patterns: the DAN/FPN system, associated with attentional/cognitive processes; the SMN, involved in pain processing; the VN, associated with visual processing; and the global mode of BOLD signal fluctuation (fully connected state). Migraine patients scanned in the ictal phase and controls revealed higher mean lifetime and probability of occurrence in the first three networks than patients in the interictal phase, and, on the contrary, patients scanned in the interictal session were revealed to spend longer continuous time periods and with a higher frequency in the global mode.

## 5.1.  Limitations and Future Work

This study presents some limitations with regards to the rs-fMRI imaging technique.

Firstly, the BOLD-fMRI signal is an indirect measure of neuronal activity due to the haemodynamic delay, and the misunderstanding of the neurovascular coupling mechanism that explains this relationship, along with its variability across subjects, hampers the homogeneity across clinical fMRI studies and is one of the most significant sources of error in their interpretation [53][64].

Secondly, rs-fMRI is particularly sensitive to multiple confounders due to the absence of any task. These confounders are hardly controlled and include alertness, cognition, fatigue, eye-opening or closing and mood. Thus, there is an additional exigence of keeping the experimental procedures constant, and the participants instructed. Future studies may include simultaneous EEG recordings (multimodal EEG-fMRI) to control for sleep, eye-opening or closing, and basic brain activity, and provide additional information regarding the relationship between the neuronal activity and the HRF [137][138].

Additionally, identifying and removing artefacts without a prior hypothesis hinders the identification of the signal derived from neuronal activity and noise. This process becomes even more challenging with the possibility of artefacts sharing spatial or spectral overlap with the functional networks [8]. Thus, despite preprocessing rs-fMRI data, the monitorisation of cardiac and respiratory fluctuations could be performed during scanning to regress these signals out of the data in the nuisance regression step.

Concerning the study population, this work includes a small sample size with a high inter-subject variability, which might limit the generalisability of the results. The most straightforward solution to validate and increase the statistical power of the present findings is to repeat the pipeline followed in this study in a larger dataset. Also, it would be interesting to reproduce the between-group comparisons throughout the migraine cycle by recruiting patients in the preictal and postictal phases and healthy controls scanned in the corresponding menstrual phase to control for hormonal variation.

Regarding the analysis, some aspects of the present study could be explored in future work.

One of them concerns the use of data-driven approaches to parcellate rs-fMRI data. The anatomical atlases used in this study ensure spatial contiguity and non-overlap of brain regions, however, they may lead to low BOLD signal homogeneity within ROIs compared to FC-based strategies and hamper the definition of brain functional characteristics in terms of large-scale brain networks [74]. Future work should explore data-driven techniques that prioritise functional homogeneity, such as the group ICA, which was not implemented in the present study due to the small cohort.

Regarding the implementation of the ICA clean-up and nuisance regression preprocessing steps, an additional analysis should be performed to clarify the influence of robust preprocessing in the specificity of detecting functional subsystems. The auto-classification of ICs should be reviewed across subjects, especially those who spent more time in the dFC frontal state or held that synchronisation pattern in specific epochs, and the occurrence of this state could be correlated with the motion parameters (time courses). Additionally, the impact of this denoising step could also be reproduced in a larger dataset to validate the present findings.

With respect to the PC method, it should be evaluated if the Hilbert transform approach is the best option for estimating the dFC matrices. The same applies to the k-means clustering algorithm to cluster dFC data. Even though this algorithm has been extensively used in the literature [83][86][111], it has also been associated with difficulties in separating clusters with different sizes and high susceptibility to outliers [11].

Furthermore, the analyses performed to compare both SW and PC methods (correlation of cluster centroid vectors between methods, correlation of dFC states with RSNs, dynamics of dFC states and subject-level assessment) could be repeated for higher $k$'s in which statistically significant between-group differences in terms of temporal metrics were identified (for example, $k = 10$). Regarding the HCP dataset, the analyses could also be reproduced for larger $k$'s and different brain parcellation schemes (AAL116, Desikan and Harvard-Oxford).

Also, the temporal metrics of dFC states at a subject-level could be correlated with individual clinical variables (e.g. mean pain intensity of the attack, hypersensitivity to sensory stimuli and cognitive evaluation).

To sum up, the results of the present dissertation extended previous findings and represent novel evidence to the literature, revealing that the dysfunction of the migraine brain may be associated with altered dynamics, especially increased mean lifetime and probability of occurrence, in attentional/cognitive and sensory processing systems during the migraine attack, and in the global mode during the attack-free phase.

Furthermore, the study of FC fluctuations over time instead of the conventional sFC analysis corroborated evidence for the dynamic nature of the migraine brain during rest and emphasised the suitability of this analysis to detect and assess the evolution of brain signals.

Hence, this work contributes to further elucidate the migraine mechanisms, and if replicated in a larger sample, may potentially point towards neuroimaging biomarkers for disease progression and response to treatment.

# Bibliography

[1]     R. Agosti, "Migraine Burden of Disease: From the Patient's Experience to a Socio-Economic View," Headache J. Head Face Pain, vol. 58, pp. 17–32, May 2018, doi: 10.1111/head.13301.

[2]     C. Abbafati et al., "Global burden of 369 diseases and injuries in 204 countries and territories, 1990–2019: a systematic analysis for the Global Burden of Disease Study 2019," Lancet, vol. 396, no. 10258, pp. 1204–1222, Oct. 2020, doi: 10.1016/S0140-6736(20)30925-9.

[3]     T. J. Steiner, L. J. Stovner, R. Jensen, D. Uluduz, and Z. Katsarava, "Migraine remains second among the world's causes of disability, and first among young women: findings from GBD2019," Journal of Headache and Pain, vol. 21, no. 1. BioMed Central Ltd, p. 137, Dec. 01, 2020, doi: 10.1186/s10194-020-01208-0.

[4]     R. Burstein, R. Noseda, and D. Borsook, "Migraine: Multiple processes, complex pathophysiology," J. Neurosci., vol. 35, no. 17, pp. 6619–6629, Apr. 2015, doi: 10.1523/JNEUROSCI.0373-15.2015.

[5]     R. Gil-Gouveia, A. G. Oliveira, and I. P. Martins, "Assessment of cognitive dysfunction during migraine attacks: a systematic review," J. Neurol. 2014 2623, vol. 262, no. 3, pp. 654–665, Dec. 2014, doi: 10.1007/S00415-014-7603-5.

[6]     T. J. Steiner, L. J. Stovner, T. Vos, R. Jensen, and Z. Katsarava, "Migraine is first cause of disability in under 50s: will health politicians now take notice?," Journal of Headache and Pain, vol. 19, no. 1. Springer-Verlag Italia s.r.l., pp. 1–4, Dec. 01, 2018, doi: 10.1186/s10194-018-0846-2.

[7]     F. Puledda, R. Messina, and P. J. Goadsby, "An update on migraine: current understanding and future directions," J. Neurol., vol. 264, no. 9, pp. 2031–2039, Sep. 2017, doi: 10.1007/s00415-017-8434-y.

[8]     J. M. Soares et al., "A Hitchhiker's guide to functional magnetic resonance imaging," Frontiers in Neuroscience, vol. 10. Frontiers Media S.A., p. 515, Nov. 01, 2016, doi: 10.3389/fnins.2016.00515.

[9]     L. H. Schulte and A. May, "Functional Neuroimaging in Migraine: Chances and Challenges," Headache, vol. 56, no. 9, pp. 1474–1481, Oct. 2016, doi: 10.1111/head.12944.

[10]    F. M. Cutrer and J. H. Smith, "Human Studies in the Pathophysiology of Migraine: Genetics and Functional Neuroimaging," Headache J. Head Face Pain, vol. 53, no. 2, pp. 401–412, Feb. 2013, doi: 10.1111/HEAD.12024.

[11]    E. A. Allen, E. Damaraju, S. M. Plis, E. B. Erhardt, T. Eichele, and V. D. Calhoun, "Tracking whole-brain connectivity dynamics in the resting state," Cereb. Cortex, vol. 24, no. 3, pp. 663–676, Mar. 2014, doi: 10.1093/cercor/bhs352.

[12]    L. Kros, C. A. Angueyra Aristizábal, and K. Khodakhah, "Cerebellar involvement in migraine," Cephalalgia, vol. 38, no. 11. SAGE Publications Ltd, pp. 1782–1791, Oct. 01, 2018, doi: 10.1177/0333102417752120.

[13]    D. W. Dodick, "A Phase-by-Phase Review of Migraine Pathophysiology," Headache J. Head Face Pain, vol. 58, pp. 4–16, May 2018, doi: 10.1111/head.13300.

[14]    P. J. Goadsby, P. R. Holland, M. Martins-Oliveira, J. Hoffmann, C. Schankin, and S. Akerman, "Pathophysiology of migraine: A disorder of sensory processing," Physiol. Rev., vol. 97, no. 2,

pp. 553–622, Apr. 2017, doi: 10.1152/physrev.00034.2015.

[15]    J. Olesen et al., "The International Classification of Headache Disorders, 3rd edition (beta version)," Cephalalgia, vol. 33, no. 9, pp. 629–808, Jul. 2013, doi: 10.1177/03331024134856.

[16]    A. Charles, "The pathophysiology of migraine: implications for clinical management," Lancet Neurol., vol. 17, no. 2, pp. 174–182, 2018, doi: 10.1016/S1474-4422(17)30435-0.

[17]    M. Lauritzen, J. P. Dreier, M. Fabricius, J. A. Hartings, R. Graf, and A. J. Strong, "Clinical relevance of cortical spreading depression in neurological disorders: Migraine, malignant stroke, subarachnoid and intracranial hemorrhage, and traumatic brain injury," Journal of Cerebral Blood Flow and Metabolism, vol. 31, no. 1. SAGE Publications, pp. 17–35, Jan. 2011, doi: 10.1038/jcbfm.2010.191.

[18]    P. J. Goadsby, R. B. Lipton, and M. D. Ferrari, "Migraine - Current Understanding and Treatment," N. Engl. J. Med., vol. 346, no. 4, pp. 257–270, Jan. 2002, doi: 10.1056/nejmra01091.

[19]    P. Martelletti et al., "My Migraine Voice survey: A global study of disease burden among individuals with migraine for whom preventive treatments have failed," J. Headache Pain, vol. 19, no. 1, Nov. 2018, doi: 10.1186/s10194-018-0946-z.

[20]    S. Evers et al., "EFNS guideline on the drug treatment of migraine - Revised report of an EFNS task force," European Journal of Neurology, vol. 16, no. 9. John Wiley & Sons, Ltd, pp. 968–981, Sep. 01, 2009, doi: 10.1111/j.1468-1331.2009.02748.x.

[21]    J. J. Y. Ong and M. de Felice, "Migraine Treatment: Current Acute Medications and Their Potential Mechanisms of Action," Neurotherapeutics, vol. 15, no. 2, pp. 1–17, Dec. 2017, doi: 10.1007/s13311-017-0592-1.

[22]    K. P. Peng and A. May, "Migraine understood as a sensory threshold disease," Pain, vol. 160, no. 7. Lippincott Williams and Wilkins, pp. 1494–1501, Jul. 01, 2019, doi: 10.1097/j.pain.0000000000001531.

[23]    K. P. Peng and A. May, "Redefining migraine phases – a suggestion based on clinical, physiological, and functional imaging evidence," Cephalalgia, vol. 40, no. 8, pp. 866–870, 2020, doi: 10.1177/0333102419898868.

[24]    R. Gil-Gouveia and I. P. Martins, "Cognition and Cognitive Impairment in Migraine," Curr. Pain Headache Reports 2019 2311, vol. 23, no. 11, pp. 1–10, Sep. 2019, doi: 10.1007/S11916-019-0824-7.

[25]    N. Karsan and P. J. Goadsby, "Biological insights from the premonitory symptoms of migraine," Nature Reviews Neurology, vol. 14, no. 12. Nature Publishing Group, pp. 699–710, Dec. 01, 2018, doi: 10.1038/s41582-018-0098-4.

[26]    M. B. Vincent and N. Hadjikhani, "Migraine aura and related phenomena: Beyond scotomata and scintillations," Cephalalgia, vol. 27, no. 12, pp. 1368–1377, Dec. 2007, doi: 10.1111/j.1468-2982.2007.01388.x.

[27]    N. J. Giffin, R. B. Lipton, S. D. Silberstein, J. Olesen, and P. J. Goadsby, "The migraine postdrome," Neurology, vol. 87, no. 3, pp. 309–313, Jul. 2016, doi: 10.1212/WNL.00000002789.

[28]    G. Coppola, F. Pierelli, and J. Schoenen, "Habituation and migraine," Neurobiol. Learn. Mem., vol. 92, no. 2, pp. 249–259, Sep. 2009, doi: 10.1016/J.NLM.2008.07.006.

[29]    J. Hoffmann, S. M. Baca, and S. Akerman, "Neurovascular mechanisms of migraine and cluster headache," Journal of Cerebral Blood Flow and Metabolism, vol. 39, no. 4. SAGE Publications Ltd, pp. 573–594, Apr. 01, 2019, doi: 10.1177/0271678X17733655.

[30]    A. A. Parsons and P. J. L. M. Strijbos, "The neuronal versus vascular hypothesis of migraine and cortical spreading depression," Current Opinion in Pharmacology, vol. 3, no. 1. Elsevier, pp. 73–77, Feb. 01, 2003, doi: 10.1016/S1471-4892(02)00016-4.

[31]    J. R. Graham and H. G. Wolff, "Mechanism of migraine headache and action of ergotamine tartrate," Arch. Neurol. Psychiatry, vol. 39, no. 4, pp. 737–763, Apr. 1938, doi: 10.1001/archneurpsyc.1938.02270040093005.

[32] T. J. Schwedt and D. W. Dodick, "Advanced neuroimaging of migraine," Lancet Neurol., vol. 8, no. 6, pp. 560–568, Jun. 2009, doi: 10.1016/S1474-4422(09)70107-3.

[33] D. Andress-Rothrock, W. King, and J. Rothrock, "An analysis of migraine triggers in a clinic-based population," Headache, vol. 50, no. 8, pp. 1366–1370, 2010, doi: 10.1111/j.1526-4610.2010.01753.x.

[34] L. H. Schulte and K. P. Peng, "Current understanding of premonitory networks in migraine: A window to attack generation," Cephalalgia, vol. 39, no. 13. SAGE Publications Ltd, pp. 1720–1727, Nov. 01, 2019, doi: 10.1177/0333102419883375.

[35] R. Burstein and M. Jakubowski, "Neural substrate of depression during migraine," Neurol. Sci., vol. 30, no. SUPPL. 1, pp. 27–31, May 2009, doi: 10.1007/s10072-009-0061-7.

[36] S. Akerman, P. R. Holland, and P. J. Goadsby, "Diencephalic and brainstem mechanisms in migraine," Nature Reviews Neuroscience, vol. 12, no. 10. pp. 570–584, Oct. 20, 2011, doi: 10.1038/nrn3057.

[37] R. Noseda and R. Burstein, "Migraine pathophysiology: Anatomy of the trigeminovascular pathway and associated neurological symptoms, cortical spreading depression, sensitization, and modulation of pain," Pain, vol. 154, no. SUPPL. 1, pp. 1–21, 2013, doi: 10.1016/j.pain.2013.07.021.

[38] M. Capi, L. M. Pomes, G. Andolina, M. Curto, P. Martelletti, and L. Lionetto, "Persistent post-traumatic headache and migraine: Pre-clinical comparisons," Int. J. Environ. Res. Public Health, vol. 17, no. 7, 2020, doi: 10.3390/ijerph17072585.

[39] A. May and P. J. Goadsby, "The trigeminovascular system in humans: Pathophysiologic implications for primary headache syndromes of the neural influences on the cerebral circulation," Journal of Cerebral Blood Flow and Metabolism, vol. 19, no. 2. Lippincott Williams and Wilkins, pp. 115–127, Feb. 1999, doi: 10.1097/00004647-199902000-00001.

[40] C. Bernstein and R. Burstein, "Sensitization of the trigeminovascular pathway: Perspective and implications to migraine pathophysiology," Journal of Clinical Neurology (Korea), vol. 8, no. 2. Korean Neurological Association, pp. 89–99, 2012, doi: 10.3988/jcn.2012.8.2.89.

[41] R. Noseda, V. Kainz, D. Borsook, and R. Burstein, "Neurochemical Pathways That Converge on Thalamic Trigeminovascular Neurons: Potential Substrate for Modulation of Migraine by Sleep, Food Intake, Stress and Anxiety," PLoS One, vol. 9, no. 8, p. e103929, Aug. 2014, doi: 10.1371/journal.pone.0103929.

[42] Y. Sharav and R. Benoliel, "Migraine and possible facial variants (Neurovascular orofacial pain)," in Orofacial Pain and Headache, Elsevier Ltd, 2008, pp. 193–224.

[43] A. B. Gago-Veiga, J. Vivancos, and M. Sobrado, "The premonitory phase: a crucial stage in migraine," Neurol. (English Ed., Jul. 2019, doi: 10.1016/j.nrleng.2017.09.006.

[44] D. Borsook and R. Burstein, "The enigma of the dorsolateral pons as a migraine generator," Cephalalgia, vol. 32, no. 11. NIH Public Access, pp. 803–812, Aug. 2012, doi: 10.1177/0333102412453952.

[45] M. Ashina, J. M. Hansen, T. P. Do, A. Melo-Carrillo, R. Burstein, and M. A. Moskowitz, "Migraine and the trigeminovascular system - 40 years and counting," The Lancet Neurology, vol. 18, no. 8. Lancet Publishing Group, pp. 795–804, Aug. 01, 2019, doi: 10.1016/S1474-4422(19)30185-.

[46] T. J. Schwedt, C. C. Chiang, C. D. Chong, and D. W. Dodick, "Functional MRI of migraine," The Lancet Neurology, vol. 14, no. 1. Lancet Publishing Group, pp. 81–91, Jan. 01, 2015, doi: 10.1016/S1474-4422(14)70193-0.

[47] G. H. Glover, "Overview of functional magnetic resonance imaging," Neurosurgery Clinics of North America, vol. 22, no. 2. NIH Public Access, pp. 133–139, Apr. 2011, doi: 10.1016/j.nec.2010.11.001.

[48] N. K. Logothetis and B. A. Wandell, "Interpreting the BOLD signal," Annu. Rev. Physiol., vol. 66, pp. 735–769, 2004, doi: 10.1146/annurev.physiol.66.082602.092845.

[49]   V. Kuperman, Magnetic Resonance Imaging: Physical Principles and Applications. .

[50]   S. C. Bushong and G. Clarke, Magnetic Resonance Imaging: Physical and Biological Principles.

[51]   V. P. B. Grover, J. M. Tognarelli, M. M. E. Crossey, I. J. Cox, S. D. Taylor-Robinson, and M. J. W. McPhail, "Magnetic Resonance Imaging: Principles and Techniques: Lessons for Clinicians," Journal of Clinical and Experimental Hepatology, vol. 5, no. 3. Elsevier, pp. 246–255, Sep. 01, 2015, doi: 10.1016/j.jceh.2015.08.001.

[52]   R. B. Buxton, Introduction to functional magnetic resonance imaging: Principles and techniques, vol. 9780521899956. Cambridge University Press, 2009.

[53]   R. A. Poldrack, T. Nichols, and J. Mumford, Handbook of Functional MRI Data Analysis. Cambridge University Press, 2011.

[54]   D. J. Heeger and D. Ress, "What does fMRI tell us about neuronal activity?," Nature Reviews Neuroscience, vol. 3, no. 2. Nature Publishing Group, pp. 142–151, Feb. 2002, doi: 10.1038/nrn730.

[55]   K. Setsompop, D. A. Feinberg, and J. R. Polimeni, "Rapid brain MRI acquisition techniques at ultra-high fields," NMR in Biomedicine, vol. 29, no. 9. John Wiley and Sons Ltd, pp. 1198–1221, Sep. 01, 2016, doi: 10.1002/nbm.3478.

[56]   M. P. van den Heuvel and H. E. Hulshoff Pol, "Exploring the brain network: A review on resting-state fMRI functional connectivity," European Neuropsychopharmacology, vol. 20, no. 8. Elsevier, pp. 519–534, Aug. 01, 2010, doi: 10.1016/j.euroneuro.2010.03.008.

[57]   K. A. Smitha et al., "Resting state fMRI: A review on methods in resting state connectivity analysis and resting state networks," Neuroradiology Journal, vol. 30, no. 4. SAGE Publications Inc., pp. 305–317, Aug. 01, 2017, doi: 10.1177/1971400917697342.

[58]   S. M. Smith et al., "Functional connectomics from resting-state fMRI," Trends in Cognitive Sciences, vol. 17, no. 12. Elsevier Current Trends, pp. 666–682, Dec. 01, 2013, doi: 10.1016/j.tics.2013.09.016.

[59]   B. Biswal, F. Z. Yetkin, V. M. Haughton, and J. S. Hyde, "Functional Connectivity in the Motor Cortex of Resting Human Brain Using Echo-Planar MRI," 1995.

[60]   C. Rosazza and L. Minati, "Resting-state brain networks: Literature review and clinical applications," Neurological Sciences, vol. 32, no. 5. Springer, pp. 773–785, Oct. 11, 2011, doi: 10.1007/s10072-011-0636-y.

[61]   B. T. Thomas Yeo et al., "The organization of the human cerebral cortex estimated by intrinsic functional connectivity," J. Neurophysiol., vol. 106, no. 3, pp. 1125–1165, Sep. 2011, doi: 10.1152/jn.00338.2011.

[62]   S. M. Smith et al., "Correspondence of the brain's functional architecture during activation and rest," Proc. Natl. Acad. Sci. U. S. A., vol. 106, no. 31, pp. 13040–13045, Aug. 2009, doi: 10.1073/pnas.0905267106.

[63]   C. Caballero-Gaudes and R. C. Reynolds, "Methods for cleaning the BOLD fMRI signal," Neuroimage, vol. 154, pp. 128–149, Jul. 2017, doi: 10.1016/J.NEUROIMAGE.2016.12.018.

[64]   R. T. Constable, "Challenges in fMRI and its limitations," Funct. MRI Basic Princ. Clin. Appl., pp. 75–98, 2006, doi: 10.1007/0-387-34665-1_4.

[65]   L. Griffanti et al., "ICA-based artefact removal and accelerated fMRI acquisition for improved resting state network imaging," Neuroimage, vol. 95, pp. 232–247, Jul. 2014, doi: 10.1016/j.neuroimage.2014.03.034.

[66]   C. Chang and G. H. Glover, "Time-frequency dynamics of resting-state brain connectivity measured with fMRI," Neuroimage, vol. 50, no. 1, pp. 81–98, Mar. 2010, doi: 10.1016/j.neuroimage.2009.12.011.

[67]   G. J. Thompson, "Neural and metabolic basis of dynamic resting state fMRI," Neuroimage, vol. 180, pp. 448–462, Oct. 2018, doi: 10.1016/J.NEUROIMAGE.2017.09.010.

[68]     S. B. Eickhoff, B. T. T. Yeo, and S. Genon, "Imaging-based parcellations of the human brain," Nat. Rev. Neurosci., vol. 19, no. 11, pp. 672–686, 2018, doi: 10.1038/s41583-018-0071-7.

[69]     E. Tagliazucchi, M. Siniatchkin, H. Laufs, and D. R. Chialvo, "The Voxel-Wise Functional Connectome Can Be Efficiently Derived from Co-activations in a Sparse Spatio-Temporal Point-Process," Front. Neurosci., vol. 0, no. AUG, p. 381, Aug. 2016, doi: 10.3389/FNINS.2016.00381.

[70]     L. Fan et al., "Brain parcellation driven by dynamic functional connectivity better capture intrinsic network dynamics," Hum. Brain Mapp., vol. 42, no. 5, pp. 1416–1433, Apr. 2021, doi: 10.1002/hbm.25303.

[71]     R. M. Lawrence et al., "Standardizing human brain parcellations," Sci. data, vol. 8, no. 1, p. 78, Mar. 2021, doi: 10.1038/s41597-021-00849-3.

[72]     N. Tzourio-Mazoyer et al., "Automated anatomical labeling of activations in SPM using a macroscopic anatomical parcellation of the MNI MRI single-subject brain," Neuroimage, vol. 15, no. 1, pp. 273–289, 2002, doi: 10.1006/nimg.2001.0978.

[73]     R. S. Desikan et al., "An automated labeling system for subdividing the human cerebral cortex on MRI scans into gyral based regions of interest," Neuroimage, vol. 31, no. 3, pp. 968–980, 2006, doi: 10.1016/j.neuroimage.2006.01.021.

[74]     R. C. Craddock, G. A. James, P. E. Holtzheimer, X. P. Hu, and H. S. Mayberg, "A whole brain fMRI atlas generated via spatially constrained spectral clustering," Hum. Brain Mapp., vol. 33, no. 8, pp. 1914–1928, 2012, doi: 10.1002/hbm.21333.

[75]     M. H. Lee, C. D. Smyser, and J. S. Shimony, "Resting-State fMRI: A Review of Methods and Clinical Applications," doi: 10.3174/ajnr.A3263.

[76]     Y. Zang, T. Jiang, Y. Lu, Y. He, and L. Tian, "Regional homogeneity approach to fMRI data analysis," doi: 10.1016/j.neuroimage.2003.12.030.

[77]     Q. H. Zou et al., "An improved approach to detection of amplitude of low-frequency fluctuation (ALFF) for resting-state fMRI: Fractional ALFF," J. Neurosci. Methods, vol. 172, no. 1, pp. 137–141, Jul. 2008, doi: 10.1016/j.jneumeth.2008.04.012.

[78]     P. Comon, "Independent Component Analysis," pp. 29–38, Jun. 1992, Accessed: May 23, 2021. [Online]. Available: https://hal.archives-ouvertes.fr/hal-00346684.

[79]     K. Li, L. Guo, J. Nie, G. Li, and T. Liu, "Review of methods for functional brain connectivity detection using fMRI," Comput. Med. Imaging Graph., vol. 33, no. 2, pp. 131–139, Mar. 2009, doi: 10.1016/j.compmedimag.2008.10.011.

[80]     M. G. Preti, T. A. Bolton, and D. Van De Ville, "The dynamic functional connectome: State-of-the-art and perspectives," Neuroimage, vol. 160, no. December, pp. 41–54, 2017, doi: 10.1016/j.neuroimage.2016.12.061.

[81]     M. J. Lee, B. Y. Park, S. Cho, H. Park, S. T. Kim, and C. S. Chung, "Dynamic functional connectivity of the migraine brain: A resting-state functional magnetic resonance imaging study," Pain, vol. 160, no. 12, pp. 2776–2786, 2019, doi: 10.1097/j.pain.0000000000001676.

[82]     A. D. Savva, G. D. Mitsis, and G. K. Matsopoulos, "Assessment of dynamic functional connectivity in resting-state fMRI using the sliding window technique," Brain Behav., vol. 9, no. 4, pp. 1–29, 2019, doi: 10.1002/brb3.1255.

[83]     J. Vohryzek, G. Deco, B. Cessac, M. L. Kringelbach, and J. Cabral, "Ghost Attractors in Spontaneous Brain Activity: Recurrent Excursions Into Functionally-Relevant BOLD Phase-Locking States," Front. Syst. Neurosci., vol. 14, no. April, pp. 1–15, 2020, doi: 10.3389/fnsys.2020.00020.

[84]     R. M. Hutchison et al., "Dynamic functional connectivity: Promise, issues, and interpretations," Neuroimage, vol. 80, pp. 360–378, Oct. 2013, doi: 10.1016/j.neuroimage.2013.05.079.

[85]     E. Glerean, J. Salmi, J. M. Lahnakoski, I. P. Jääskeläinen, and M. Sams, "Functional Magnetic Resonance Imaging Phase Synchronization as a Measure of Dynamic Functional Connectivity," Brain Connect., vol. 2, no. 2, pp. 91–101, Apr. 2012, doi: 10.1089/brain.2011.0068.

[86] J. Cabral et al., "Cognitive performance in healthy older adults relates to spontaneous switching between states of functional connectivity during rest," Sci. Rep., vol. 7, no. 1, pp. 1–13, 2017, doi: 10.1038/s41598-017-05425-7.

[87] F. Ribeiro, "Study of the brain's dynamic functional connectivity with simultaneous fMRI-EEG: a network science approach," Master Thesis, vol. 1, no. December, 2020.

[88] M. Yaesoubi, E. A. Allen, R. L. Miller, and V. D. Calhoun, "Dynamic coherence analysis of resting fMRI data to jointly capture state-based phase, frequency, and time-domain information," Neuroimage, vol. 120, pp. 133–142, Oct. 2015, doi: 10.1016/j.neuroimage.2015.07.002.

[89] C. A. Figueroa et al., "Altered ability to access a clinically relevant control network in patients remitted from major depressive disorder," Hum. Brain Mapp., vol. 40, no. 9, pp. 2771–2786, 2019, doi: 10.1002/hbm.24559.

[90] N. Leonardi et al., "Principal components of functional connectivity: A new approach to study dynamic brain connectivity during rest," Neuroimage, vol. 83, pp. 937–950, Dec. 2013, doi: 10.1016/j.neuroimage.2013.07.019.

[91] R. Abreu, A. Leal, and P. Figueiredo, "Identification of epileptic brain states by dynamic functional connectivity analysis of simultaneous EEG-fMRI: a dictionary learning approach," Sci. Rep., vol. 9, no. 1, pp. 1–18, Dec. 2019, doi: 10.1038/s41598-018-36976-y.

[92] T. J. Schwedt and C. D. Chong, "Functional imaging and migraine: New connections?," Current Opinion in Neurology, vol. 28, no. 3. Lippincott Williams and Wilkins, pp. 265–270, Jun. 06, 2015, doi: 10.1097/WCO.0000000000000194.

[93] T. Schwedt, C. C. Chiang, C. D. Chong, and D. W. Dodick, "Functional MRI of migraine," The Lancet Neurology, vol. 14, no. 1. Lancet Publishing Group, pp. 81–91, Jan. 01, 2015, doi: 10.1016/S1474-4422(14)70193-0.

[94] K. Skorobogatykh et al., "Functional connectivity studies in migraine: What have we learned?," Journal of Headache and Pain, vol. 20, no. 1. BioMed Central Ltd., pp. 1–10, Nov. 20, 2019, doi: 10.1186/s10194-019-1047-3.

[95] Z. Wang, Q. Yang, and L. M. Chen, "Abnormal dynamics of cortical resting state functional connectivity in chronic headache patients," Magn. Reson. Imaging, vol. 36, pp. 56–67, Feb. 2017, doi: 10.1016/j.mri.2016.10.015.

[96] Y. Tu et al., "Abnormal thalamocortical network dynamics in migraine," Neurology, vol. 92, no. 23, pp. 2706–2716, 2019, doi: 10.1212/WNL.0000000000007607.

[97] G. Dumkrieger, C. D. Chong, K. Ross, V. Berisha, and T. J. Schwedt, "Static and dynamic functional connectivity differences between migraine and persistent post-traumatic headache: A resting-state magnetic resonance imaging study," Cephalalgia, vol. 39, no. 11, pp. 1366–1381, 2019, doi: 10.1177/0333102419847728.

[98] Y. Zou, W. Tang, X. Qiao, and J. Li, "Aberrant modulations of static functional connectivity and dynamic functional network connectivity in chronic migraine," Quant. Imaging Med. Surg., vol. 11, no. 6, pp. 2253–2264, Jun. 2021, doi: 10.21037/qims-20-588.

[99] N. Imai, A. Moriya, and E. Kitamura, "Functional connectivity in migraineurs with photo-, phono-, or osmophobia: A static and dynamic resting-state functional magnetic resonance imaging study," Neurol. Clin. Neurosci., vol. 8, no. 6, pp. 390–398, 2020, doi: 10.1111/ncn3.12440.

[100] H. Chen et al., "Altered Dynamic Amplitude of Low-Frequency Fluctuations in Patients With Migraine Without Aura," Front. Hum. Neurosci., vol. 15, no. February, pp. 1–7, 2021, doi: 10.3389/fnhum.2021.636472.

[101] W. Nie et al., "Extraction and Analysis of Dynamic Functional Connectome Patterns in Migraine Sufferers: A Resting-State fMRI Study," Comput. Math. Methods Med., vol. 2021, 2021, doi: 10.1155/2021/6614520.

[102] M. F. Glasser et al., "The Minimal Preprocessing Pipelines for the Human Connectome Project," Neuroimage, vol. 80, p. 105, Oct. 2013, doi: 10.1016/J.NEUROIMAGE.2013.04.127.

[103] S. M. Smith et al., "Resting-state fMRI in the Human Connectome Project," Neuroimage, vol. 80, pp. 144–168, Oct. 2013, doi: 10.1016/J.NEUROIMAGE.2013.05.039.

[104] S. M. Smith, "Fast robust automated brain extraction," Hum. Brain Mapp., vol. 17, no. 3, p. 143, Nov. 2002, doi: 10.1002/HBM.10062.

[105] Y. Zhang, M. Brady, and S. Smith, "Segmentation of brain MR images through a hidden Markov random field model and the expectation-maximization algorithm," IEEE Trans. Med. Imaging, vol. 20, no. 1, pp. 45–57, Jan. 2001, doi: 10.1109/42.906424.

[106] M. Jenkinson, P. Bannister, M. Brady, and S. Smith, "Improved Optimization for the Robust and Accurate Linear Registration and Motion Correction of Brain Images," Neuroimage, vol. 17, no. 2, pp. 825–841, Oct. 2002, doi: 10.1006/NIMG.2002.1132.

[107] J. Andersson, M. Jenkinson, and S. Smith, "Non-linear registration aka Spatial normalisation FMRIB Technial Report TR07JA2," 2007.

[108] G. Salimi-Khorshidi, G. Douaud, C. . Beckmann, M. . Glasser, L. Griffanti, and S. . Smith, "Automatic Denoising of Functional MRI Data: Combining Independent Component Analysis and Hierarchical Fusion of Classifiers," Neuroimage, vol. 90, p. 449, Apr. 2014, doi: 10.1016/J.NEUROIMAGE.2013.11.046.

[109] M. W. Woolrich, B. D. Ripley, M. Brady, and S. M. Smith, "Temporal autocorrelation in univariate linear modeling of FMRI data," Neuroimage, vol. 14, no. 6, pp. 1370–1386, 2001, doi: 10.1006/NIMG.2001.0931.

[110] S. M. Smith and J. M. Brady, "SUSAN—A New Approach to Low Level Image Processing," Int. J. Comput. Vis. 1997 231, vol. 23, no. 1, pp. 45–78, 1997, doi: 10.1023/A:1007963824710.

[111] L. D. Lord et al., "Dynamical exploration of the repertoire of brain networks at rest is modulated by psilocybin," Neuroimage, vol. 199, no. May, pp. 127–142, 2019, doi: 10.1016/j.neuroimage.2019.05.060.

[112] P. Pascual-Marqui, C. M. Michel, and D. Lehmann, "Segmentation of brain electrical activity into microstates: model estimation and validation," IEEE Trans. Biomed. Eng., vol. 42, no. 7, pp. 658–665, 1995, doi: 10.1109/10.391164.

[113] A. Aires, "EEG correlates of fMRI dynamic functional connectivity states," Master Thesis, no. November, 2019.

[114] D. J. Bora and A. K. Gupta, "Effect of Different Distance Measures on the Performance of K-Means Algorithm: An Experimental Study in Matlab," May 2014, Accessed: Jul. 16, 2021. [Online]. Available: https://arxiv.org/abs/1405.7471v1.

[115] S. Alonso Martínez, G. Deco, G. J. Ter Horst, and J. Cabral, "The Dynamics of Functional Brain Networks Associated With Depressive Symptoms in a Nonclinical Sample," Front. Neural Circuits, vol. 14, no. September, 2020, doi: 10.3389/fncir.2020.570583.

[116] A. Camargo, F. Azuaje, H. Wang, and H. Zheng, "Permutation-based statistical tests for multiple hypotheses," Source Code Biol. Med. 2008 31, vol. 3, no. 1, pp. 1–8, Oct. 2008, doi: 10.1186/1751-0473-3-15.

[117] N. Gogolla, "The insular cortex," Current Biology, vol. 27, no. 12. Cell Press, pp. R580–R586, Jun. 19, 2017, doi: 10.1016/j.cub.2017.05.010.

[118] A. R. Lopes, A. S. Letournel, and J. Cabral, "Altered resting-state network dynamics in Schizophrenia," medRxiv, pp. 1–9, 2020, doi: 10.1101/2020.07.21.20157347.

[119] M. Pedersen, A. Omidvarnia, A. Zalesky, and G. D. Jackson, "On the relationship between instantaneous phase synchrony and correlation-based sliding windows for time-resolved fMRI connectivity analysis," Neuroimage, vol. 181, pp. 85–94, Nov. 2018, doi: 10.1016/J.NEUROIMAGE.2018.06.020.

[120] H. Honari, A. S. Choe, and M. A. Lindquist, "Evaluating phase synchronization methods in fMRI: A comparison study and new approaches," Neuroimage, vol. 228, p. 117704, Mar. 2021, doi: 10.1016/J.NEUROIMAGE.2020.117704.

[121] G. Coppola et al., "Thalamo-cortical network activity during spontaneous migraine attacks," Neurology, vol. 87, no. 20, pp. 2154–2160, Nov. 2016, doi: 10.1212/WNL.0000000000003327.

[122] J. Liu et al., "Disrupted resting-state functional connectivity and its changing trend in migraine suffers," Hum. Brain Mapp., vol. 36, no. 5, pp. 1892–1907, May 2015, doi: 10.1002/hbm.22744.

[123] A. V. Apkarian, M. N. Baliki, and P. Y. Geha, "Towards a theory of chronic pain," Prog. Neurobiol., vol. 87, no. 2, p. 81, Feb. 2009, doi: 10.1016/J.PNEUROBIO.2008.09.018.

[124] D. M. Niddam, K. Lai, J. Fuh, C. N. Chuang, W. Chen, and S. Wang, "Reduced functional connectivity between salience and visual networks in migraine with aura:," https://doi.org/10.1177/0333102415583144, vol. 36, no. 1, pp. 53–66, Apr. 2015, doi: 10.1177/0333102415583144.

[125] A. Russo et al., "Executive resting-state network connectivity in migraine without aura," Cephalalgia, vol. 32, no. 14, pp. 1041–1048, Oct. 2012, doi: 10.1177/0333102412457089.

[126] Z. Li et al., "The altered right frontoparietal network functional connectivity in migraine and the modulation effect of treatment:," https://doi.org/10.1177/0333102416641665, vol. 37, no. 2, pp. 161–176, Apr. 2016, doi: 10.1177/0333102416641665.

[127] T. Xue et al., "Intrinsic Brain Network Abnormalities in Migraines without Aura Revealed in Resting-State fMRI," PLoS One, vol. 7, no. 12, p. e52927, Dec. 2012, doi: 10.1371/journal.pone.0052927.

[128] D. A. Seminowicz and K. D. Davis, "Pain Enhances Functional Connectivity of a Brain Network Evoked by Performance of a Cognitive Task," https://doi.org/10.1152/jn.01210.2006, vol. 97, no. 5, pp. 3651–3659, May 2007, doi: 10.1152/JN.01210.2006.

[129] L. Heine et al., "Resting state networks and consciousness," Front. Psychol., vol. 3, no. AUG, p. 295, Aug. 2012, doi: 10.3389/fpsyg.2012.00295.

[130] J. Zhang et al., "The sensorimotor network dysfunction in migraineurs without aura: a resting-state fMRI study," doi: 10.1007/s00415-017-8404-4.

[131] R. Araújo, "Functional connectivity during spontaneous migraine attacks compared to pain-free periods: a resting-state fMRI study," Master Thesis, no. November, 2020.

[132] A. Hougaard, F. M. Amin, H. B. W. Larsson, E. Rostrup, and M. Ashina, "Increased intrinsic brain connectivity between pons and somatosensory cortex during attacks of migraine with aura," Hum. Brain Mapp., vol. 38, no. 5, pp. 2635–2642, May 2017, doi: 10.1002/hbm.23548.

[133] M. C. Bushnell, M. Čeko, and L. A. Low, "Cognitive and emotional control of pain and its disruption in chronic pain," Nat. Rev. Neurosci. 2013 147, vol. 14, no. 7, pp. 502–511, May 2013, doi: 10.1038/nrn3516.

[134] A. . Harriott and T. . Schwedt, "Migraine is Associated With Altered Processing of Sensory Stimuli," doi: 10.1007/s11916-014-0458-8.

[135] F. Puledda, D. Ffytche, O. O'Daly, and P. J. Goadsby, "Imaging the Visual Network in the Migraine Spectrum," Front. Neurol., vol. 10, Dec. 2019, doi: 10.3389/FNEUR.2019.01325.

[136] A. Ashourvan, S. Gu, M. G. Mattar, J. M. Vettel, and D. S. Bassett, "The energy landscape underpinning module dynamics in the human brain connectome," Neuroimage, vol. 157, pp. 364–380, Aug. 2017, doi: 10.1016/J.NEUROIMAGE.2017.05.067.

[137] L. H. Schulte and A. May, "Functional Neuroimaging in Migraine: Chances and Challenges," Headache, vol. 56, no. 9, pp. 1474–1481, Oct. 2016, doi: 10.1111/head.12944.

[138] G. Mele, C. Cavaliere, V. Alfano, M. Orsini, M. Salvatore, and M. Aiello, "Simultaneous EEG-fMRI for Functional Neurological Assessment," Front. Neurol., vol. 0, no. JUL, p. 848, 2019, doi: 10.3389/FNEUR.2019.00848.

# Appendix A

# RSNs vectors into the atlases spaces
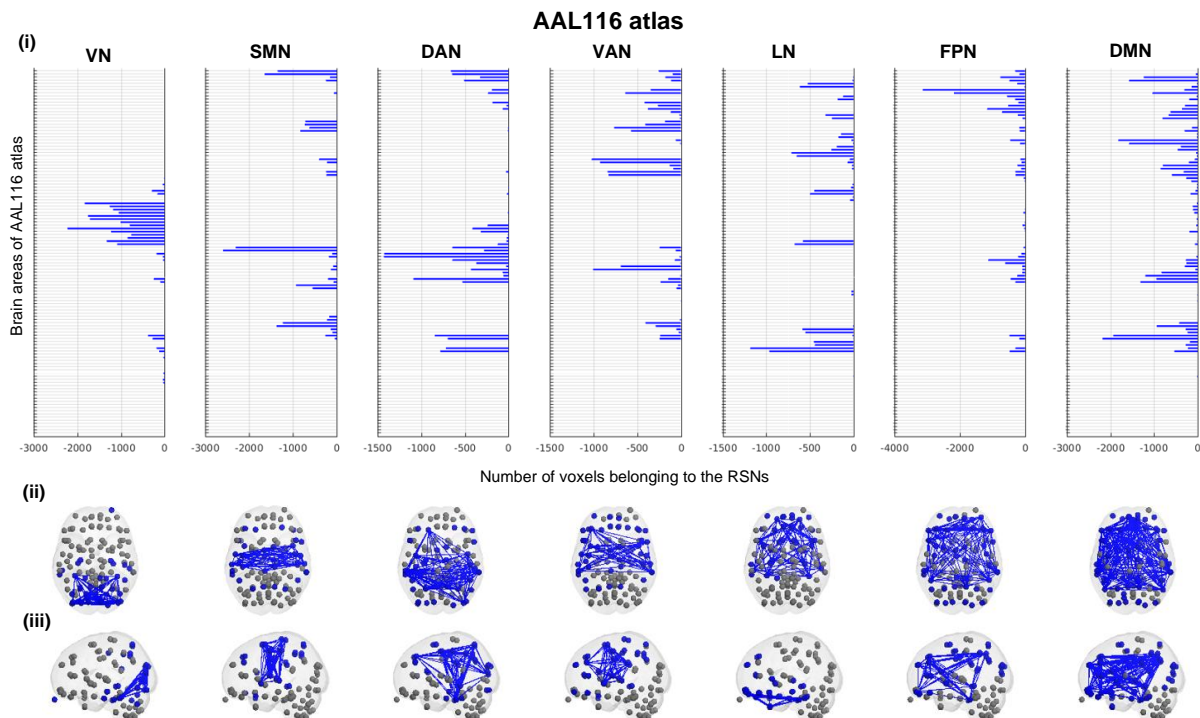
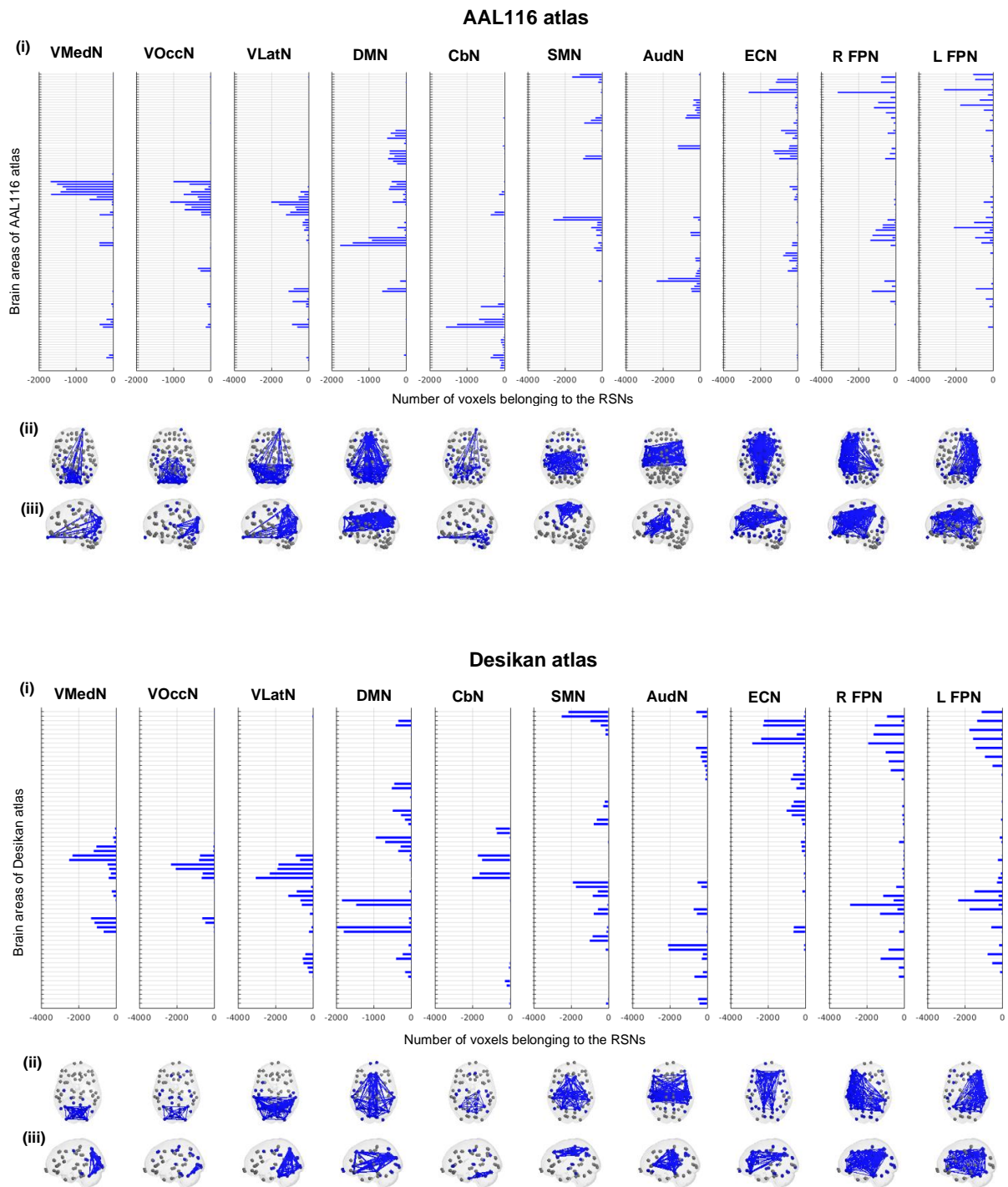## A.1. Transformation of Yeo repertoire



Figure A.1. Yeo repertoire transformed into the atlases (AAL116, Desikan and Harvard-Oxford) spaces and represented through RSN vectors by **(i)** the distribution of the number of 2 mm$^3$ MNI voxels in each brain area belonging to the corresponding RSN, obtaining a vector with $N$ (number of brain areas) elements that can be correlated with the cluster centroid vectors of the dFC states and the functional network that detach from the global mode of BOLD signal fluctuation represented in the atlas cortical space (**(ii)** axial and **(iii)** sagittal slices). The brain areas contributing to each RSN are displayed with dark blue color and those without any voxel belonging to the RSN are displayed with grey color. The brain areas with more than 400 MNI voxels contributing to the RSN are linked with blue edges. VN = Visual Network; SMN = Somatomotor Network; DAN = Dorsal Attention Network; VAN = Ventral Attention Network; LN = Limbic Network; FPN = Frontoparietal Network; DMN = Default Mode Network.

## Desikan atlas

**(i)**

| VN | SMN | DAN | VAN | LN | FPN | DMN |

Brain areas of Desikan atlas

Number of voxels belonging to the RSNs

**(ii)**

**(iii)**

## Harvard-Oxford atlas

**(i)**

| VN | SMN | DAN | VAN | LN | FPN | DMN |

Brain areas of Harvard-Oxford atlas

Number of voxels belonging to the RSNs

**(ii)**

**(iii)**

Figure A.1. *(Continued).*

# A.2. Transformation of Smith repertoire

## AAL116 atlas



## Desikan atlas



Figure A.2. Smith repertoire transformed into the atlases (AAL116, Desikan and Harvard-Oxford) spaces and represented through RSN vectors by **(i)** the distribution of the number of 2 mm$^3$ MNI voxels in each brain area belonging to the corresponding RSN, obtaining a vector with $N$ (number of brain areas) elements that can be correlated with the cluster centroid vectors of the dFC states and the functional network that detach from the global mode of BOLD signal fluctuation represented in the atlas cortical space (**(ii)** axial and **(iii)** sagittal slices). The brain areas contributing to each RSN are displayed with dark blue color and those without any voxel belonging to the RSN are displayed with grey color. The brain areas with more than 200 MNI voxels contributing to the RSN are linked with blue edges. VMedN = Visual Medial Network; VOccN = Visual Occipital Network; VLatN = Visual Lateral Network; DMN = Default Mode Network; CbN = Cerebellar Network; SMN = Sensorimotor Network; AudN = Auditory Network; ECN = Executive Control Network; R/L FPN = Right/Left Frontoparietal Network.

# Harvard-Oxford atlas
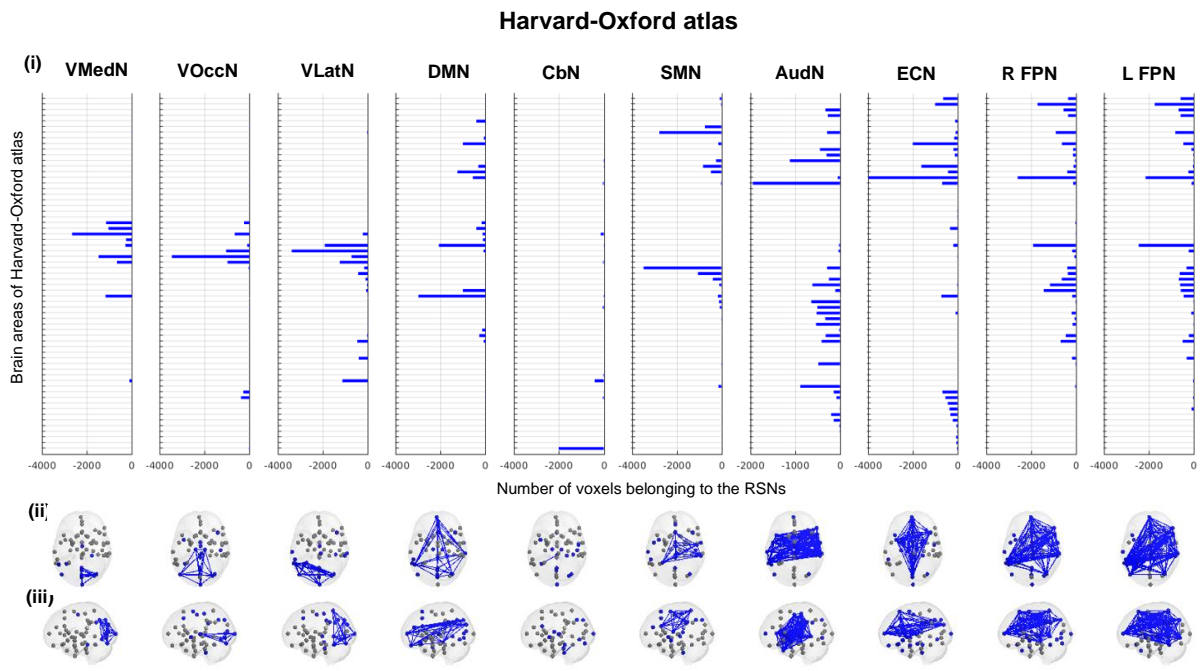


Figure A.2. *(Continued).*

# Appendix B

# Results obtained with the k-means clustering algorithm

## B.1. Migraine interictal dataset
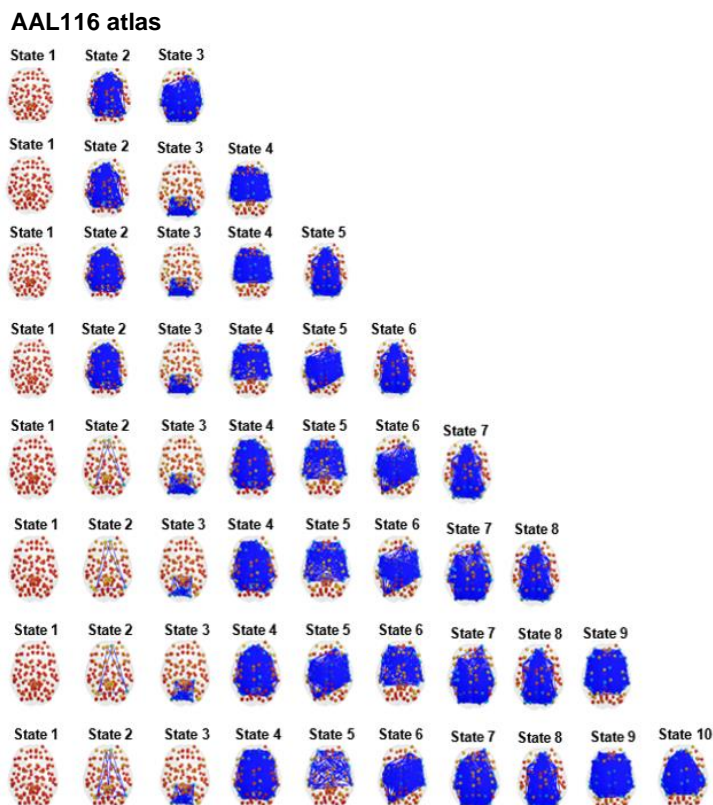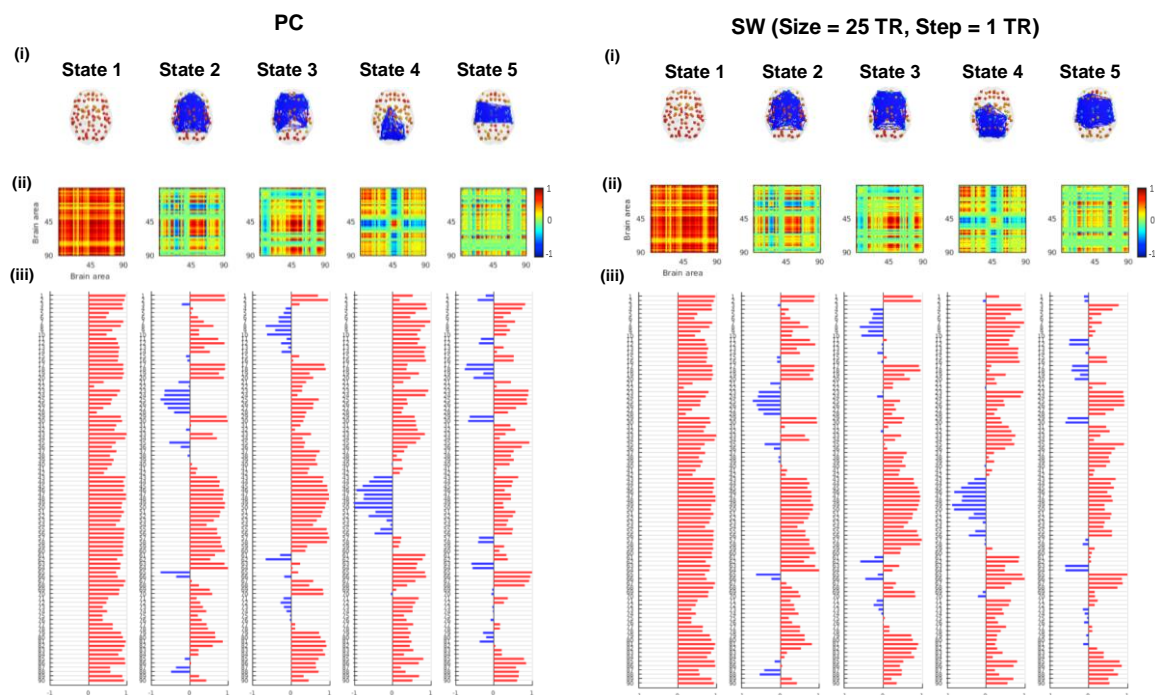


**AAL116 atlas**

Figure B.1. dFC states obtained with the k-means clustering algorithm ($k = 3$ to $k = 15$), displayed according to their decreasing probability of occurrence within each $k$, for the AAL116, Desikan and Harvard-Oxford atlases, and the PC method. Each dFC state is represented by its $V_c$ as a network in the AAL90 cortical space (axial slice), in which the elements of $V_c$ are placed at the center of gravity of the respective brain region, shaped as spheres colored according to their sign (red to yellow spheres represent positive elements from 1 to 0, cyan to dark blue spheres represent negative elements from 0 to -1), and areas with $V_c \leq 0.1$ are linked with dark blue edges.

## AAL116 atlas *(Continued)*



## Desikan atlas
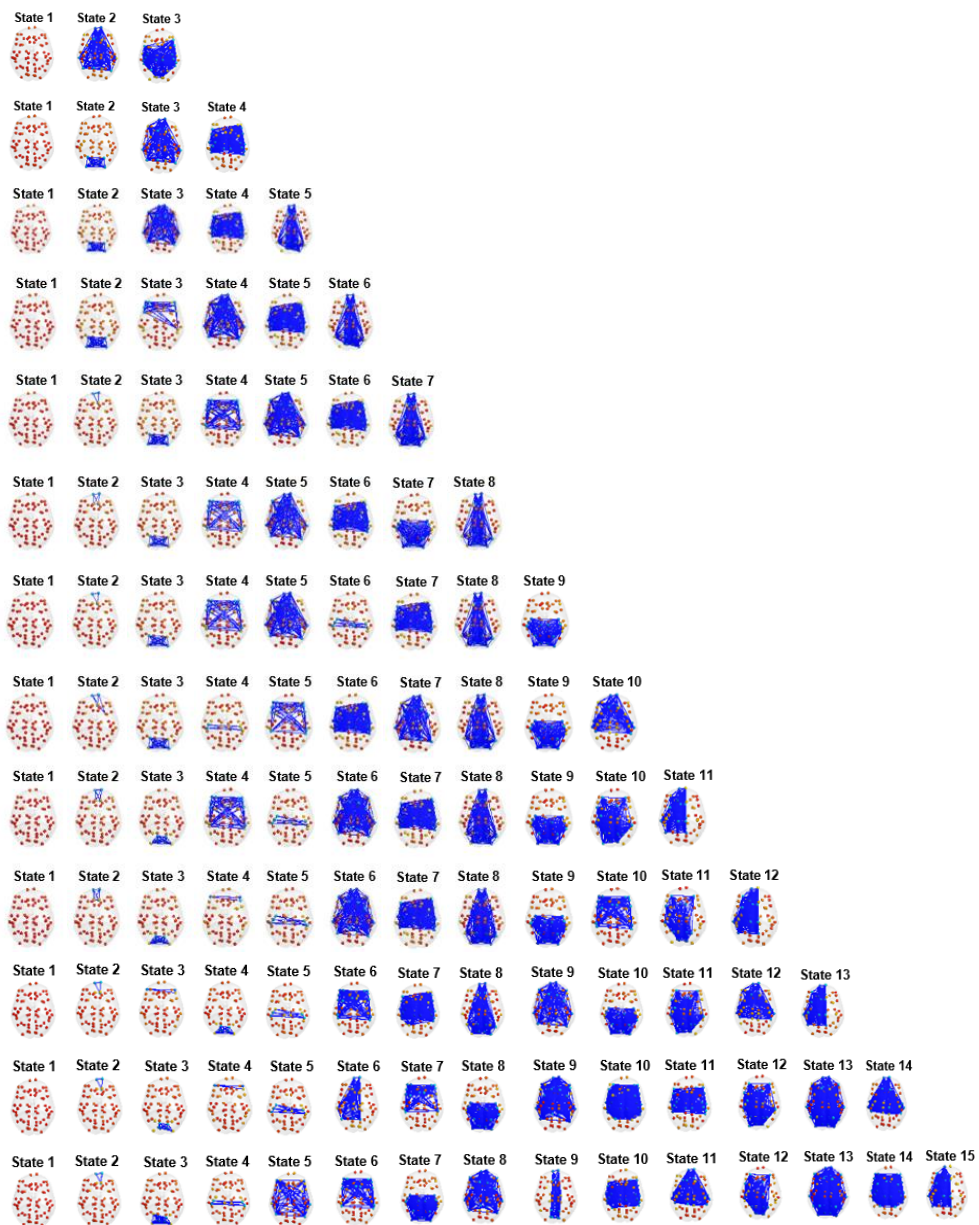


Figure B.1. *(Continued)*

## Harvard-Oxford atlas
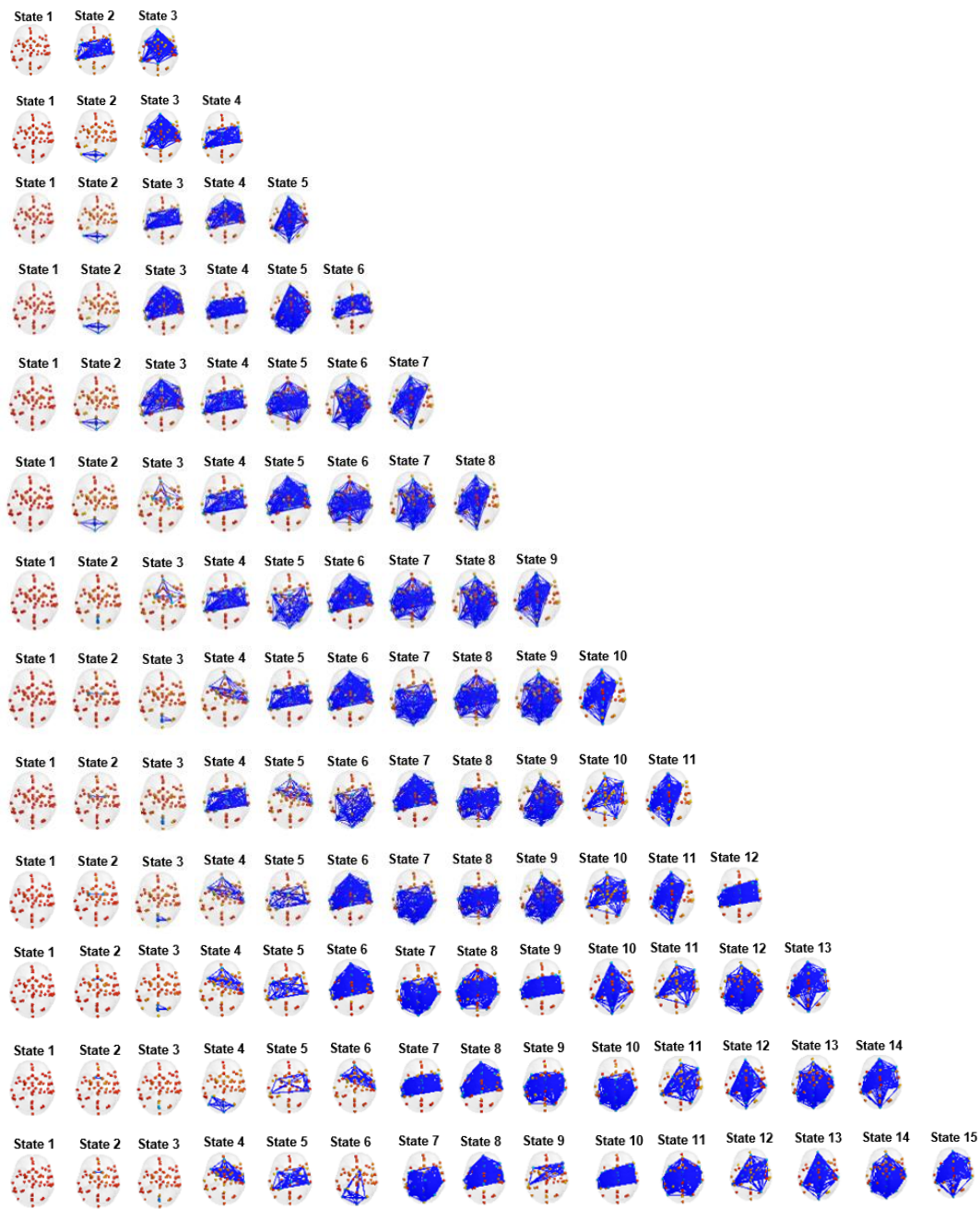


Figure B.1. *(Continued)*

## B.2. Migraine interictal dataset without the ICA clean-up and nuisance regression preprocessing steps

**AAL90 atlas**
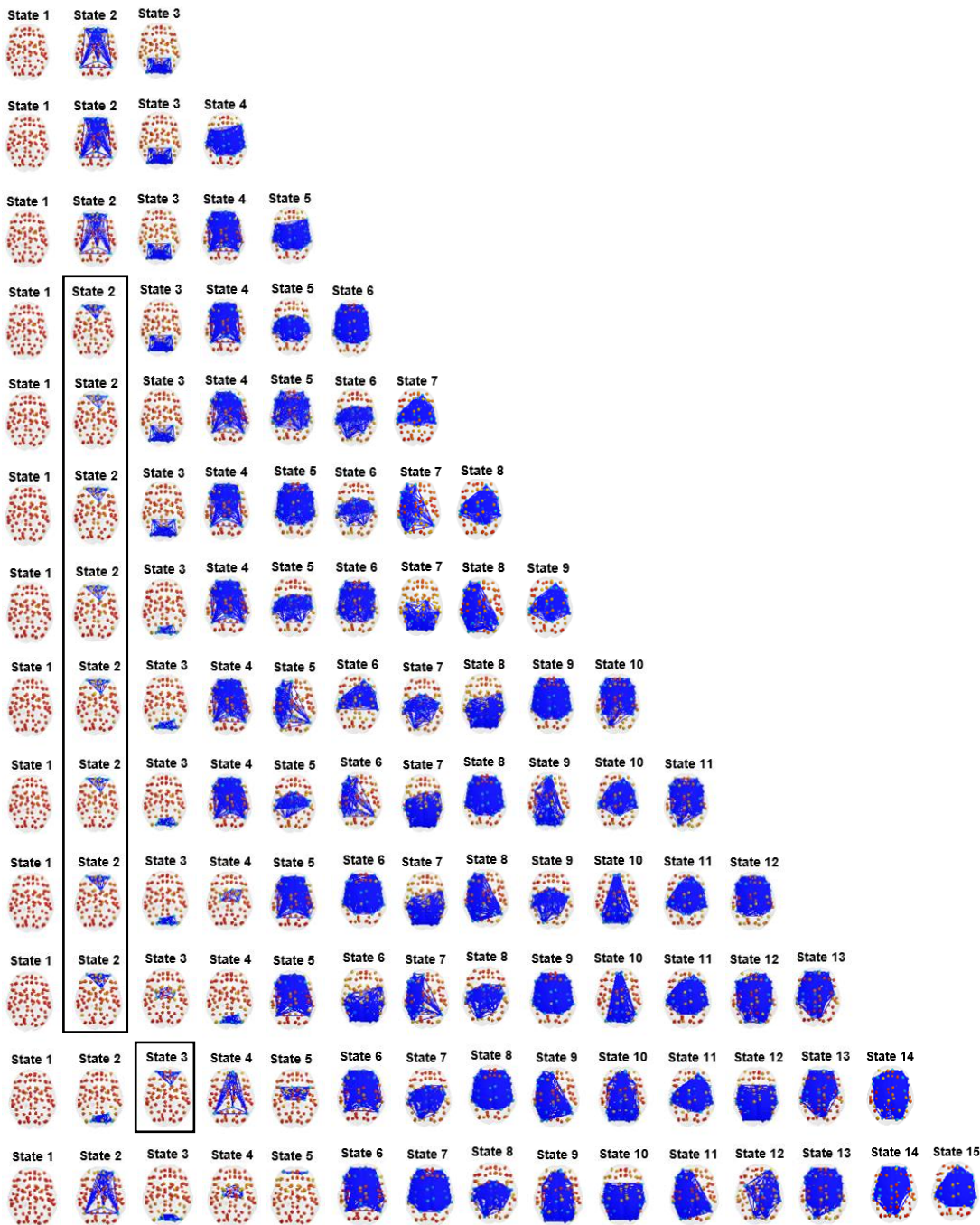


Figure B.2. dFC states obtained with the k-means clustering algorithm ($k = 3$ to $k = 15$), displayed according to their decreasing probability of occurrence within each $k$, for the AAL90 atlas and the PC method without the ICA clean-up and nuisance regression preprocessing steps. Each dFC state is represented by its $V_c$ as a network in the AAL90 cortical space (axial slice), in which the elements of $V_c$ are placed at the center of gravity of the respective brain region, shaped as spheres colored according to their sign (red to yellow spheres represent positive elements from 1 to 0, cyan to dark blue spheres represent negative elements from 0 to -1), and areas with $V_c \leq 0.1$ are linked with dark blue edges. The black rectangles mark the frontal state.

# Appendix C

# Results obtained for the HCP dataset



Figure C.1. dFC states obtained with the k-means clustering algorithm ($k = 5$), displayed according to their decreasing probability of occurrence, for the AAL90 atlas and PC and SW (sizes of 25 TR, 35 TR and 45 TR, step of 1 TR) methods. Each dFC state is represented by its $V_c$: **(i)** as a network in the AAL90 cortical space (axial slice), in which the elements of $V_c$ are placed at the center of gravity of the respective brain region, shaped as spheres colored according to their sign (red to yellow spheres represent positive elements from 1 to 0, cyan to dark blue spheres represent negative elements from 0 to -1), and areas with $V_c \leq 0.1$ are linked with dark blue edges; **(ii)** by the outer product $V_c V_c^T$; and **(iii)** as a bar plot displaying the projection of the BOLD phase in each brain region into $V_c$.
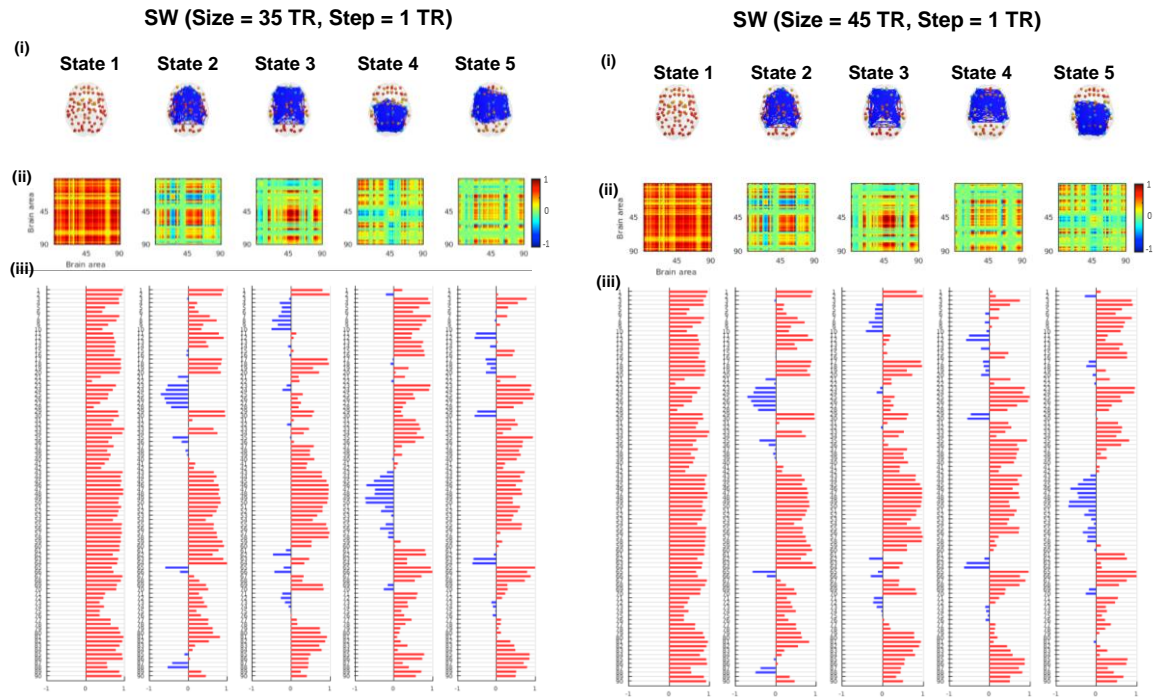
Figure C.1. *(Continued).*
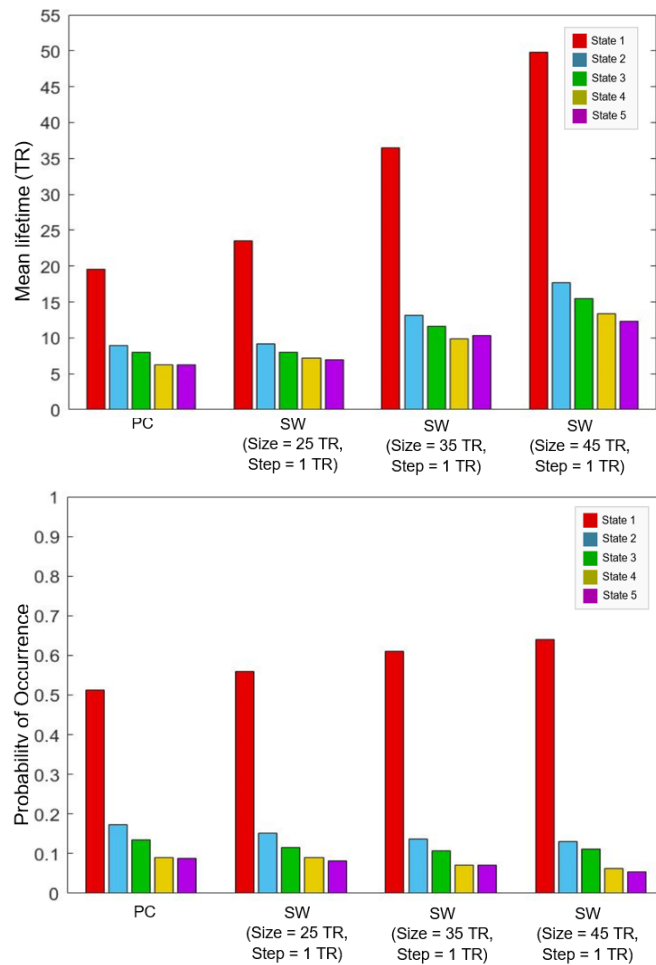


Figure C.2. Mean lifetime **(i)** and probability of occurrence **(ii)** of each dFC state obtained with the k-means clustering algorithm ($k = 5$), for the AAL90 atlas and the PC and SW with window sizes of 25 TR, 35 TR and 45 TR.
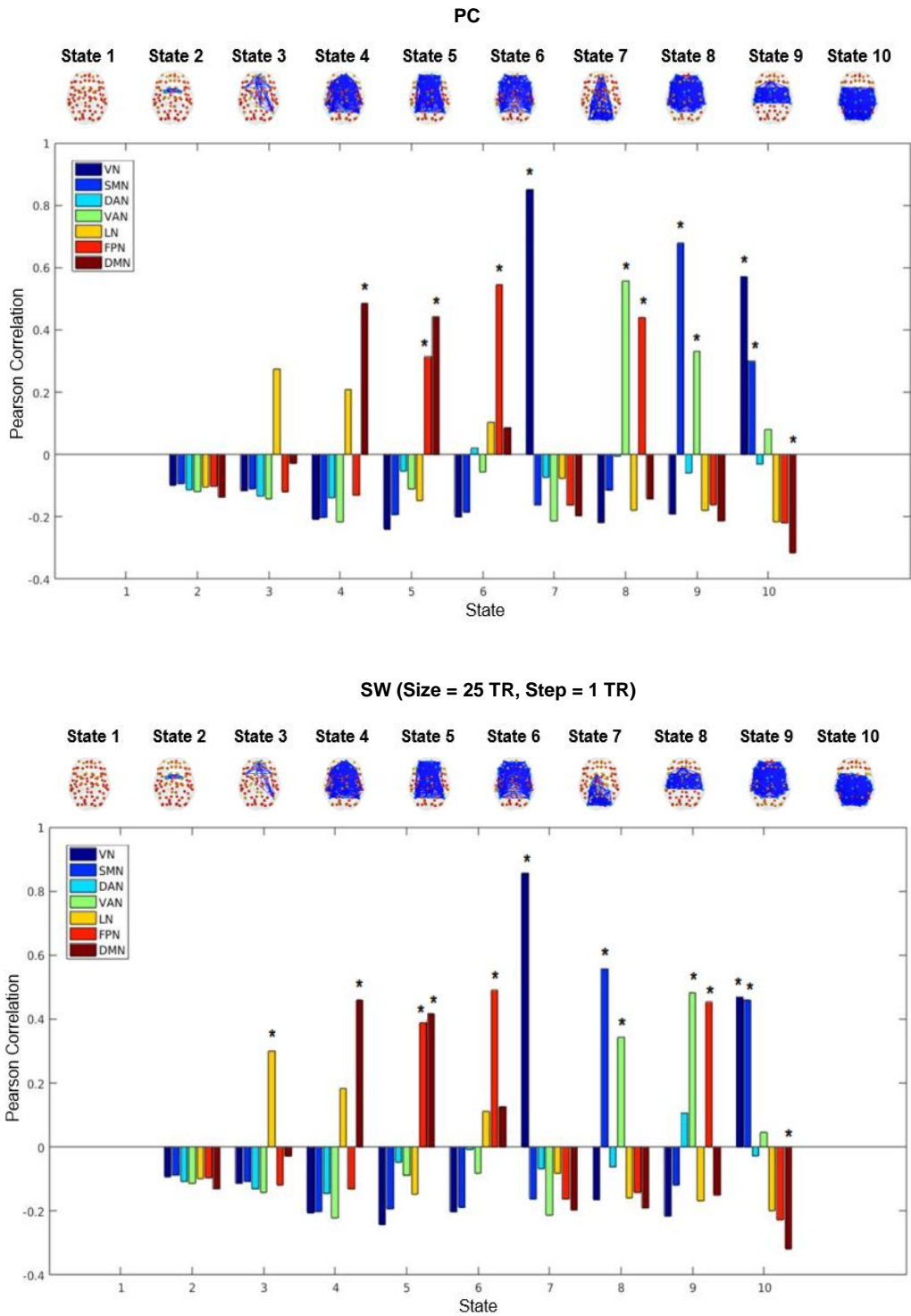
Figure C.3. Pearson correlation coefficient computed between the cluster centroid vectors of the dFC states ($k$ = 10) obtained with the PC and SW (sizes of 25 TR, 35 TR and 45 TR) methods and the seven Yeo RSNs transformed into the AAL90 space. *: Statistically significant correlations ($p$-value < 0.005); VN = Visual Network; SMN = Somatomotor Network; DAN = Dorsal Attention Network; VAN = Ventral Attention Network; LN = Limbic Network; FPN = Frontoparietal Network; DMN = Default Mode Network.

**SW (Size = 35 TR, Step = 1 TR)**



**SW (Size = 45 TR, Step = 1 TR)**
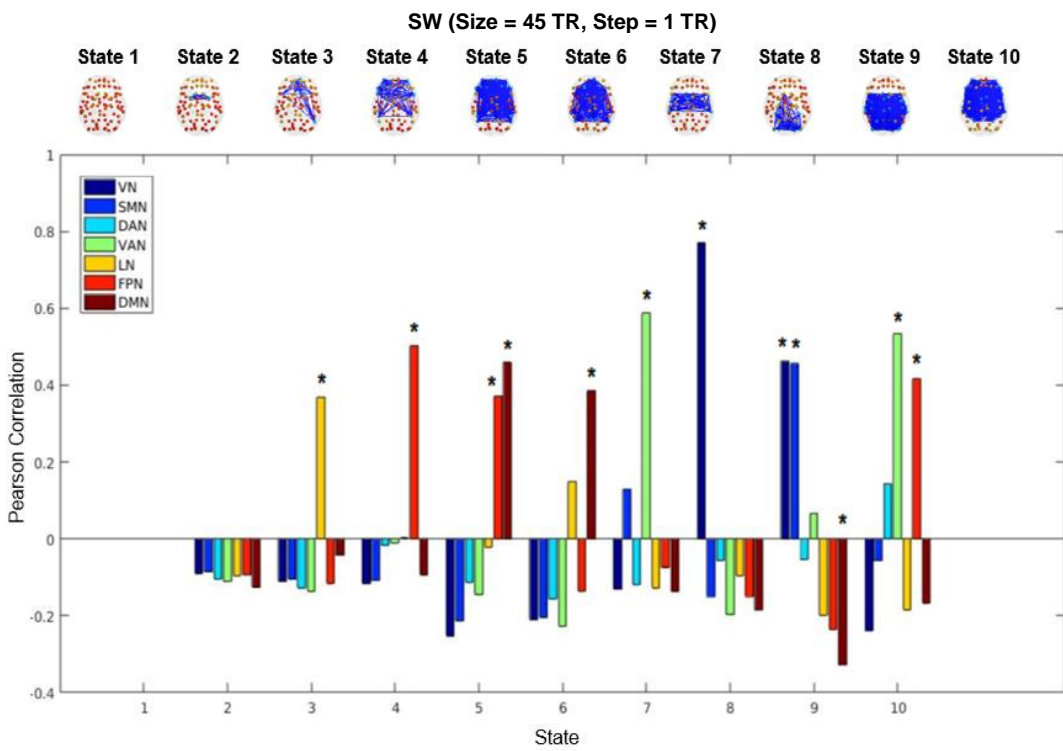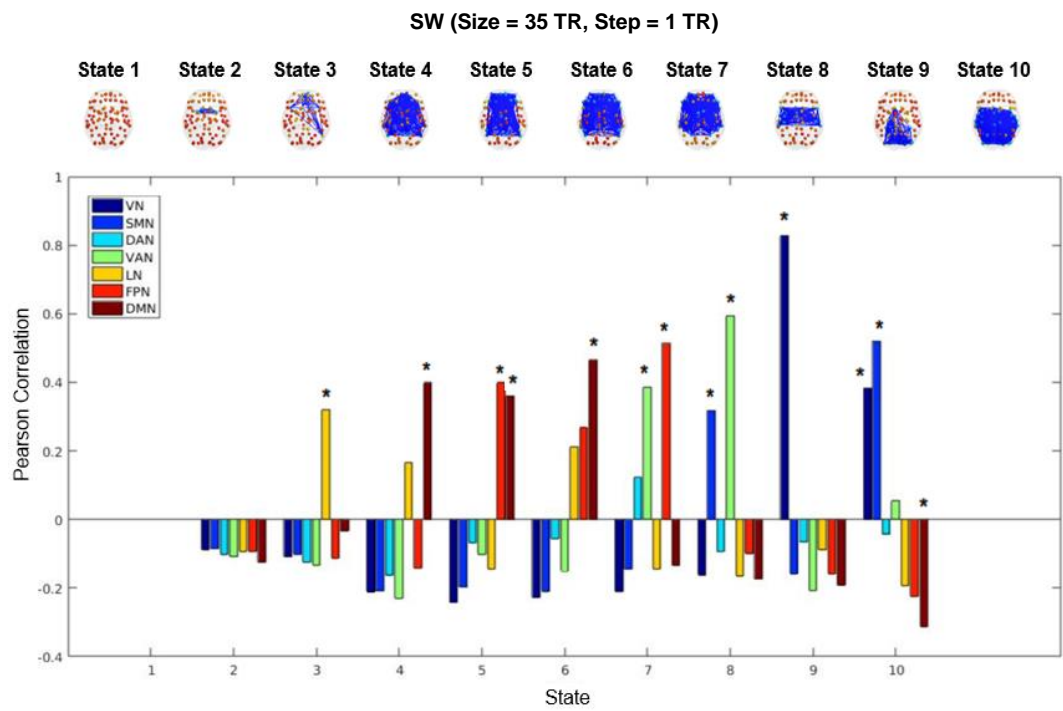


Figure C.3. *(Continued).*

# Appendix D

# Comparison Between Groups

## D.1. Migraineurs: Interictal vs. Ictal sessions
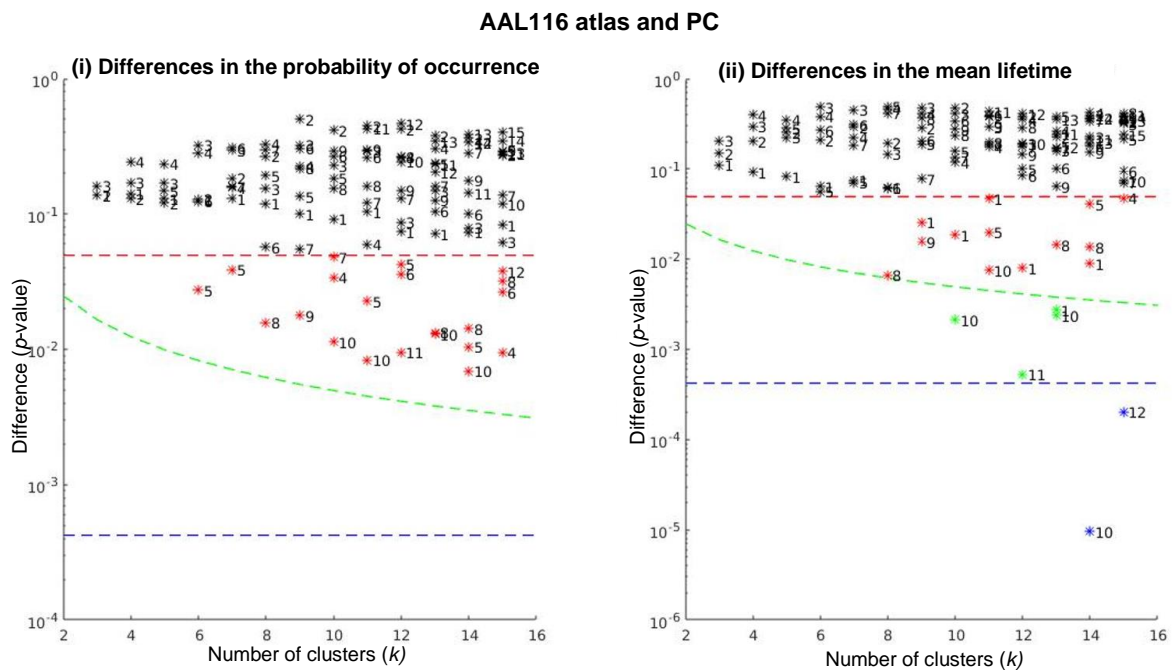


Figure D.1. Significance of differences in the **(i)** probabilities of occurrence and **(ii)** mean lifetimes of dFC states obtained with the AAL116, Desikan and Harvard-Oxford atlases and the PC method, and AAL90 atlas and the SW method (size of 25 TR), between migraine interictal and ictal sessions, as a function of $k$. The red, green and blue dashed lines represent $p$-values equal to 0.05, 0.05/$k$ and 0.05/$\Sigma k$, respectively. Thus, all dFC states noted with a black asterisk (above the red line) passed the null hypothesis, i.e., present no significant difference between groups; the FC patterns marked with a red asterisk (above the green and below the red lines, $p$-value < 0.05, > 95 % of confidence) rejected the null hypothesis but did not pass the correction for multiple comparisons, being considered possible false positives; the states noted with a green asterisk (above the blue and below the green lines) rejected the null hypothesis with $p$-value < 0.05/$k$; and the states noted with a blue asterisk (below the blue line) rejected the null hypothesis with $p$-value < 0.05/$\Sigma k$.

**Desikan atlas and PC**

**(i) Differences in the probability of occurrence**



**(ii) Differences in the mean lifetime**



**Harvard-Oxford atlas and PC**

**(i) Differences in the probability of occurrence**



**(ii) Differences in the mean lifetime**



Figure D.1. *(Continued).*

102
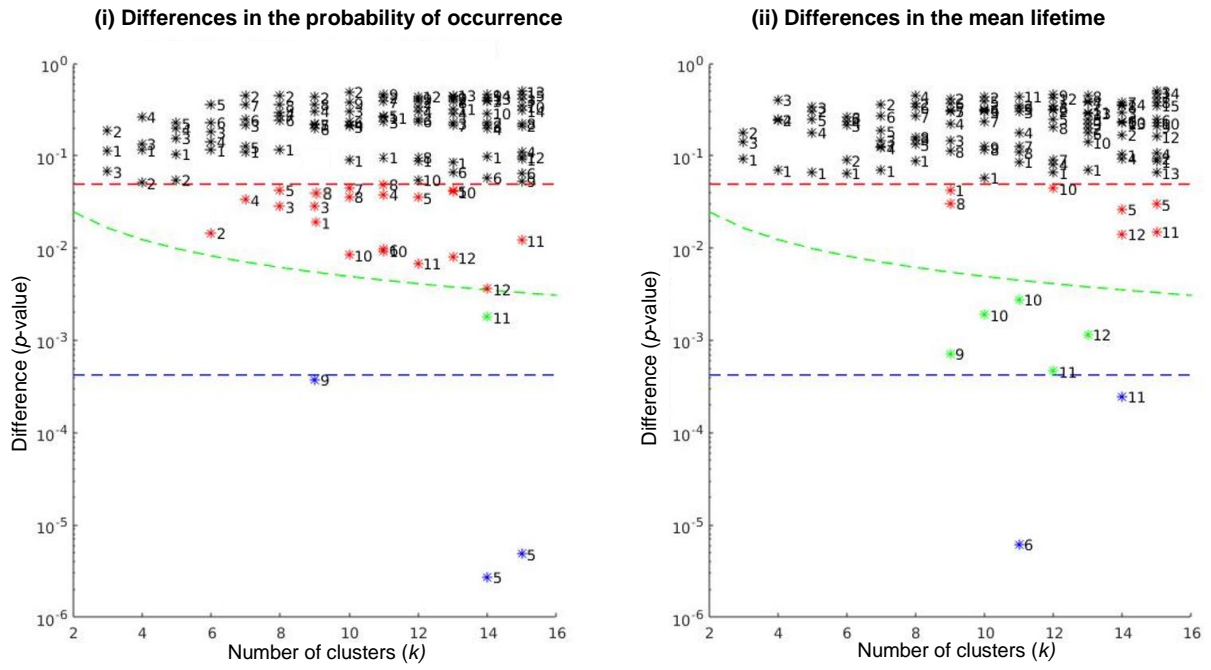
**AAL90 atlas and SW (Size = 25 TR, Step = 1 TR)**



**(i) Differences in the probability of occurrence**

**(ii) Differences in the mean lifetime**
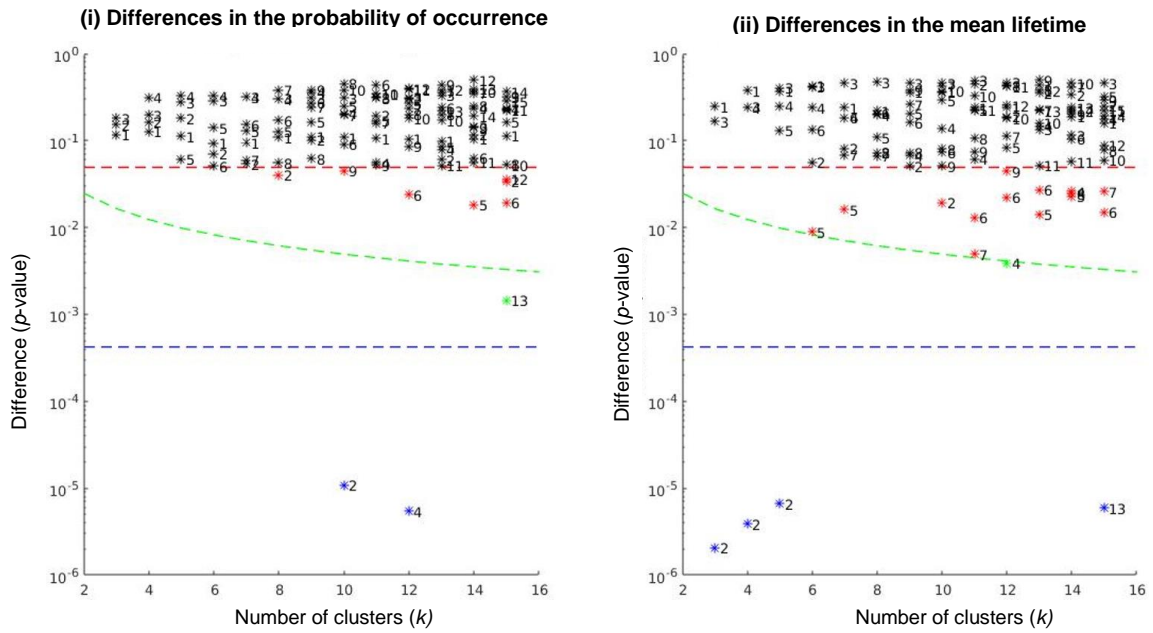
Figure D.1. *(Continued).*
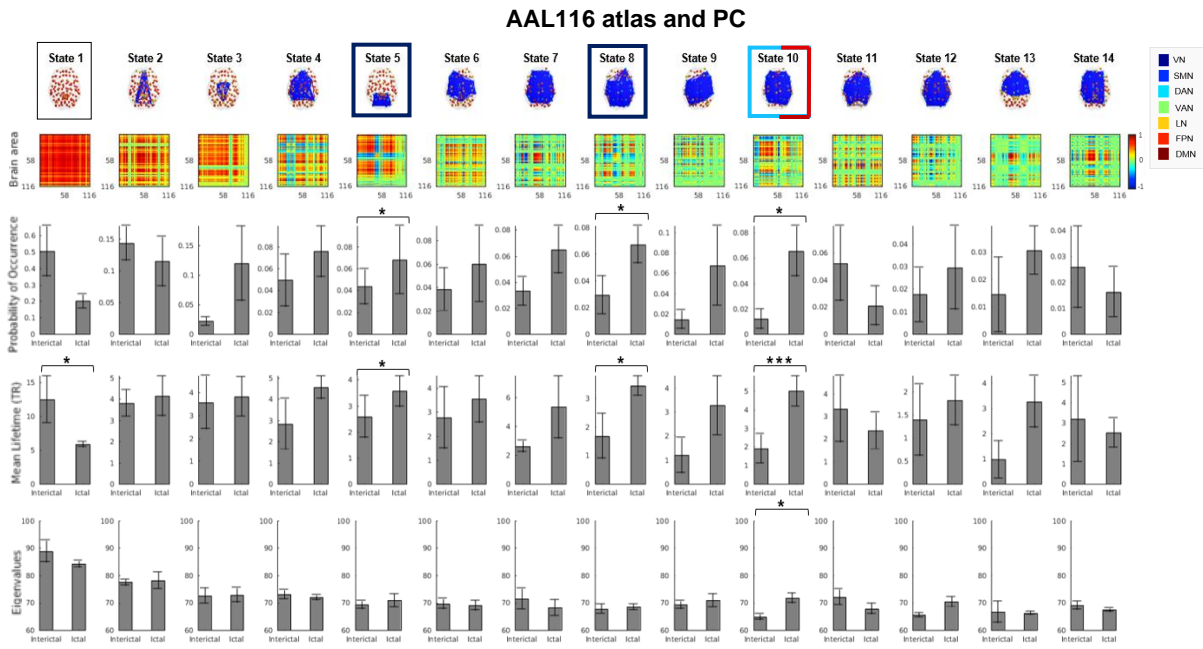
**AAL116 atlas and PC**



Figure D.2. dFC states obtained with the k-means clustering algorithm, displayed according to their decreasing probability of occurrence, for the AAL116 ($k = 14$), Desikan ($k = 9$), Harvard-Oxford ($k = 13$) and AAL90 ($k = 7$) atlases and PC method, and for the AAL90 atlas ($k = 3$, $k = 12$ and $k = 15$) and the SW method (size of 25 TR). Each dFC state is represented by its $V_c$ as: a network in the atlas cortical space (axial slice), in which the elements of $V_c$ are placed at the center of gravity of the respective brain region, shaped as spheres coloured according to their sign (red to yellow spheres represent positive elements from 1 to 0, cyan to dark blue spheres represent negative elements from 0 to -1), and areas with $V_c \leq 0.1$ are linked with dark blue edges; and by the outer product $V_c V_c^T$. Below the representation of each state, the respective probabilities of occurrence, mean lifetimes and mean eigenvalues are displayed for the migraine patients in the interictal and ictal sessions. The rectangle marks states with statistically significant between-group differences and correlation to any Yeo RSN, with the colours representing the RSN. The black rectangle marks the global mode. * Significant difference before correcting for multiple comparisons ($p$-value < 0.05); ** Significant difference after correcting for multiple comparisons ($p$-value < 0.05/k); *** Significant difference after correcting for multiple comparisons ($p$-value < 0.05/Σk).

103

## Desikan atlas and PC



## Harvard-Oxford atlas and PC
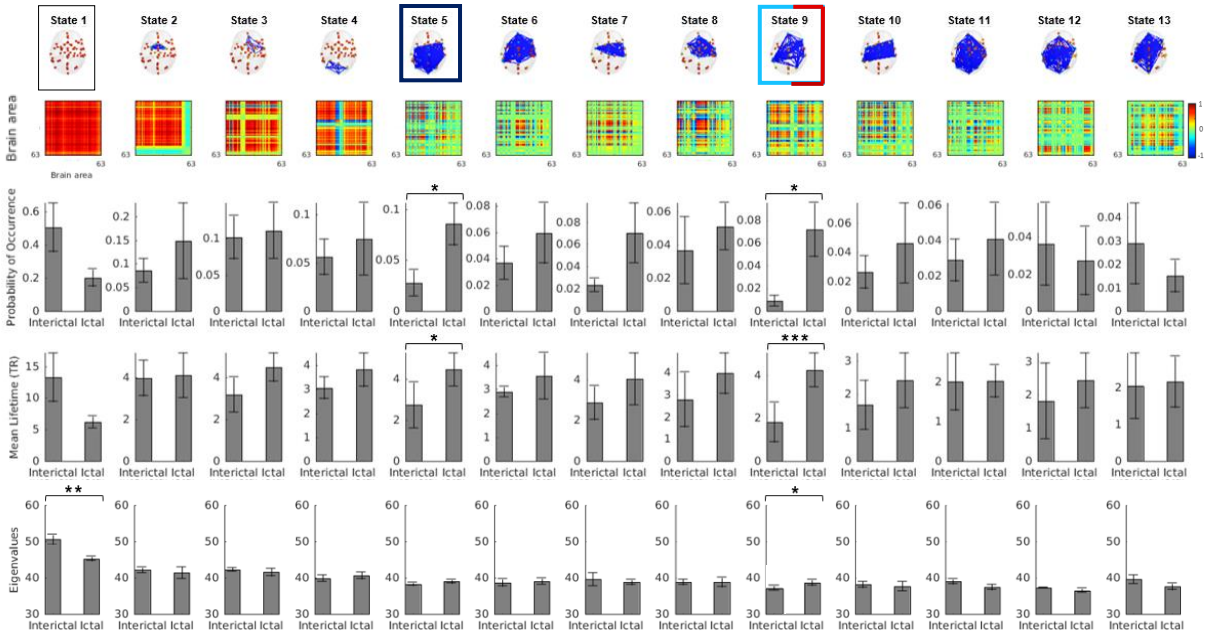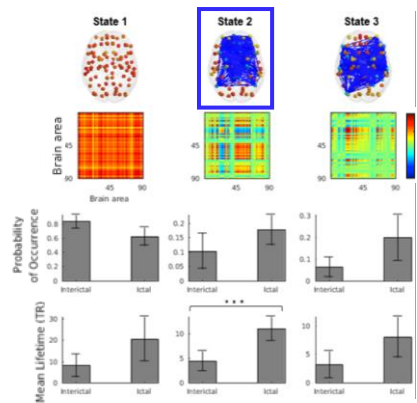


## AAL90 atlas and SW (Size = 25 TR)
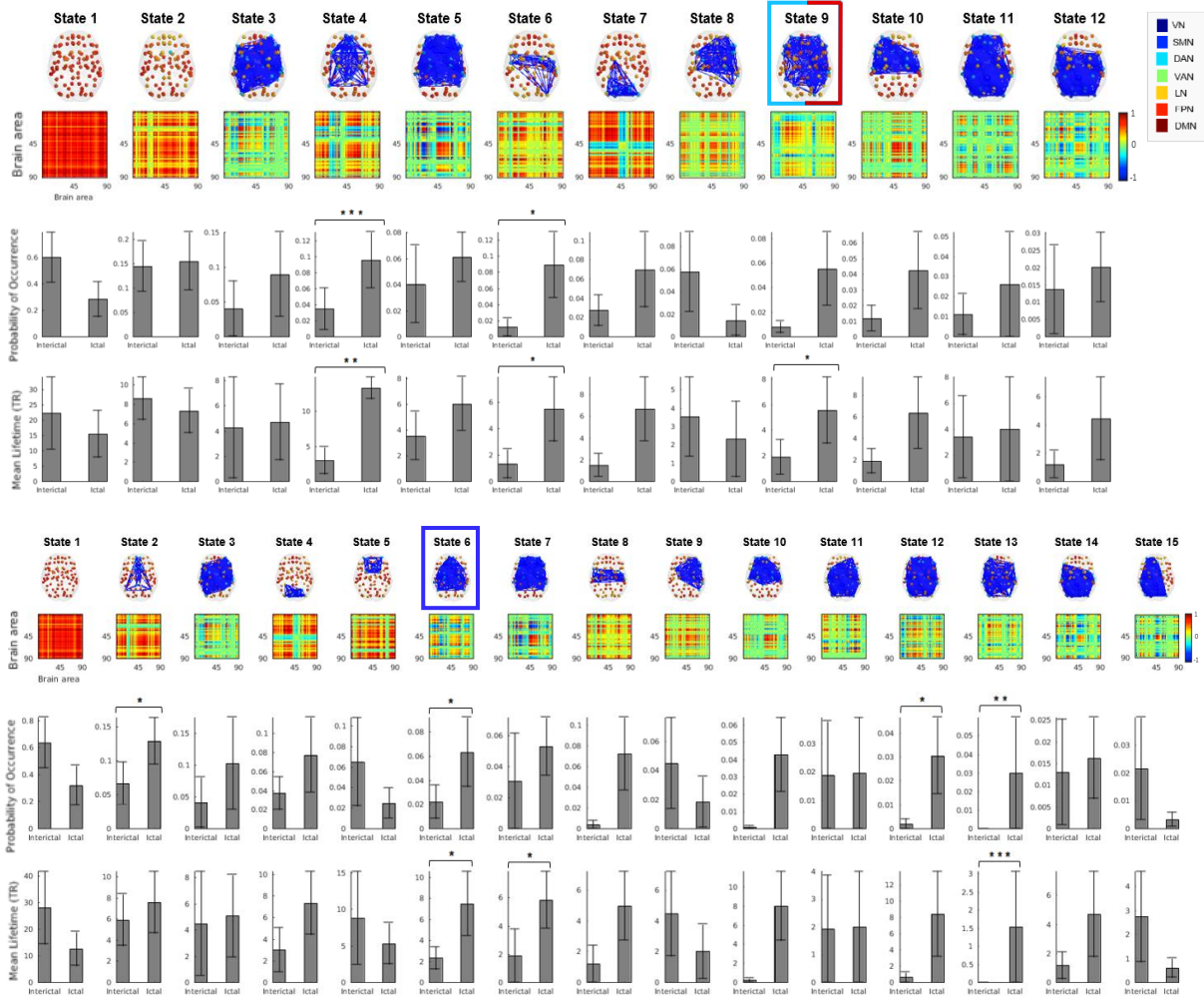


Figure D.2. *(Continued)*
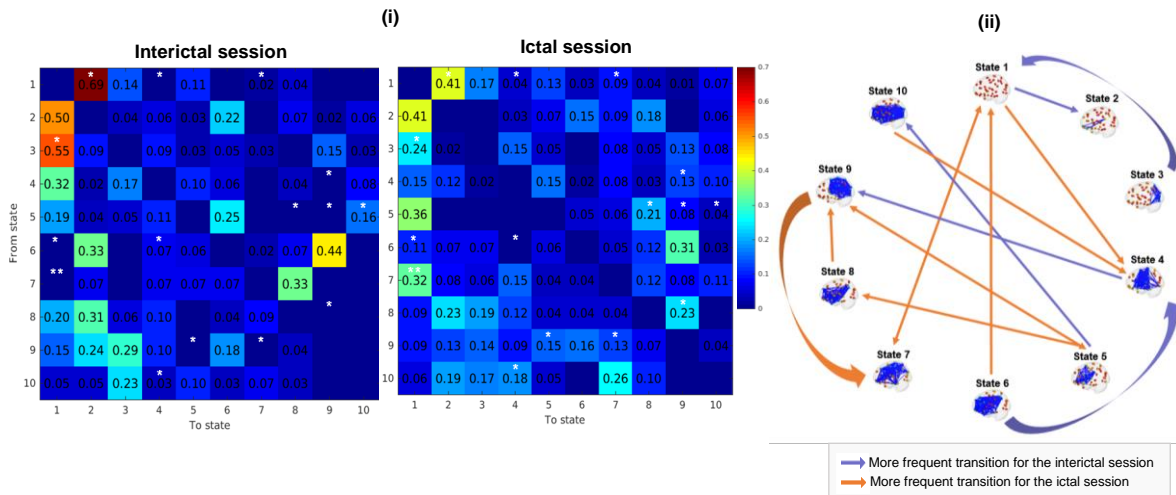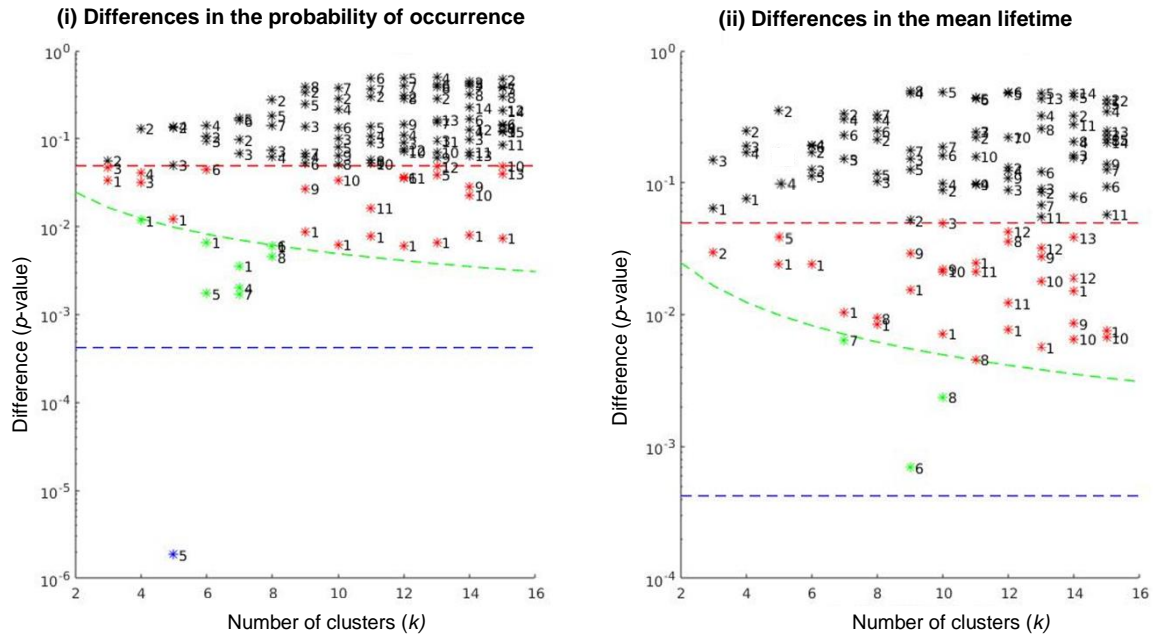
Figure D.2. *(Continued)*



Figure D.3. Switching profile between dFC states ($k$ = 10) obtained with the AAL90 atlas and PC method for the interictal and ictal sessions. **(i)** Transition matrices indicating the probability of, being in a given dFC state (rows), transitioning to another dFC state (columns). * Significant difference before correcting for multiple comparisons ($p$-value < 0.05). **(ii)** Plot exhibiting the significantly different transitions denoted with an asterisk in **(i)**. Purple arrows indicate the state-to-state transitions that occur with higher probability in the interictal session, and orange arrows represent those which are more prevalent in the ictal session.

## D.2. Migraineurs vs. Controls

**AAL116 atlas and PC**

**(i) Differences in the probability of occurrence**

**(ii) Differences in the mean lifetime**



**Desikan atlas and PC**

**(i) Differences in the probability of occurrence**

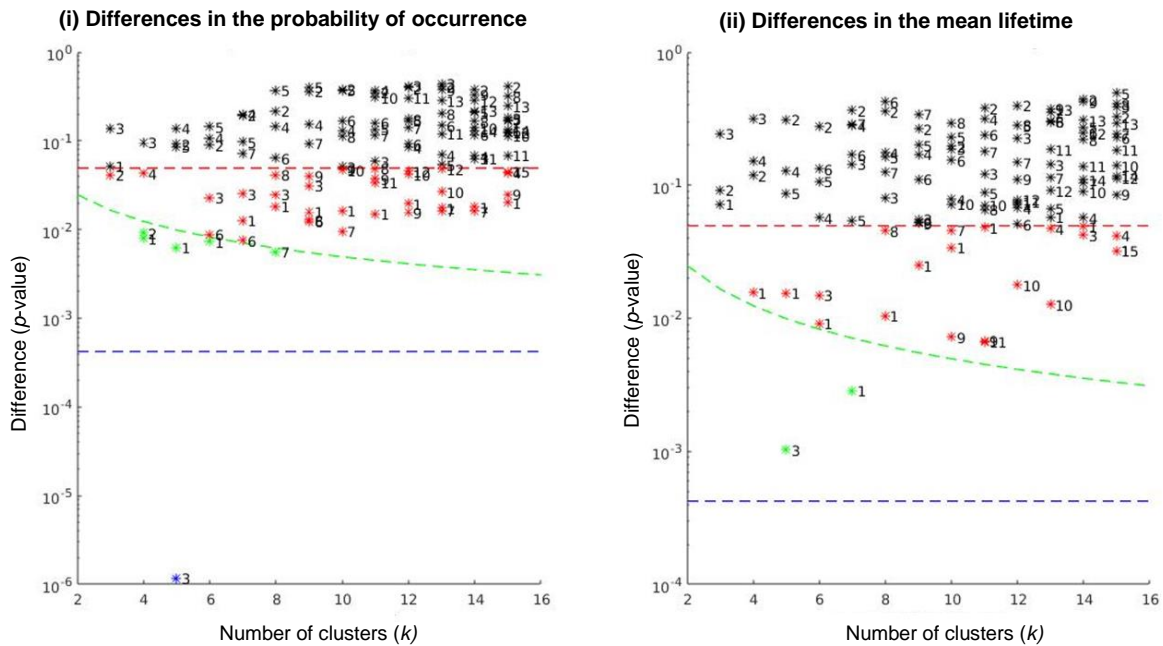**(ii) Differences in the mean lifetime**



Figure D.4. Significance of between-group differences in the **(i)** probabilities of occurrence and **(ii)** mean lifetimes of each dFC state, obtained with the AAL116, Desikan and Harvard-Oxford atlases and the PC method, between migraine patients scanned in the interictal phase and healthy controls, as a function of $k$. The red, green and blue dashed lines represent $p$-values equal to 0.05, 0.05/$k$ and 0.05/$\Sigma k$, respectively. Thus, all dFC states noted with a black asterisk (above the red line) passed the null hypothesis, i.e., present no significant difference between groups; the FC patterns marked with a red asterisk (above the green and below the red lines, $p$-value < 0.05, > 95 % of confidence) rejected the null hypothesis but did not pass the correction for multiple comparisons, being considered possible false positives; the states noted with a green asterisk (above the blue and below the green lines) rejected the null hypothesis with $p$-value < 0.05/$k$; and the states noted with a blue asterisk (below the blue line) rejected the null hypothesis with $p$-value < 0.05/$\Sigma k$.
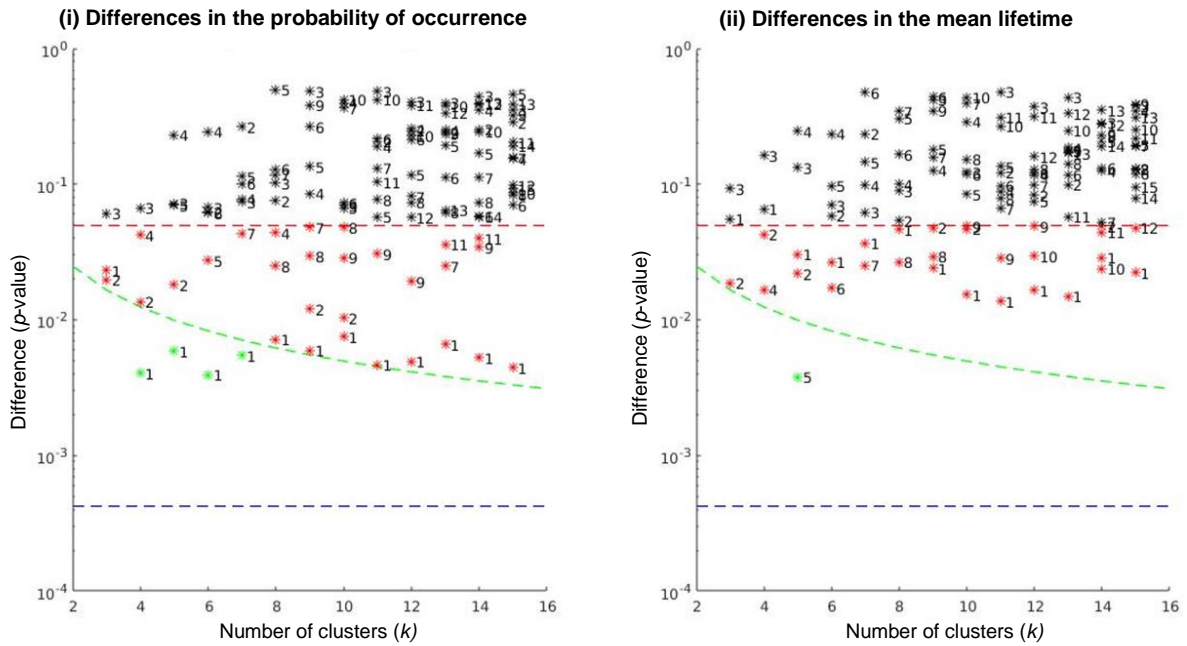
**Harvard-Oxford atlas and PC**

**(i) Differences in the probability of occurrence**



**(ii) Differences in the mean lifetime**



Figure D.4. *(Continued)*
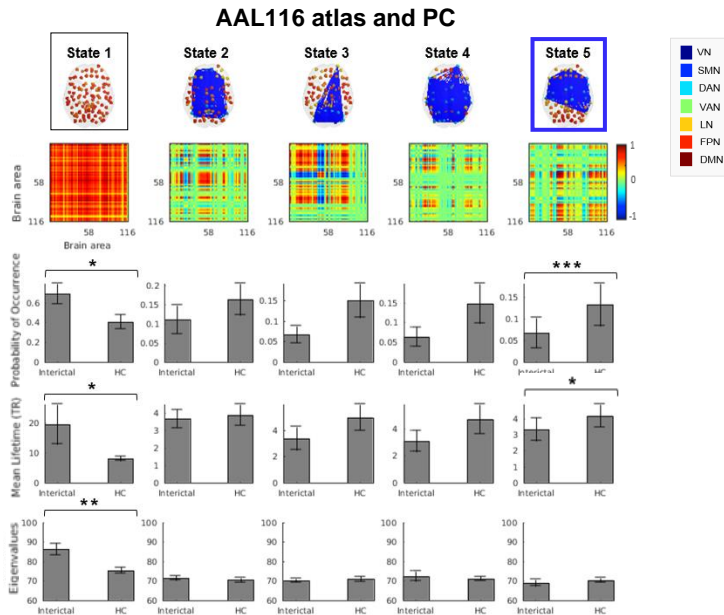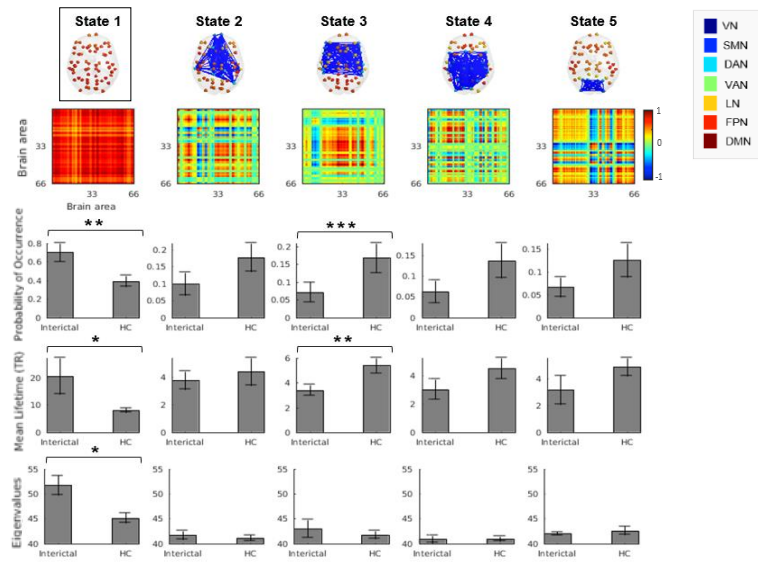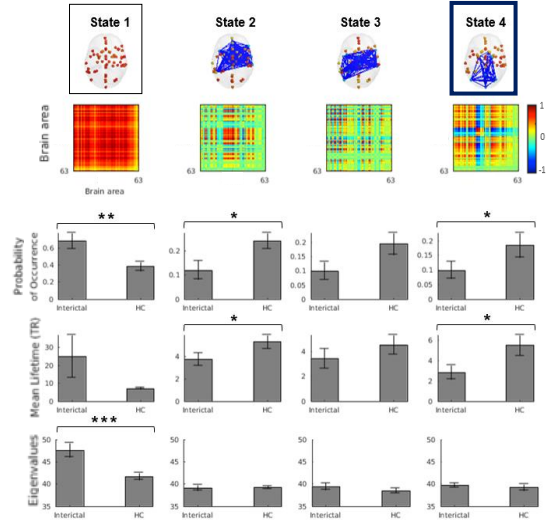
**AAL116 atlas and PC**



Figure D.5. dFC states obtained with the k-means clustering algorithm, displayed according to their decreasing probability of occurrence, for the AAL116 (k = 5), Desikan (k = 5), Harvard-Oxford (k = 4) and AAL90 (k = 14) atlases and PC method. Each dFC state is represented by its $V_c$ as: a network in the atlas cortical space (axial slice), in which the elements of $V_c$ are placed at the center of gravity of the respective brain region, shaped as spheres colored according to their sign (red to yellow spheres represent positive elements from 1 to 0, cyan to dark blue spheres represent negative elements from 0 to -1), and areas with $V_c \leq 0.1$ are linked with dark blue edges; and by the outer product $V_c V_c^T$. Below the representation of each state, the respective probabilities of occurrence, mean lifetimes and mean eigenvalues are displayed for the migraine patients in the interictal phase and healthy controls. The rectangle marks states with statistically significant between-group differences and correlation to any Yeo RSN, with the colors representing the RSN. The black rectangle marks the global mode. * Significant difference before correcting for multiple comparisons (*p*-value < 0.05); ** Significant diffence after correcting for multiple comparisons (*p*-value < 0.05/k); *** Significant difference after correcting for multiple comparisons (*p*-value < 0.05/Σk). HC = Healthy Controls.
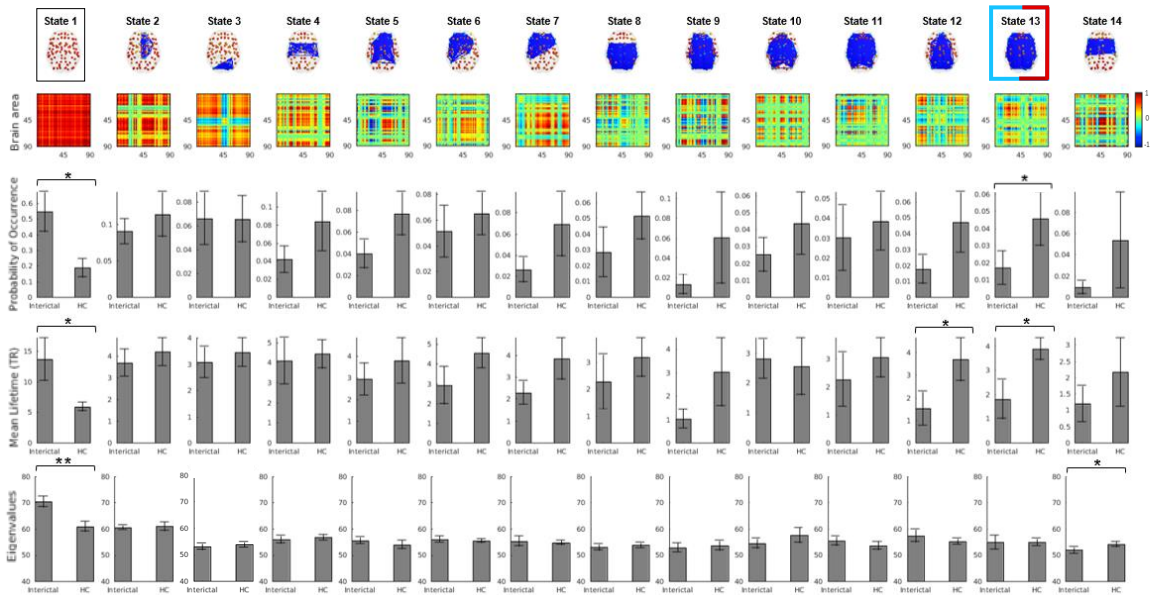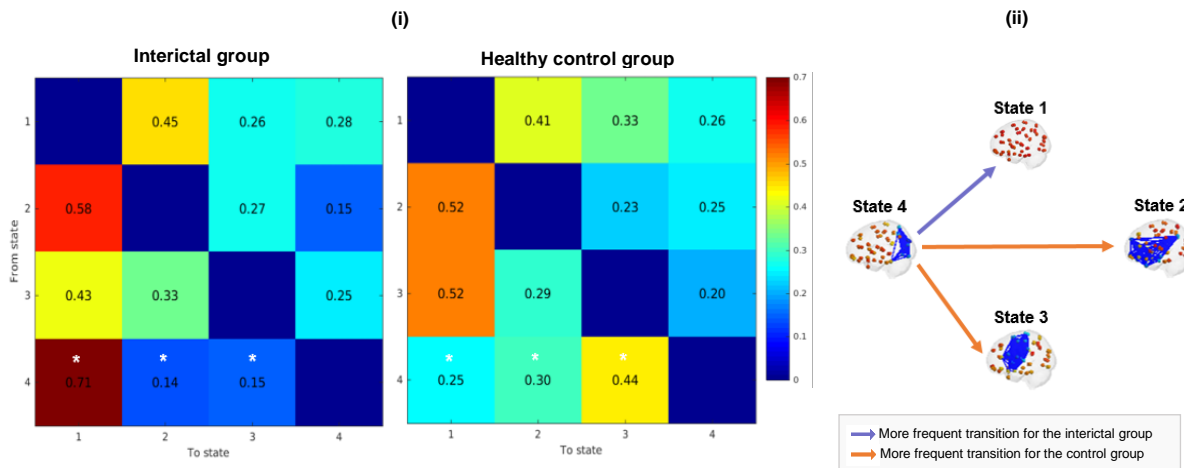
Figure D.5. *(Continued)*

Figure D.6. Switching profile between dFC states ($k = 4$) obtained with the AAL90 atlas and PC method for the interictal group and healthy control group. **(i)** Transition matrices indicating the probability of, being in a given dFC state (rows), transitioning to another dFC state (columns). * Significant difference before correcting for multiple comparisons (*p*-value < 0.05). **(ii)** Plot exhibiting the significantly different transitions denoted with an asterisk in **(i)**. Purple arrows indicate the state-to-state transitions that occur with higher probability in the interictal group, and orange arrows represent those which are more prevalent in the healthy controls group.